

**PREPARATION, CHARACTERIZATION OF
METAL OXIDE AND SILICON BASED
NANOSTRUCTURES FOR ENERGY
APPLICATIONS OF CATALYSIS,
SUPERCAPACITORS AND BATTERY**

Thesis

Submitted in partial fulfillment of the requirements for the degree of

DOCTOR OF PHILOSOPHY

by

MARTHA RAMESH



**DEPARTMENT OF PHYSICS
NATIONAL INSTITUTE OF TECHNOLOGY KARNATAKA,
SURATHKAL, MANGALORE -575025**

September, 2018

**PREPARATION, CHARACTERIZATION OF
METAL OXIDE AND SILICON BASED
NANOSTRUCTURES FOR ENERGY
APPLICATIONS OF CATALYSIS,
SUPERCAPACITORS AND BATTERY**

Thesis

Submitted in partial fulfillment of the requirements for the degree of

DOCTOR OF PHILOSOPHY

by

MARTHA RAMESH

Under the guidance of

Dr. NAGARAJA H. S.



**DEPARTMENT OF PHYSICS
NATIONAL INSTITUTE OF TECHNOLOGY KARNATAKA,
SURATHKAL, MANGALORE -575025**

September, 2018

DECLARATION

by the Ph.D. Research Scholar

I hereby *declare* that the Research Thesis entitled “Preparation, characterization of metal oxide and Silicon based nanostructures for energy applications of catalysis, supercapacitors and battery” which is being submitted to the National Institute of Technology Karnataka, Surathkal in partial fulfilment of the requirements for the award of the Degree of Doctor of Philosophy in Physics is a *bonafide report of the research work carried out by me*. The material contained in this Research Thesis has not been submitted to any University or Institution for the award of any degree.

Martha Ramesh

(Register Number: 112025PH11F07)

Department of Physics

Place: NITK-Surathkal

Date: 24-09-2018

CERTIFICATE

This is to certify that the Research Thesis entitled "Preparation, characterization of metal oxide and Silicon based nanostructures for energy applications of catalysis, supercapacitors and battery " submitted by Martha Ramesh (Register Number: 112025PH11F07) as the record of the research work carried out by him, is accepted as the Research Thesis submission in partial fulfilment of the requirements for the award of degree of Doctor of Philosophy.

DR.H.S.NAGARAJA

(Research Guide)

Chairman – DRPC

ACKNOWLEDGEMENTS

First and foremost, I wish to express my sincere appreciation and deepest gratitude to my supervisor, Dr. H.S. Nagaraja, for giving me the opportunity to extend my scientific skills during this Ph.D. work. I am grateful for pointing out an interesting research topic to me and spending time during fruitful discussions, while guiding me through this demanding period. I thank him for all advice and the possibility to work under his supervision, what allowed me to finalize this work.

I thank National Institute of Technology Karnataka for giving me the opportunity for doing research and Ministry of Human Resource Department (MHRD) Government of India for awarding research scholarship.

I thank the members of my Research Progress Assessment Committee (RPAC) Dr. Ajith (Department of Physics) and Dr. Ravishankar K.S.(Department of Metallurgical and Materials Engineering), for their suggestions during every stage of my dissertation work.

I wish to acknowledge help of Dr. S Anandhan and his student Martha Purna Chander Rao, Department of Chemistry, NIT-Tiruchirappalli for helping me in catalysis experiment.

I am grateful to all the faculty members, present and former HODs of Department of Physics, Dr. M.N. Satyanarayana, Prof. H.D. Shashikala, Prof. N.K. Udayashankar, Prof. G.K. Shivakumar, Prof. G. Umesh, Prof. Kasturi V Bangera, for their cooperation and support.

I express my sincere thanks to Dr. K Narayan Prabhu, Dr. Anandhan Srinivasan and Dr. Udaya Bhat K, Department of Metallurgical and Materials Engineering, NITK for providing contact angle measurement, FTIR, SEM, EDS, TEM analysis, and also Prof. A. C. Hegde, Department of chemistry, NITK for allowing me to carry out DC power analyzer for my samples and his student Liju Elias for helping in this regard.

I am indebted to Dr. Girish Kunte, IISc-Bangalore and Director, STIC-CUSAT, Cochin for providing Raman, HRTEM and SEAD analysis to my samples.

I would like to acknowledge the help and cooperation of the Physics staff including Mr. Dhanraj, Ashalatha Y, Mrs. Saritha, Miss. Usha, Mr. S. Nayak and Mr. Chandranna in carrying out my research and daily activities in the department.

I want to express my eternal thankfulness to my wife Marta Ramadevi for being at my side all the time. She is the source of my power and happiness. I could not do anything without her devotion, encouragement and unbreakable love. I am grateful to my parents Sathaiah and Sabitha for support and unremitting faith in me and love. I thank my sister Geetha and her spouse for being close to me when I needed it. I strongly believed that all my efforts, work, and success would not have been possible without their involvement in my life.

Finally, I would like to express my gratitude to my friends Ramana, Fernandes, P. Kiran, M. Kiran, Naveen, Venkatesh, Jean, Hidayat, Sadanand, Raghavendra, Bharath, Siby, Nagaraja, Santhosh, Kartic, Amuda, Breejesh, Bindu, Sreejesh and others at NITK for their encouragements, the motivation and direct or indirect help they gave me to finish this work.

Martha Ramesh

Abstract

The metal oxides/composite nanostructures (MnO_2 , rGO/MnO_2 , NiO , and CuO) have been synthesized via hydrothermally and chemical precipitation process. The prepared metal oxides/composites were characterized by XRD, FTIR, Raman spectroscopy, SEM, EDS, TEM, BET and DRS. The Adsorption and catalytic properties of the catalyst were tested on aqueous solutions containing mono- and multiple dyes, and the optimized process conditions were also established. The results indicate that dye RB-5 exhibits superior removal/degradation percentage using the process of adsorption and Fenton, as compared to the photo catalysis. The removal rates of RB-5 from wastewater treated using MnO_2 , rGO/MnO_2 , US/rGO/MnO_2 , catalyst were 63%, 84%, and 95% respectively, using Fenton/sono-Fenton method. NiO NPs found to be efficient adsorbent for RB5 dye molecules at higher annealing temperature. It is correlated to the band gap and surface area. Also, RB5 adsorption on NiO NPs follows second-order kinetics. CuO NPs were used as a photo catalyst to degrade various dyes, such as methylene blue (MB), acid yellow 23 (AY-23) and reactive black 5 (RB-5), with a low concentration in the presence of visible light. The results show that the highest degradation achieved was 67.8% and 66.3% for RB-5 dye and AY-23 dye, while 43.5% for MB dye from aqueous solution at 5h illumination. The enhanced catalytic performance of metal oxides/composites towards dye removal/degradation is found to be related to its structural and chemical properties. The decomposition products of RB-5 identified using GC-MS technique revealed a higher production rate of fragments in the sono-Fenton process. The kinetics of the reactions were investigated using batch assays. The supercapacitor electrodes fabricated using NWs of MnO_2 , rGO-MnO_2 , and Sn@rGO-MnO_2 reveal the specific capacitance of 139.05, 309.7 and 460.9 F/g respectively at a scan rate of 20mV/s, in an aqueous electrolyte Na_2SO_4 (1 M). The electrochemically prepared silicon nanowires were tested as an anode in Li-ion battery. The charge capacity of the anode is $\sim 3452.47 \text{ mAhg}^{-1}$ at the first cycle with the coulombic efficiency of 85.8 %, and faded to $1134.34 \text{ mAhg}^{-1}$ with coulombic efficiency of 81.6 % after the 12th cycle at a current rate of 1C.

keywords: *MnO₂nanowires, NiO, CuO, rGO, Si nanocrystals, catalysis, dye degradation, electrode materials, supercapacitor, Li ionbattery.*

Contents

Chapter	Titles	Page numbers
1	Introduction	1
1.1	Overview of catalysis	1
1.2	Metal Oxides as Catalysts	2
1.3	Doped Metal Oxide as Catalysts	5
1.4	Overview of dyes	6
1.5	Catalysis methods	9
1.6	Over view of charge storage devices	12
1.6.1	Lithium ion battery	12
1.6.2	Battery working principle	13
1.6.3	Silicon nanostructures	14
1.6.4	Super capacitors	14
1.7	Preparation methods	15
1.8	Characterizations	20
1.9	Scope and Objectives of the Thesis	28
1.10	Organization of the Thesis	29
2	Growth, characterization of undoped and Tin (Sn) &/or rGO doped MnO ₂ NWs and their applications in catalysis and super capacitor electrode	32
2.1	Introduction	32
2.2	Experimental Procedure	33
2.2.1	Synthesis of rGO nanosheets	33
2.2.2	Synthesis of MnO ₂ NWs	34
2.2.3	Synthesis of rGO-MnO ₂ and Sn@rGO-MnO ₂	34
2.3	Results and Discussions	34
2.3.1	Structural and optical properties of prestine α -MnO ₂ NWs	34

2.3.2	Structural and optical properties MnO ₂ nanocomposites	40
2.4	Applications	45
2.4.1	Catalysis	45
2.4.1.1	Catalytic Properties of pure MnO ₂ NWs	45
2.4.1.2	Catalytic Properties of rGO/MnO ₂ NWs using Fenton and sono-Fenton process	49
2.4.1.3	Influence of functional parameters	53
2.4.2	Super capacitors	59
2.4.2.1	Electrode fabrication	59
2.4.2.2	Electrochemical characterization	59
2.5	Conclusions	64
3	Growth, characterization and catalytic activity of NiO and CuO nanoparticles	66
3.1	Introduction	66
3.2	Experimental procedure	66
3.2.1	Preparation of NiO NPs	66
3.2.2	Synthesize of CuO NPs	67
3.3	Results and discussions	67
3.3.1	Structural and optical properties of NiO NPs	67
3.3.2	Structural and optical properties of CuO NPs	72
3.3.3	Adsorption and photocatalysis experiments	74
3.3.4	Reaction Kinetics	80
3.4	Conclusions	84
4	Preparation, characterization and electrochemical properties of Silicon nanostructures	85
4.1	Introduction	85
4.2	Preparation of Si NSs	86
4.3	Results and Discussion	86
4.3.1	Structural and optical properties of PS at the different etching time	86

4.3.2	Structural and optical properties of PS at the different current density	91
4.3.3	Structural, optical and electrochemical properties of Si NWs	97
4.4	Conclusions	107
5	Summary, Conclusion and Future directions	108
	References	114

Nomenclature

X	grain size (nm)
λ	wavelength
R_a	average roughness
h_{VPL}	PL peak position (eV)
E_g	band gap
α	absorption coefficient
R_{ku}	surface kurtosis
R_q	RMS roughness
A_0	initial absorbance
A_t	absorbance at the time of t
R_{sk}	surface skewness,
N	Avogadro's number
d	inter pore distance
D	Pore diameter
S	specific surface area
C	specific capacitance (F/g)
I	current (A)
v	scan rate (V/s)
V	potential
Δt	discharge time (s)
m	mass of the active material
P	porosity
γ_s	surface free energy
w	base width
R	regularity ratio
θ	contact angle

Chapter 1

INTRODUCTION

This chapter describes the general introduction of the thesis. The part of it includes an overview of catalysis with heterogeneous catalysts, such as various metal oxides and carbon related materials, along with preparation methods and characterization techniques. The remaining part of it is the overview of various industrial dyes along with various advanced oxidization methods. Brief discussion of experimental techniques used in the present work is also included.

1.1 Overview of catalysis

During the period of 19th century, the word catalysis remained greatly disputed till about 1900; Wilhelm Ostwald, presented convincing descriptions using kinetic concepts. In 1909, he received the Nobel Prize in chemistry for his contribution to catalysis and reaction kinetics (Gorin 1994). Nowadays, catalysis has a remarkable effect in our daily life and also industrial processes.

Catalysts are substrates that alter the rate of a chemical reaction without undergoing any change in it. In addition to the increase in the activity of the chemical species, catalyst offers a remarkable selectivity towards the certain desirable reaction reagents. Frequently, this higher selectivity is of more importance than increased reactivity, since a greatly selective route reduces the creation of waste intermediates (Moulijn et al. 1993).

Based on the phase of the reactant and the catalyst, they can be classified into two groups, namely - homogeneous and heterogeneous catalysis. In homogeneous catalysis, both reactant and the catalyst are at the same phase (eg, Ziegler Natta polymerization), but they are in different phases in the heterogeneous catalysis. Heterogeneous catalysis offers several advantages over the homogeneous catalysis

such as easy separation of products from the catalyst and more stable catalyst etc. Heterogeneous catalyst can either be semiconductor or metal or their oxides, which in turn may be amorphous or crystalline. Each kind has its own advantages and disadvantages based on their application. The efficiency of heterogeneous catalyst depends on its selectivity, activity, reproducibility, surface area and crystallinity (Choplin and Quignard 1998).

1.2 Metal Oxides as Catalysts

Transition metal oxides reveal one of the most significant and widely used categories of heterogeneous catalysts either as an active substrate or as support. The versatility of the use of oxide systems can be seen in many organic reactions like oxidation, hydrogenation, dehydrogenation, condensation, cracking, isomerisation and alkylation etc (Cavani and Trifiro 1999). Hence, oxide catalysts are important from the commercial point of view and have been used for manufacturing many valuable products.

Classifying metal oxide catalysts is tedious to a certain extent, since it involves a variety of crystal structures and compositions, along with wide range of physicochemical properties. Oxides have an ability to bring about electron- and proton- transfer and they can be used in both redox and acid base reactions. Some of the oxides have both acidic/basic properties; these are normally oxides of weakly electropositive metals like MnO_2 , NiO , CuO , etc. The other type of oxides, which are commonly used in oxidation reactions and photocatalysis, are semiconductor or conducting oxides, like reduced graphene oxide (El-Safty et al. 2008) (Cheng et al. 2009) (Sheikh et al. 2016).

(a) MnO_2

Manganese oxide is a most plentiful mineral in the earth's crust and consists spinel, layered, and tunnel forms. Among these, the tunnel types are constructed of several

(single, double, or triple) chains of $n \times m$ MnO_6 octahedrasuch as todorokite (3×3), romanechite (2×3), hollandite (2×2 , $\alpha\text{-MnO}_2$), ramsdellite (1×2 , $\gamma\text{-MnO}_2$) and pyrolusite (1×1 , $\beta\text{-MnO}_2$) (Kucza 2002). Fig. 1 depicts the structure of $\alpha\text{-MnO}_2$, where red balls are O_2 and purple Mn can be assembled by sharing edges and/or corners into octahedra and then createa densely packed wall to the a 2×2 tunnel along the c-axis (Tompsett and Islam 2013). It consists the tetragonal space group I4/m.

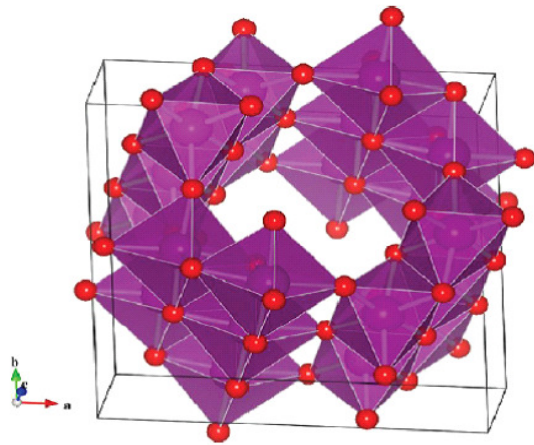


Fig. 1.1 A unit cell representation of manganese oxide.

(b) NiO

NiO is available as mineral, bunsenite in nature. NiO crystallizes in "NaCl" structure with a lattice constant of $a_0 = 4.17 \text{ \AA}$ (Sato et al. 1993). As illustrated in Fig. of 1.2, it is a simple cubic with octahedral Ni (II) and O^{2-} sites, wherein an anion at the corner of the cube and the cation in the middle of the cube (and vice versa). The NiO structure can be regarded as two interpenetrating FCC lattices. Each lattice point has 6 nearest neighbours of opposite charges, the so called rock salt structure and inter atomic distance is $\sim 1.94 \pm 0.05 \text{ \AA}$ in the p (2×2) phase (Saleh 2013). El-Kemary et al. (2013) reported that NiO NPs are much more effective catalyst or adsorbent due to its excellent durability, high photosensitivity, and high adsorptive affinity.

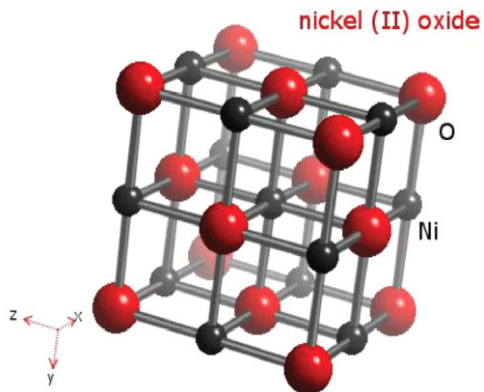


Fig. 1.2 A unit cell representation of nickel oxide.

(c) CuO

Copper (II) oxide is known as tenorite. It is a monoclinic unit cell (space group C_{2h}^6-C2/c) with the unit cell vectors of $c = 5.1288 \text{ \AA}$, $b = 3.4226 \text{ \AA}$, $a = 4.6837 \text{ \AA}$ and crystallographic angles of $\gamma = 90^\circ$, $\beta = 99.54^\circ$ and $\alpha = 90^\circ$. The atoms coordination is that each atom has four nearest neighbours of the other kind. For example, in the (110) plan (as depicted in figure I.3), where sky blue are Cu atom and red oxygen atoms with 1:4 ratio can be assembled into tetrahedron configuration (Asbrink and Norrby 1970).

CuO has attracted extensive attention as visible photo catalyst due to its low band gap. Evidently, recent work is reported by Rao et al. 2017 predicted that preparation of CuO nanostructures via chemical precipitation route, found to have efficient photocatalytic activity towards dye (tartrazine) degradation under visible light irradiation.

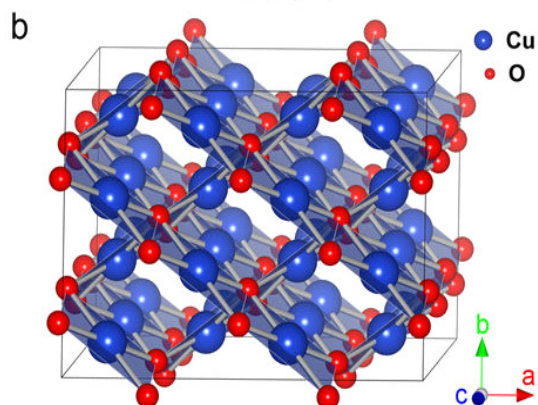


Fig. 1.3 A unit cell representation of copper oxide.

Table 1.1 Basic physical properties of metal oxides

Properties	MnO ₂	NiO	CuO
Appearance	Brown-black solid	green crystalline solid	black to brown powder
Molar mass	86.9368 g/mol	74.6928 g/mol	79.545 g/mol
Density	5.026 g/cm ³	6.67 g/cm ³	6.315 g/cm ³
Melting point	535 °C	1,955 °C	1,326 °C
Solubility in water	insoluble	negligible	insoluble

1.3 Doped Metal Oxide as Catalysts

Sometimes metal oxides are not active enough to achieve the highest catalytic performance. To overcome the above limitation, doping with suitable heteroatom is required, as metal-support interaction helps to change the electronic and chemical properties, thus helps to accomplish the desired performance. For instance, carbon

materials, like graphene oxide, can be chosen for doping the metal oxide. The presence of carbon ions in the metal oxide, strongly influences physical properties by tuning the synergy between the metal and oxide ions (Chen et al. 2010). The physical properties like dislocation density, surface area, and agglomeration might play a crucial role in the efficiency of degradation of organic pollutants or water splitting reactions.

(a) Reduced Graphene oxide

Reduced graphene oxide (rGO) is a non-stoichiometric, with less oxygen content and can be obtained from graphite, a low-cost starting material, that is found as flakes or a powder with diverse particle sizes. It is also highly transparent (97.3%) and extremely lightweight (Dresselhaus and Araujo 2010). As shown in Fig.1.4, rGO contains of a single atomic layer of sp^2 -two dimensional hybridized carbon molecules connected in a honeycomb crystal lattice and every carbon atom in graphene oxide is covalently bonded to three adjacent carbon atoms. The layers are distorted and the space between the two successive layers in rGO is larger (~0.7 nm) than the interlayer spacing in graphite (0.355 nm). Graphene oxide is a building block for other carbon/metal-based materials due to the large π network across the molecular structure. Hence, it can be wrapped up on the 1D metal oxide nano structures (Novoselov et al. 2005).

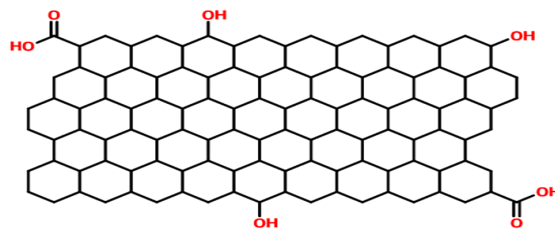


Fig. 1.4 Image of reduced graphene oxide

1.4 Overview of dyes

Dyes are known as substrates that provide color and will not fade their color affinity when exposed to water, light and any chemical substances (Rai et al. 2005). Azo dyes are the most important class of dyes and characterized by the existence of two nitrogen atoms ($-N=N-$). The 'azo' dyes have wide variety, namely basic, acidic,

reactive, mordant, direct, disperse, solvents or food dyes. Azo colorants offer high-intensity colors (Shaul et al. 1991). Among them, reactive black 5, methylene blue, acid yellow 23 are much familiar due to their special features, such as solubility, good fastness and easy attachment to the matrix (Garg et al. 2016)(Sahoo et al. 2012)(Merlain et al. 2016).

(a) Reactive black 5 (RB-5)

RB-5 is a anionic dye with the chemical formula of $\text{Na}_4\text{O}_{19}\text{S}_6\text{C}_{26}\text{H}_{21}\text{N}_5$ and molar mass 991.83 g/mol. It can be detected with an absorption peak at a wavelength of 596 nm in the electromagnetic spectrum. It is a odourless, black powder at ambient conditions. Reactive colorants contain a low utilization degree compared to other types of colorants because their chemical groups react with water and causing hydrolysis.

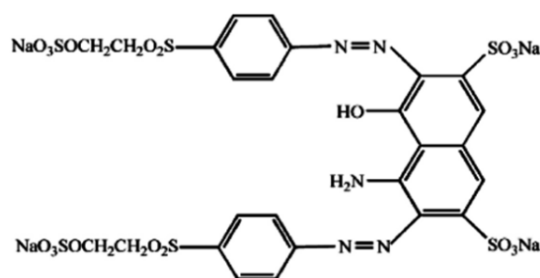


Fig. 1.5 Image of RB-5

(b) Methylene Blue (MB)

MB is a cationic type dye with a chemical formula: $\text{C}_{16}\text{H}_{18}\text{ClN}_3\text{S}$ and a molar mass of 319.85 g/mol. It can be detected at a absorption wavelength of 664 nm in the electromagnetic spectrum. MB is a solid, odorless, and dark green in complexion at ambient conditions and changes its complexion to blue when dissolved in water. MB

contains 3 molecules of water per one unit in its hydrated form with pH = 3 in water (10g/L) at 25 °C (77 °F).



Fig. 1.6 Image of MB

(c) Acid Yellow 23 (AY-23)

AY-23 is an anionic dye type with the chemical formula C₁₆H₉N₄Na₃O₉S₂ and a molar mass 534.37 g/mol. It is measurable at an absorption wavelength of 432 nm in the electromagnetic spectra. AY-23 is apparent as solid, odorless, orange-yellow in complexion and changes its complexion to light yellow, when dissolved in water. It is an azo dye with two sulfonate groups and one carboxylate group.

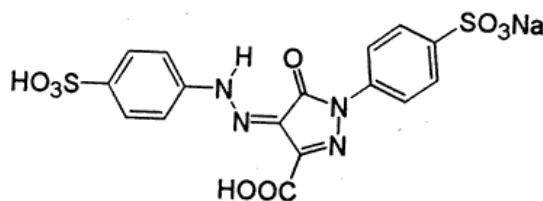


Fig. 1.7 Image of AY-23

These colorants are extensively used in the various industries because of their excellent bath stability, high degree of exhaustion and very high wash fastness properties. Their chemical species are capable of forming covalent bonds with nucleophilic or hydroxyl groups of the matrix during dyeing/coating process. In that regard, the dye-matter reaction varies from 90 to 50 %, and the remaining unfixed dye material is washed off. Therefore, a considerable quantity of these colorants can be directly released into wastewater. These colorants are toxic and problematic to aquatic and human life.

In order to decolorize the wastewater, different route, such as chemical, electrochemical, biological and physical methods have been invented. Among these, advanced oxidation process (AOP) have a significant attention, due to its special features like efficiency, environmental-friendly, and cost-effectiveness for treating dye-contaminated wastewater.

1.5 Catalysis methods

(a) Adsorption

It is a surface process of collecting chemical species at the surface of the solid phase, which arises due to the existence of residual or unbalanced forces at the surface of liquid/solid. These forces have a tendency to interact with the chemical species and deposits on the solid surface. This process takes place via two components, such as adsorbate and adsorbent. Adsorbent is the solid on the surface of which adsorption occurs. Adsorbate is the solute which is being retained on the surface of adsorbent (McKay 1995).

(b) Fenton process

The Fenton process has been discovered by chemist, Fenton in 1894; however, the attention in this procedure is renewed due to its capability to degrade toxic pollutants such as organic pollutants and their derivatives (FentonH 1894). It is an ionization of metal or metal oxides, when they interact with oxidant, like hydrogen peroxide in an aqueous solution. This is one of the easy techniques for decolorizing wastewater, without longer duration and expensive chemicals. Additionally, disposal water treated with Fenton process is not problematic as Mn, rGO and their composites are a plentiful and not toxic elements, while H_2O_2 is environmentally safe and easy to handle (Saputra et al. 2013).

It possesses three processes such as adsorption, oxidation, and desorption. Initially, hydrogen peroxide molecules adsorb on the catalyst and disintegrate into free

primitive species. The generated free radicals have the high oxidative capability to break the adsorbed effluents. Likewise, more effluent molecules could transfer from the suspension to the catalyst and later be mineralised to smaller components. The obtained small components from the aqueous solution would leave the catalyst surface by desorption, which results in recovery of catalyst (Haber and Weiss 1934).

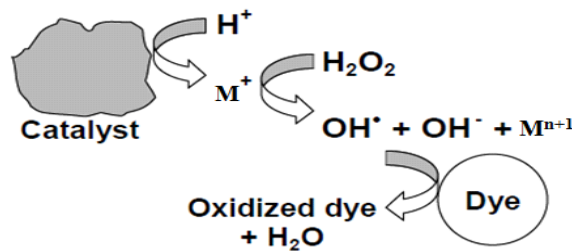


Fig. 1.8 Image of Fenton process

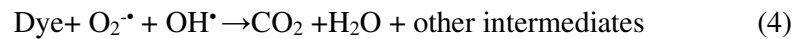
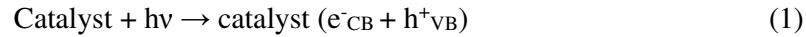
(c) Sonolysis

Sonolysis facilitates to understand the effect of ultrasound in the aqueous solution. When sound waves propagate via a solution, at higher frequencies with a wavelength larger than the bond length of the water molecule, massive energy begins to build-up inside the cavitation bubble, inducing localized high temperatures and pressures. The thermal dissociation of water molecules in the solution leads to creation of primary and secondary radicals. The resultant radicals can be mixed with bulk liquid, where they can intimate and promote hydroxylation reaction leading to decomposition of colorants (Jensen 1996).

(d) Photo catalysis

This process also activates catalysts, when its band gap is less than the absorbed photon energy. It generates the opposite charge carriers in the catalyst such as electron (e^-) and hole (h^+). The negatively charged electrons in conduction band are good reductants, whereas positive charged holes in valence band are good oxidants (Eq. 1). Thereafter electrons react with atmospheric oxygen to produce superoxide anion

radical (Eq. 2), meanwhile holes react with water molecules to produce the hydroxyl radicals (Eq. 3). These radicals are mainly responsible for the attacking of dye molecules, which adsorbed or close to the catalyst surface (Eq. 4).



Thereafter, they can be involved in the redox reactions with water and oxygen molecules. The resulting radicals are extremely reactive to oxidize colorants into the minor products (Maruska and Ghosh 1978).

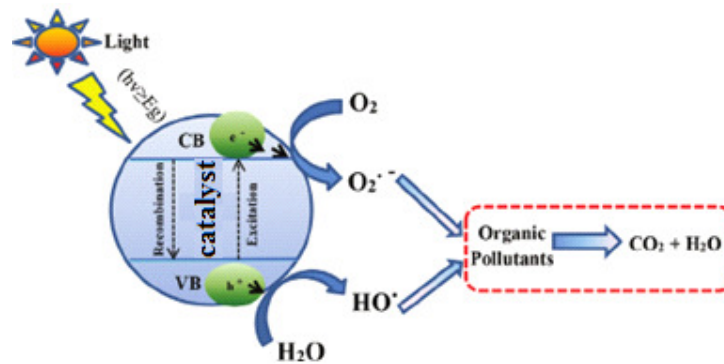


Fig. 1.9 Image of photocatalysis

In photocatalysis, the efficiency of the catalyst could be predicted through a number of reactions occurring per photon absorbed on it. It depends on the rate of migration, the density of energy levels in the catalyst and charge generation rate. The charge generation rate is decided by the irradiation conditions such as photon energies, flux and related to properties such as surface area, optical band gap, and crystallite size. The fate of charge carriers determine the reactions that occur both within the particle and on its surface (Rajeshwar 1995).

1.6 Over view of charge storage devices

1.6.1 Lithium ion Battery

Batteries are charge storage devices that can interchange energy between chemical and electrical forms via redox reactions. At the end of 18th century, Italian physicist, Alessandro Volta discovered battery for the first time. Thereafter a different series of battery devices have been invented (Song et al. 1999). Lithium (Li) is well known material in battery devices, because of its special features such as highest operation potential, high specific capacity, and light weight. Upon constant charge transfer, dendrites were created on Li, hence, hence Li is not broadly employed as electrode. This led to the innovation of Li battery using carbonaceous material, in which Li ions could be intercalated/deintercalated through electrochemical reactions (Zhang 2011).

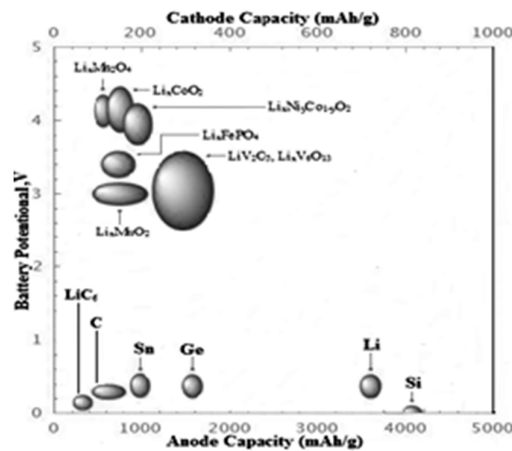


Fig. 1. 10 Comparison of battery technologies including gravimetric energy densities and volumetric energy densities.

Among all conventional batteries such as nickel metal hydride, nickel acid, nickel oxide hydroxide nickel cadmium, and other popular rechargeable batteries, LiBs batteries are regarded as most familiar because of their high operating voltage, light in weight, high energy density and electrochemical stability (Etacheri et al. 2011). Generally, carbon and polymers are utilized as an anode material in Li-ion Batteries (Wu et al. 2011, Meyer 1998) but they poses a limitation leading to further improvement in the specific capacity. Si has been chosen as alternative, owing to its

highest theoretical capacity ($\sim 4200 \text{ mAh}\cdot\text{g}^{-1}$). During last decade, a large amount of research has been done on the bulk Si but rather limited work on the preparation of Silicon nanostructures with proper alignment and their integration into higher performance of LIBs (Su et al. 2014a).

1.6.2 Battery working principle

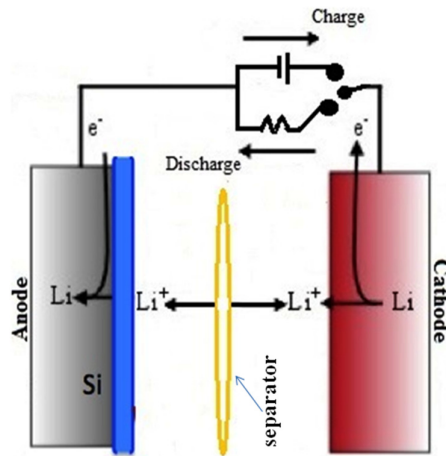


Fig. 1.11 The lithiation and delithiation process in Silicon Anode of Lithium ion battery. Each Silicon atom can hold 4.4 lithium ions when it is fully charged.

When the two electrodes, anode and cathode are immersed in the electrolyte, one of them will liberate electrons and the other will gain electrons. The gain or lose of electrons depends upon the electron affinity of the electrode. The electrode with high electron affinity will liberate electrons to the positive ions or electrode with low electron affinity gain the electrons from the negative ions of the electrolyte solution. In most practical battery devices, a separator is also inserted between two electrodes to prevent them from physically touching each other since they are usually in very close physical proximity. During charging, the Li ions move from cathode to the anode through the reduction, this process is called lithiation. Hence the electrical energy is converted into chemical energy. On the other hand, when the battery is discharged, Li ions travel from anode to the cathode through oxidation, this process is

called delithiation. During the discharge, the chemical energy is converted in to the electrical energy.

1.6.3 Silicon nanostructures

The first work on silicon nanostructures (nanopores or nanowires) was reported by Wagner and Ooherty (1968). They managed to grow silicon nanostructures using the Vapour Liquid Solid (VLS) mechanism using gold as the catalyst. Generally Si nanostructures are either 'grown' or etched. Growth can be initiated using a nucleation center (for example a catalyst) and a precursor material. Etching refers to a process, where material is removed locally to create nanowires and nanopores. Si nanowires are studied widely for their potential applications in battery. Nevertheless, there have been a few discussions on the physical properties of the Si NWs.

1.6.4 Super capacitors

Super capacitors are of considerable interest because they deliver more power than batteries and store more energy than common capacitors. A characteristic schematic of the supercapacitor is depicted in Fig.1.12. Like capacitors, super capacitors are built-up from two highly porous electrodes, which are separated by a dielectric membrane. When the external potential is applied between the electrodes, opposite charge careers gather on their surfaces. Meanwhile, electrolyte ions travel into the pores of the electrodes. It leads a double layer at each electrode. Pseudo capacitance can be developed, when adsorbed ions out of the electrolyte penetrate the double-layer. The performance of super capacitors depend on the electrolyte, distance between electrodes, surface area and structure of electrodes (An et al. 2001).

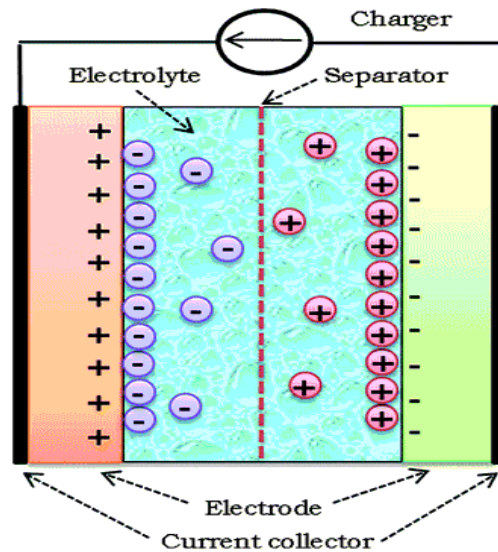


Fig. 1.12 Image of a super capacitor.

1. 7 Preparation methods

Metal oxides, mentioned above, have been synthesized using different methods such as hydrothermal, chemical precipitation and Modified Hummer’s method, because they are a low–temperature process giving better microstructural control of metallic particles, superior homogeneity, and purity, uniform particle distribution, high yield and specific surface area, and is most importantly cost effective.

(a) Hydrothermal process

It was introduced firstly, by a British geologist, Roderick Murchison in about 1840, to reveal the role of water at prominent pressure and temperature in the earth’s crust leading to the creation of different minerals and rocks. Afterwards, the hydrothermal process was employed to grow the single crystals (Prakasam et al. 2015). Typically, the growth of crystals is carried out hydrothermally in a steel pressure vessel, in which a variety of nanostructures can be produced. A temperature gradient is developed along the opposite ends of the steel vessel. Initially, nutrient solute which is soluble at the hotter end, deposits on a seed crystal at the cooler end, growing the

desired crystal. In this present work, the aqueous reaction mixture was taken in an autoclave (Hydrothermal Autoclave, Tech Lab Instruments Co., Kottur, Chennai) heated to temperature of 130-200 °C at high vapor pressures (0.3 – 4 Mpa) with a volume of 100 mL for 12 h in air.

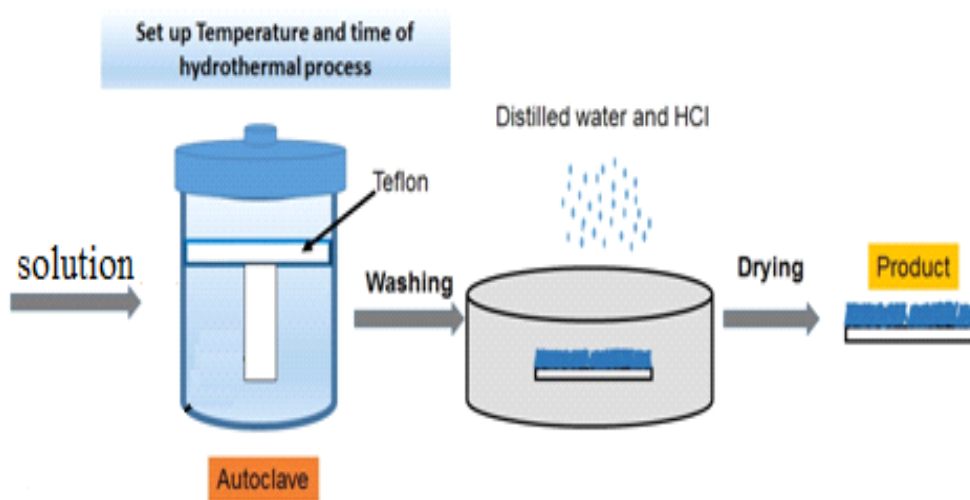


Fig. 1.13 Image of hydrothermal method



Fig. 1.14 Experimental set-up for the hydrothermal process

(b) Chemical precipitation

It is a process in which, solid products are away from a reaction mixture, either by converting the products into an unsolvable form or by varying the concentration of the solvent to weaken the solubility of the reagent in it. It contains several parts: rapid mix, sedimentation, and filtration. Rapid mix combines the coagulants with the inflow water, the sedimentation process functions to lower the turbidity through settling and resultant metal contaminants are separated by filtering in the form of metal hydroxides or metal carbonates. Here, solubility is a factor that determines the removal performance of target contaminants in the water, that varies as complex conditions, such as temperature and solution ionic strength (Reynolds 1933).

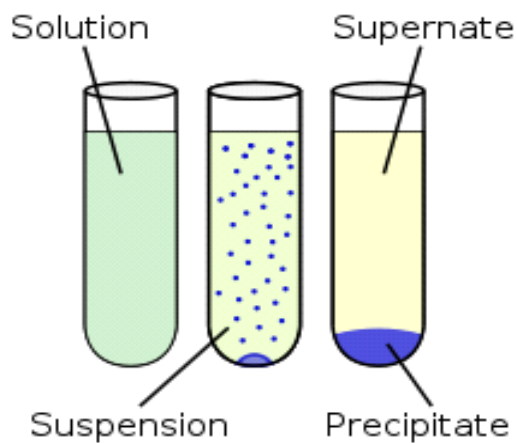


Fig. 1.15 Image of chemical precipitation process

(c) Thermal decomposition method

It is known as a thermolysis, in which solid products could be decomposed chemically through heat. During the thermal decomposition, there arise physical and chemical changes in materials due to the evolution of volatile matter. This method is most suitable to synthesize metal oxides, example NiO, and its composites because it provides better homogeneity, low processing temperature, controlled stoichiometry, control over the particle size of the crystallites, inexpensive, flexibility of creating dense nanoparticles or nanosheets (Galwey and Brown 1999).

(d) Hummer's method

Modified Hummers method is used to synthesize of graphite oxide (or graphene oxide). It involves an additional pre-oxidation step. Hummers method as a safer, faster and more efficient method for graphite oxide synthesis was first reported in 1958. After the discovery of graphene in 2004, people gradually noticed graphite oxide can be exfoliated into single-layered graphene oxide simply by ultrasonication in water as shown in Figure 6. Typically in Hummers method, natural graphite flakes (or powders) are oxidized into graphite oxide with conc. H_2SO_4 , NaNO_3 , and KMnO_4 at 35°C (Chen et al. 2013).

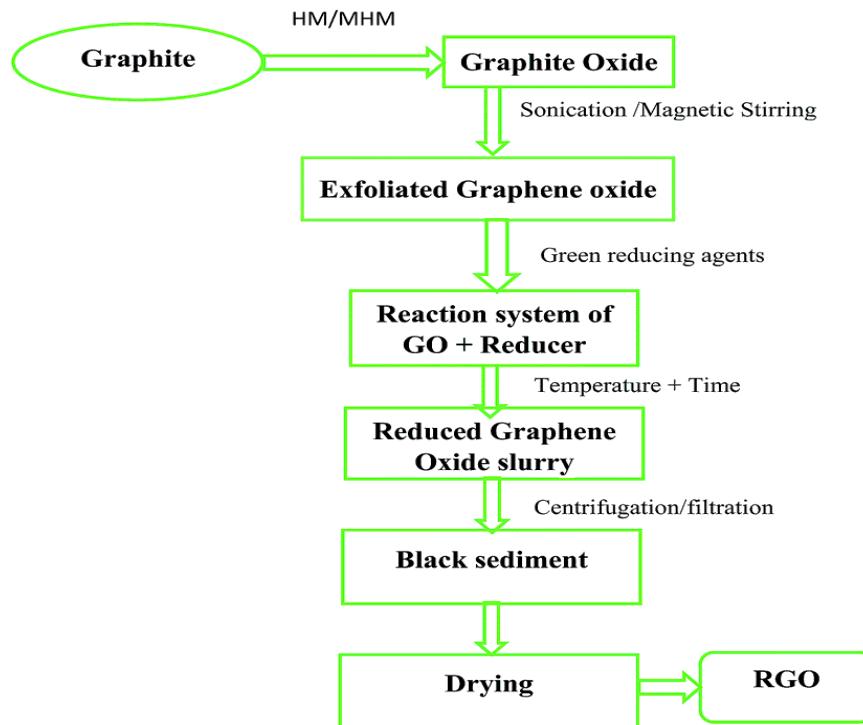


Fig. 1.16 A Schematic representation of green reduction of graphene oxide via modified Hummers method.



Fig. 1.17 Image of rGO solution prepared in the laboratory.

(e) Electrochemical etching

Electrochemical etching is considered a simple and versatile route to grow a variety of Si NSs from silicon wafer. The electrochemically etched Si NSs are featured with outstanding physical properties such as low level of defects, high surface-to-volume ratio and high crystalline quality. In addition, the produced Si NSs can be precisely controlled via various etching factors such as time, applied current density, illumination intensity, temperature and concentration of the electrolyte etc. Typically, among these parameters, the current density and etching time are critical parameters, which lead to precisely ordered arrays of NSs with uniform growth. Hence, the etching time and current density must be enlarged as macrostructure grow in order to get vertical and well-defined NSs from up to down. For these reasons, Electrochemical etching of silicon has become an alternative route to conventional etching methods.

1. 8 Characterizations

(a) X-ray Diffraction (XRD)

XRD analysis was carried out to investigate the crystallinity of the solid products. The crystalline phases of the products were identified using a Panalytical diffractometer (Rigaku miniflex 600, Japan, X-ray tube-Toshiba A-21, Panalytical PW22XX) connected with a copper anode ($K\alpha = 1.540598\text{\AA}$). The 2θ range of 10 to 80° with a step size of 0.02° was used. Then, the obtained data were evaluated using either International community for diffraction data (ICDD) or diffraction standard patterns in Joint Committee for Powder Diffraction Standard (JCPDS) files. At maximum diffraction peak, the average crystallite size and dislocation density in the prepared products are estimated using Debye-Scherrer (Holzwarth and Gibson 2011), and Smallman's and Williamson formula (Williamson and Smallman 1956) respectively.

$$D = K\lambda/\beta\cos\theta \quad (5)$$

$$\delta = n/D^2 \quad (6)$$

where D is the average crystallite size (nm), K is the shape factor which is identical to 0.9 , λ is the X-ray wavelength, 0.154 nm for $\text{Cu } K_\alpha$ radiation, β is the line width at half of the peak intensity (radians), θ is the angle of the peak (degrees), δ is the dislocation density, and “ n ” is unity.



Fig. 1.18 Image of the XRD equipment

(b) Scanning Electron Microscopy (SEM) and Transmission Electron Microscope (TEM)

SEM and TEM are used to study the surface morphology of nanomaterials such as silicon, graphene and metal oxides. SEM (JEOL JSM 6380LA, Japan) and TEM (JEOL JEM 2100) which operates at the energy range from 200 keV to 3 keV is used. Prior to observation, samples were coated with gold layer in nanosize using a JFC 1600 autofine coater (JEOL, Japan). TEM is more favoured than SEM because it provides details about defects in crystalline solid materials, phase impurities, extended magnification range and the particular plane of Miller indices.

(c) Energy Dispersive X-ray analysis (EDX)

EDAX, also known as EDS, is widely used to examine the atomic and weight percentage of the samples. EDS equipped with SEM gives the qualitative information, which means various intensity peaks associated with elements, in order to know the real composition of the sample and also to detect contamination in the sample composition. Furthermore, elemental mapping of a product and image analysis have been carried out.

(d) Fourier transform infrared spectroscopy (FTIR)

FTIR is a useful to detect the chemical bonds and molecular structures of samples. In the present study, FTIR analysis was performed on the various metal oxides such as MnO₂, rGO/MnO₂ and NiO using JASCO-4200 FTIR spectrometer to determine the relevant functional groups, which exist in the samples. FTIR absorbance/transmittance data was recorded over the range of 400 - 4000 cm⁻¹ with a resolution of 1cm⁻¹, using a Pike Technologies diamond crystal plate ATR in transmission mode. Prior to observation under FTIR, the products were mixed with dry KBr and grounded thoroughly to make a pellet. The pellets were placed into the sample holder for recording the IR spectra and referencing was done by recording a blank KBr pellet.

(e) Raman spectra

Raman spectra is used to observe the various frequency modes and crystalline parameters in the desired sample. In the present study, the Raman spectra were recorded on MnO₂ and rGO/MnO₂ NWs over the spectral range of 400 – 2000 cm⁻¹ using model LabRam HR800 (Horiba Jobin Yvon Inc. USA). Raman shift is determined from the following expression. Raman shifts are directly related to energy and are reported in wave numbers with units of inverse length (Bowley et al. 2012):

$$\Delta\omega = (\lambda^{-1} - \lambda_1^{-1}) \quad (7)$$

where $\Delta\omega$, λ_0 , and λ_1 are the Raman shift (cm⁻¹), excitation wavelength, and incident wavelength, respectively.

Model suggested by Ossadnik et al. (1999) uses the following Eq. (8) to calculate the size of the crystallites (d) in the nanomaterials.

$$\text{Raman Peak (cm}^{-1}\text{)} = 521.01[10d/(10d+0.337)] \quad (8)$$

(f) Photoluminescence

Photoluminescence is an important technique for measuring the crystallite size, crystalline quality and for quantification of the amount of disorder present in nanomaterials. The average crystallite size can be determined from the following Eq. (9) (Gonchar et al. 2016).

$$h\nu_{PL} = E_g + 3.73/d^{1.39} \quad (9)$$

Where d - grain size (nm), $h\nu_{PL}$ - PL peak position (eV) and E_g - band gap of the material

(g) UV-Visible spectroscopy

The technique is frequently used to detect the quantity of an absorbing species in a liquid using Beer-Lambert law (Said et al. 2014).

$$A = \log_{10} (I_0/I) = \epsilon cL \quad (10)$$

Where A , I_0 , I , L , c , and ϵ is the absorbance, incident light intensity, transmitted light intensity, path length, concentration, and molar absorptivity, respectively. From the absorption spectra, the optical band gap can be obtained using Tauc's relation.

$$\alpha h\nu = A (h\nu - E_g)^n \quad (11)$$

where, α is the absorption coefficient of the sample, n is the power factor of the transition mode, ν is the light frequency, A is a constant called the band tailing parameter and E_g is the energy of the optical band gap. The Tauc's plot of $(\alpha h\nu)^2$ vs $h\nu$ for direct band gap and $(\alpha h\nu)^{1/2}$ vs $h\nu$ for indirect band gap. And the choose straight line vertically downward to energy-axis that value is the optical band gap (Ebraheem and El-Saied 2013).

The decolorization percentage was calculated according to the following Eq. (12): where A_0 refers to the initial absorbance, and A_t is the absorbance at the time of t (Goharshadi et al. 2013).

$$\text{Decolorization (\%)} = ((A_0 - A_t)/A_0) \times 100 \quad (12)$$

(h) Brunauer-Emmet-Teller (BET)

The BET method is often used to determine the specific surface area of a material based on physical adsorption of gas molecules on a solid surface. The specific surface area of the prepared samples was estimated based on the nitrogen desorption-adsorption kinetic reaction, attained using a BELSORP mini II measurement (BEL Japan Co., Ltd). The BET curve is a straight line by plotting $\varphi = p/p_0$ against $1/\nu[(p_0/p)-1]$, where p is the equilibrium pressure, p_0 is the saturation pressure of adsorbates and monolayer adsorbed gas quantity ν . From BET plot, the value of the intercept I and the slope A of the line are used to determine the BET constant c and monolayer adsorbed gas quantity ν . The following relations can be used to find the specific surface area S_{BET} , as well as total surface area S_{total} of the material (Brunauer et al. 1938).

$$S_{total} = (\nu_m N_s)/V \quad (13)$$

$$S_{BET} = S_{total}/a \quad (14)$$

The specific BET surface area, average pore radius and specific pore volume can be related from the following relation (Samejima et al. 1977).

$$S_{\text{BET}} = 4/d \cdot V_g \times 10^8 \text{ [cm}^2\text{/g]} \quad (15)$$

where, v_m is the monolayer volume of the adsorbed gas, V is the molar volume of the adsorbed gas, N is Avogadro's number, a is the mass of the solid sample or adsorbent, s is the adsorption cross section, d is the average pore diameter and V_g is the specific pore volume ($\text{cm}^3\text{/g}$)

(i) Gas chromatography-mass spectrometry

Gas chromatography–mass spectrometry is an analytical method that merges the features of mass spectrometry and gas-chromatography to detect the various molecular products to provide elemental analysis within a test sample. The sample solution injected into the instrument enters a gas stream (nitrogen or helium) which transports the sample into a separation tube known as the "column". The function of the stationary phase in the column is to separate different components, causing each one to exit the column at a different time. As the chemicals exit the end of the column, they are ionized by the mass spectrometer and detected in terms of mass-to-charge ratio. In the present work, we used GCMS-QP 2010 Plus Shimadzu mass spectrometer to evaluate the catalysis by-products. HP-5 ms column consists the dimensions of 0.25 mm \times 30 m, 0.25 μm . The temperature was ramped as follows: 36 °C for 1 min, 5 °C min^{-1} up to 300 C and hold time is 10 min. The temperature of the transfer, inlet, and source and line was 280, 250 and 230 °C respectively. The analysis was done using splitless (0.7 min) injection.

(j) Cyclic voltammetry

Cyclic voltammetry (CV) is used to study a supercapacitor's charge-response with respect to variation in a potential, which gives a means of measure of capacitance. To carry out CV experiments, a series of varying potential at a steady sweep rate (dV/dt)

is applied and the response current is measured. The specific capacitances of the electrodes are determined from galvanic discharging and CV curves using the following expressions (Khomenko et al. 2005).

$$C = \frac{I \times \Delta t}{m \times \Delta V} \quad (16)$$

$$C = \frac{1}{mv\Delta V} \int I(V)dV \quad (17)$$

where, I is current (A), C is specific capacitance (F/g), v is the scan rate (V/s), ΔV is the potential window of discharge (V), I' is the constant discharge current density (mAcm^{-2}), Δt is discharge time (s), V is potential (V), and m (g) is the mass of the active material in the working electrode.

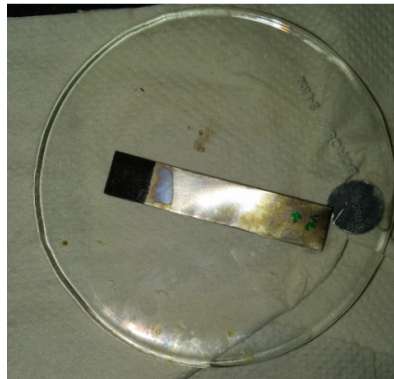


Fig. 1.19 Active material prepared as electrode to measure the super capacitive properties

(k) Glove box

It is a closed chamber that is intended to permit one to move the things within a very high purity inert atmosphere, such as nitrogen or argon. The glove box is especially used in order to protect Lithium (Li) from its chemical oxidation during fabrication of battery. In Li ion battery, Li is used as an electrode due to its high chemical reactivity. Li is 1A group element in the periodic table and very sensitive to water, oxygen and

nitrogen molecules. In water, Li slowly creates a liquid, LiOH. In addition to interact with O₂, Li also interacts with N₂ in the ordinary atmosphere, creating product Li₃N. The oxidation due to interaction with atmospheric oxygen, nitrogen, moisture, turns Li into a dull and dark gray color. So, we need to avoid the above chemical species from the air by creating vacuum in the glove box, while handling Li.

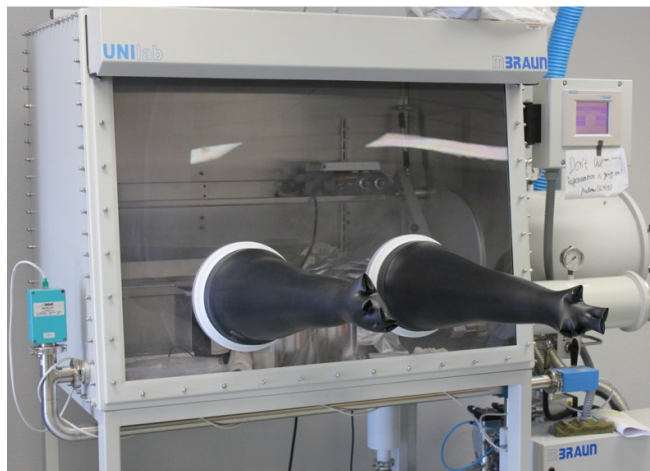


Fig. 1.20 Glove box to manipulate the objects in the inert atmosphere.

(I) Electrochemical Impedance spectroscopy (EIS)

Impedance spectroscopy is a reliable method for estimating electrochemical performance in the frequency region. The electrochemical studies like EIS, galvanostatic charging-discharging and CV were performed using (SP-150) BIOLOGIC. A traditional three-electrode system was used, with an active material (Sn@rGO-MnO₂, rGO-MnO₂ and α -MnO₂) coated titanium foil as a working electrode, a platinum counter electrode and Ag/AgCl as the reference electrode and 1M Na₂SO₄ solution was used as an electrolyte.



Fig.1.21 Bio-logic work station used for electrochemical studies

Electrochemical impedance is generally detected by applying an AC voltage to a system of electrolyte/electrode and detecting the current passing through the system. Presuming a sinusoidal voltage excitation, the effect to this voltage is an alternative current signal. The current signal can be revealed as a total of sinusoidal expressions. The voltage is a function of time, has the form

$$\sin(\omega t) E_0 = E \quad (18)$$

E_0 is the amplitude of the signal, ω is the radial frequency and E_t is the voltage at time t . The relationship between frequency f (expressed in hertz) and radial frequency ω (expressed in radians/second) is:

$$f2\pi = \omega \quad (19)$$

In a linear system, the response signal, shifted in phase (ϕ).

$$\sin(\omega t + \phi) I_0 = I \quad (20)$$

Ohm's Law permits us to estimate the impedance of the system as:

$$Z = E_t / I_t = Z_0(\sin(\omega t) / \sin(\omega t + \phi) I_0) = E_0(\sin(\omega t) / I_0 \sin(\omega t + \phi)) \quad (21)$$

The impedance is revealed in terms of a phase shift, ϕ and a magnitude, Z_0 .

With Eulers relationship,

$$\exp(j\phi) = j\sin\phi + \cos\phi \quad (22)$$

The, the impedance is expressed as a complex number,

$$Z(\omega) = Z(j\sin\phi + \cos\phi) = Z\exp(j\phi) \quad (23)$$

The equation for $Z(\omega)$ consists of imaginary part and a real. The imaginary part on the Y axis and the real part is plotted on the X axis of a chart, which gives us the "Nyquist plot". Here in this graph, it is to be observed that the y-axis is negative and that each point on the Nyquist plot is the impedance at one frequency. In Fig. 2-3 it has been illustrated that higher frequency data are on the left of the plot and lower frequencies are on the right side. On the Nyquist graph, the impedance can be revealed as a vector of length $|Z|$. The angle between the x-axis and this vector is ϕ ($=\arg Z$) and semicircle is a time constant (Macdonald 1987). Electrochemical Impedance graphs often possess quite a few semicircles. Frequently, only a portion of a semicircle is seen.

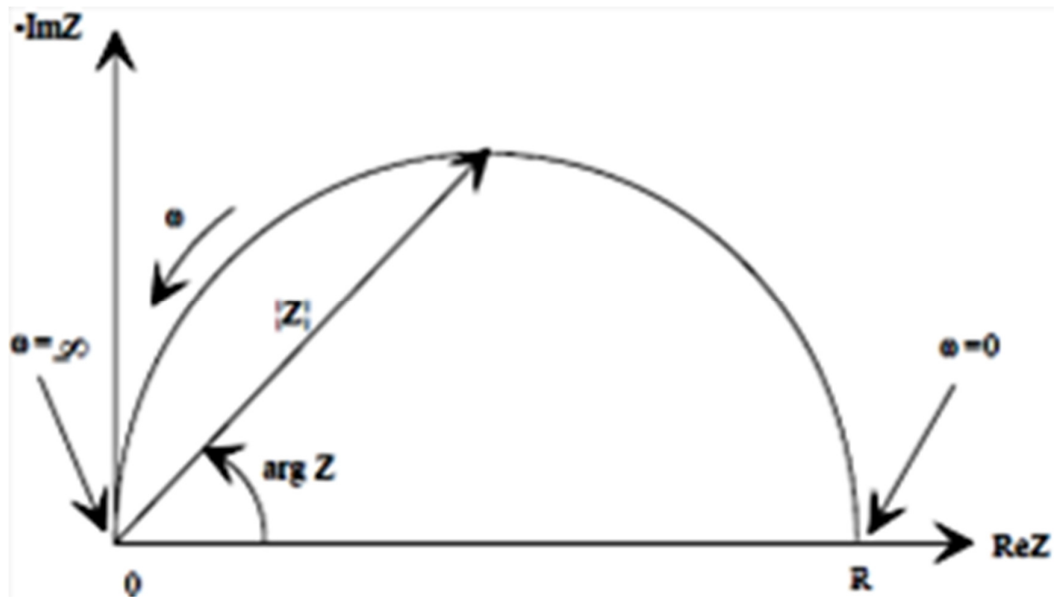


Fig. 1.22 Nyquist plot of Impedance Vector

1.9 Scope and Objectives of the Thesis

In the last few years, technologically important semiconducting nanostructure oxides, such as MnO_2 , NiO , and CuO have attracted enormous interest owing to their unique properties and potential use in applications, such as Li-ion batteries, solar cells, and electrochemical sensors. There are now increasing research interests in a wide range

of manganese and nickel based compound structures, due to their applications in catalytic activity for the sake of waste water treatment. Also, the electrochemical study of Silicon NWs for application as anode in Lithium ion battery is of particular interest, because it reduces the intrinsic problem of volume change in the bulk. Though, Si has highest theoretical capacity, it could not be used in battery due to above problems and draws more research insight by fabricating nanostructures.

The objectives of the present research work

- Growth, characterization and catalytic activity of MnO_2 and rGO/MnO_2 Nanowires (NWs). To study the structure-property correlation.
- Fabrication and characterization of MnO_2 , rGO/MnO_2 , Sn/rGO/MnO_2 NWs and their application as working electrode in the super capacitor.
- Fabrication and characterization of NiO and CuO Nanoparticles (NPs), and their application for the dye removal/photo-degradation of RB-5/MB/AY-23 from the aqueous solution (waste water).
- To study the structural and optical properties of the Silicon (Si) NSs
- To study the electrochemical behaviour of Si NWs for application as anode in Lithium ion battery and its correlation to physico-chemical properties

1.10 Organization of the Thesis

The thesis is organized as follows:

- Chapter 1 presents the overview of oxide semiconductor nanostructures, especially MnO_2 , NiO and CuO, and their structural and physical properties, preparation methods and characterizations. The chapter also includes various

industrial dyes such as RB-5, MB and AY-23, their physical, chemical properties and degradation methods. It also gives the brief description of the hydrothermal technique, modified Hummer technique to prepare rGO nanosheets. This is followed by a concise description of different characterization techniques.

- Chapter 2: The catalytic activity of MnO₂ nanowires towards dye (RB-5) degradation is also studied in this chapter. In addition, this chapter discusses the fabrication and testing of supercapacitor electrodes using synthesized pristine MnO₂, doped MnO₂ with reduced graphene oxide and Sn. Electrochemical characterizations are used to estimate the specific capacitance, energy density, and power density. The electrochemical impedance plot will be used to compare the performances of the working electrodes.
- Chapter 3 deals with the fabrication and characterization of NiO nanoparticles using thermal decomposition technique. Also, it contains the study on the effect of annealing temperature on the adsorption and photocatalytic properties of NiO nanoparticles towards RB-5 removal and MB degradation, respectively. This chapter also includes discussion on the growth and characterization of CuO nanoparticles by modified chemical precipitation technique. Also, it contains the results of photocatalytic effect of CuO nanoparticles towards dye, like RB-5, MB and AY-23 degradation under visible light irradiation. Finally, this chapter ends with the kinetics study in order to know the rate of degradation of respective dyes.
- Chapter 4 deals with the fabrication Si NSs using electrochemical etching technique, and the effect of current density and etching time on structural and optical properties of Si NSs. A testing of synthesized Si NWs as anode in Li ion

cell and the effect of cycling on the structural, optical and electrochemical properties of the anode is also discussed.

- Chapter 5 gives the summary and conclusions of the present work. The scope for further research work in this area is also discussed.

CHAPTER 2

GROWTH, CHARACTERIZATION OF UNDOPED AND TIN (Sn) &/ OR rGO DOPED MnO₂ NANOWIRES AND THEIR APPLICATIONS IN CATALYSIS AND SUPERCAPACITOR ELECTRODE

2.1 Introduction

The growth of MnO₂ nanowires and their application towards dye (RB-5) degradation is reported in this chapter. The effect of rGO nanosheets, on structural, optical, and catalytic properties of MnO₂ NWs is discussed. In addition, this chapter discusses the fabrication, testing and performance of supercapacitor electrodes using synthesized pristine MnO₂, doped MnO₂ nanowires with reduced graphene oxide and tin.

Synthetic colorants are extensively used in textile industries for dyeing and coloring of materials. Reactive Black 5 (RB5) dye is much familiar due to its special features such as solubility, the high shade of the color and easy attachment to the fiber. Once coloring is finished, the colored substrate is cleaned off few times to take away unattached and/or hydrolyzed dye. It means 15-50% of the industrial colorants is released in wastewater flow throughout dyeing process (Karatat et al. 2012). The loss of colorant in wastewater is very hazardous to human and aquatic life. There are several reports on the photocatalytic degradation of RB5 from various semiconductors such as SiO₂, SnO₂, Fe₂O₃, TiO₂, etc (Chong et al. 2015)(Chatterjee et al. 2010 p. 5)(Zhang et al. 2004). Recent studies like Weng et al. (2013) utilized Fe⁰ (ZVI) products, as a catalyst to decompose RB-5 by Fenton treatment. It is expected that ZVI aggregates provide a lot of iron ions, which leads to Fe precipitates like (Fe(OH)₃(s) and Fe(OH)₂(s)). The iron compounds restrain the reproduction of OH[•] and reduce the catalytic efficiency during the degradation of hydrogen peroxide. In Fenton process, a sufficient amount of the HO[•] radicals are required for the degradation of dyes (Zhang et al. 2006). Vyas et al. (2013) evaluated the photocatalytic activity of

TiO₂ for the elimination of RB-5 in aqueous solution. It was concluded that TiO₂ nanoparticles have lesser surface area and it absorbs less number of photons and dye species. In addition, occupied active sites on TiO₂ particles will repress the production of reactants, which results in a lesser decomposition rate of organic effluents.

To overcome the above drawbacks, Manganese dioxide (MnO₂) is considered due to its special properties like high surface reactivity, chemical stability, and large specific surface area. The reaction between H₂O₂ and Mn⁺² ions (chemically generated) leads to the huge quantity of OH[•] generation. The OH[•] species are able to attack colorants and cause chemical degradation of these products by H- abstraction, and addition to C - C unsaturated bonds (Cheng et al. 2014).

On the other hand, MnO₂ is well-known as electrode material for charge storage applications owing to the highest theoretical specific capacitance of 1370 F/g [80, 81]. Nonetheless, MnO₂ has some disadvantages such as slower ionic transport rate and lower energy density due to charge storage mechanism and its poor electrical conductivity. In order to enhance the catalytic activity, energy density and electrochemical cycling stability of MnO₂ electrodes, graphene and Sn nanostructures have been introduced (Wang et al. 2016 p. 2).

2.2 Experimental Procedure

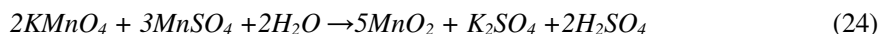
2.2.1 Synthesis of rGO nanosheets

Briefly, 23 ml of con. H₂SO₄ was taken into a 250 mL beaker filled with 1g of graphite flakes and 0.5 g of NaNO₃, afterward stirred it on a magnetic stirrer at 30 °C until creating a homogeneous mixture. Then 3 gm of KMnO₄ was slowly poured into the above mixture and continued to stir at 35 °C for half day. After that, 5 mL 30% H₂O₂ aqueous solution was mixed with the deep brown mixture till the complexion of the solution turned to bright yellow. The resulting mixture was centrifuged with D.I water and 5% HCl for 3-4 times to remove the organic residues and other metal ions in it as a result of the reduction of KMnO₄, then dried at 60 °C in a vacuum oven for

12 h. The obtained product was dispersed using ethanol and calcined at 150°C for 4 h to decrease GO into rGO.

2.2.2 Synthesis of MnO₂ NWs

The salts MnSO₄·H₂O and KMnO₄ were taken into a crucible and annealed at 500 °C for 3.0 h in an air oven. After liberating water molecules, 0.2 M of MnSO₄ was added slowly to 0.21 M (S1), 0.42 M (S2) and 0.63 M (S3) of KMnO₄ solubilized in 30 mL of D.I water. The above solution was stirred on a magnetic stirrer for 1 hour to form a homogeneous mixture. When the color of mixture turned to dark brown, it was shifted into a 100 mL of autoclave reactor and treated at 150°C for 24 hr. Then, the resultant solid brown color solution was centrifuged to eliminate impurities and dried at 55 °C in air. MnO₂ is resulted from the oxidation of MnSO₄ by KMnO₄ (oxidizer) from the following relation



2.2.3 Synthesis of rGO-MnO₂ and Sn@rGO-MnO₂

To obtain the rGO-MnO₂ composite, 0.2M MnSO₄ and 0.2M KMnO₄ were mixed with 35ml of Graphene Oxide (GO) solution of concentration 0.4 mg/mL. This reaction is stirred well for 30 minutes and then ultrasonicated for 15 minutes to ensure the dispersion of GO. Then the reaction mixture was transferred to a 50 ml hydrothermal autoclave system and kept at 150 °C for 24 hours. This was left to cool down to room temperature and then washed repeatedly with double distilled water and acetone. The sample was then dried at 60 °C for 15 hours. Sn@rGO-MnO₂ nanocomposite was prepared using 10 wt% of SnCl₂·2H₂O with addition of above prepared hydrothermal rGO-MnO₂ solution.

2.3 Results and Discussions

2.3.1 Structural and optical properties of undoped α -MnO₂ NWs

Fig.2.1 (a) depicts XRD spectra of the MnO₂ NWs grown hydrothermally at the different concentration of KMnO₄. The XRD peaks of all samples were matched to the tetragonal α -MnO₂ phase (JCPDS Card No.44-0141) with a space group $I 4/m$ and lattice constants of $c = 2.863 \text{ \AA}$, $a = 9.784 \text{ \AA}$. At lesser quantity of oxidizer, the crystallite is smaller, resulting in broad XRD peak (Wang and Li 2003). At greater quantity, larger crystallite is created and therefore the peak breadth reduces, therein intensity enhances, indicating the increase in the crystallinity of α -MnO₂.

The mean size of the crystallite of MnO₂ NWs is calculated via Eq. (1) at maximum diffraction peak (211). The crystallite size of MnO₂ NWs was found to be 15 to 25 nm. The mean crystallite size enhances with the enhance in oxidizer molarity as shown in Table 2.1.

Table 2.1 the structural and optical factors of α -MnO₂ NWs synthesized at the various quantity of oxidizer.

Molarity (M) of oxidizer	Surface Area ($\times 10^{-3} \mu\text{m}^2$)	Crystallite size(nm)	Band gap (eV)	Minimum dislocation density ($\times 10^{15} \text{ m}^{-2}$)
0.21	1.35	15.1	2.55	4.1
0.42	2.37	18.4	1.65	3.3
0.63	4.22	24.6	1.27	1.8

Additionally, minimum dislocation density has been determined using Eq. (6). The dislocation density decreases with the increase in the concentration of KMnO₄ due to a decrease in the number of grain boundaries and lattice defects with an enhance in the average crystallite size of MnO₂NWs. The related values are tabulated in Table 2.1.

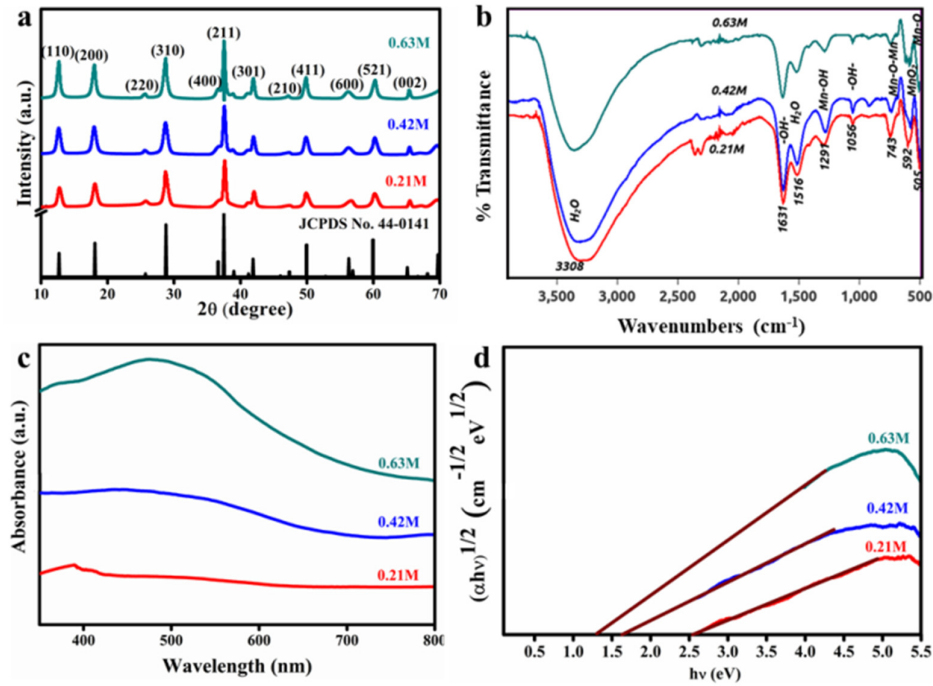


Fig. 2.1 (a) XRD, (b) FTIR, (c) UV-vis and (d) band-gap spectra of NWs like of α - MnO_2 nanostructures with different oxidizer contents

The FT-IR spectra for MnO_2 are shown in Fig. 2.1 (b). The band around 3308.36 and 1631.12 cm^{-1} correspond to O-H vibrating mode and is due to physically adsorbed water on the MnO_2 crystal from the environment (Henry et al. 2013). The band at 1056-1290 cm^{-1} is due to the Mn-OH stretching vibrations, and peak at 1516 cm^{-1} is attributed to hydration water of MnO_2 . A sharp peak due to Mn-O vibrations was assigned at 505 cm^{-1} in the spectra of MnO_2 , and some humps are detected around 743 cm^{-1} and 592 cm^{-1} due to the bending vibrations of α - MnO_2 (Jiang et al. 2009). No major change was observed in the FT-IR spectrum of MnO_2 NWs attained from the various quantity of KMnO_4 .

The absorption spectrum and band gap energy (E_g) for α - MnO_2 NWs are illustrated in Fig. 2.1 (c -d). It is observed that a single broad peak in the visible spectrum is due to the d-d orbital transition of manganese ions in the MnO_6 octahedra of the MnO_2 NWs (Toufiq et al. 2014). The absorption peak shifts towards the higher wavelengths with

increasing concentration of KMnO_4 because of the high density of energy levels ensuing from the high surface to volume ratio. However, as shown in Table 2.1, E_g decreases with increasing oxidizer molarity, which can be attributed to the decrement of the lattice defects and enhancement of transition manganese (II) ion quantity (Sakai et al. 2005).

Fig. 2.2 reveals that all MnO_2 samples analyzed with SEM show nanowire morphology at different magnifications, the diameter and length of the NWs enhance with the increase in the quantity of oxidizer. At lesser quantity of the oxidizer, the nucleation is heterogeneous, ensuring a shorter NWs. Conversely, at higher oxidizer quantity, MnO_2 nuclei are formed very shortly, due to homogeneous nucleation, resulting in a larger and longer size NWs. By image J Software, we could obtain the surface area of NWs, which also increases with oxidizer quantity as shown in Table 2.1.

Fig. 2.3 (a-c) shows the high-resolution TEM bright-field images of MnO_2 products heat treated at 150°C . It can be observed that the synthesized products consisted of nearly wire shaped particles with a size around 10-20 nm. The lattice fringes can be seen from the HRTEM image as shown in (Fig. 2.3 (B)), in which inter planar distance is determined to be about 0.24 nm, which are consistent with the d spacing of (211) of simple tetragonal MnO_2 . From HRTEM image the unidirectional fringe patterns are clearly observed, which indicates single crystalline nature of MnO_2 NWs.

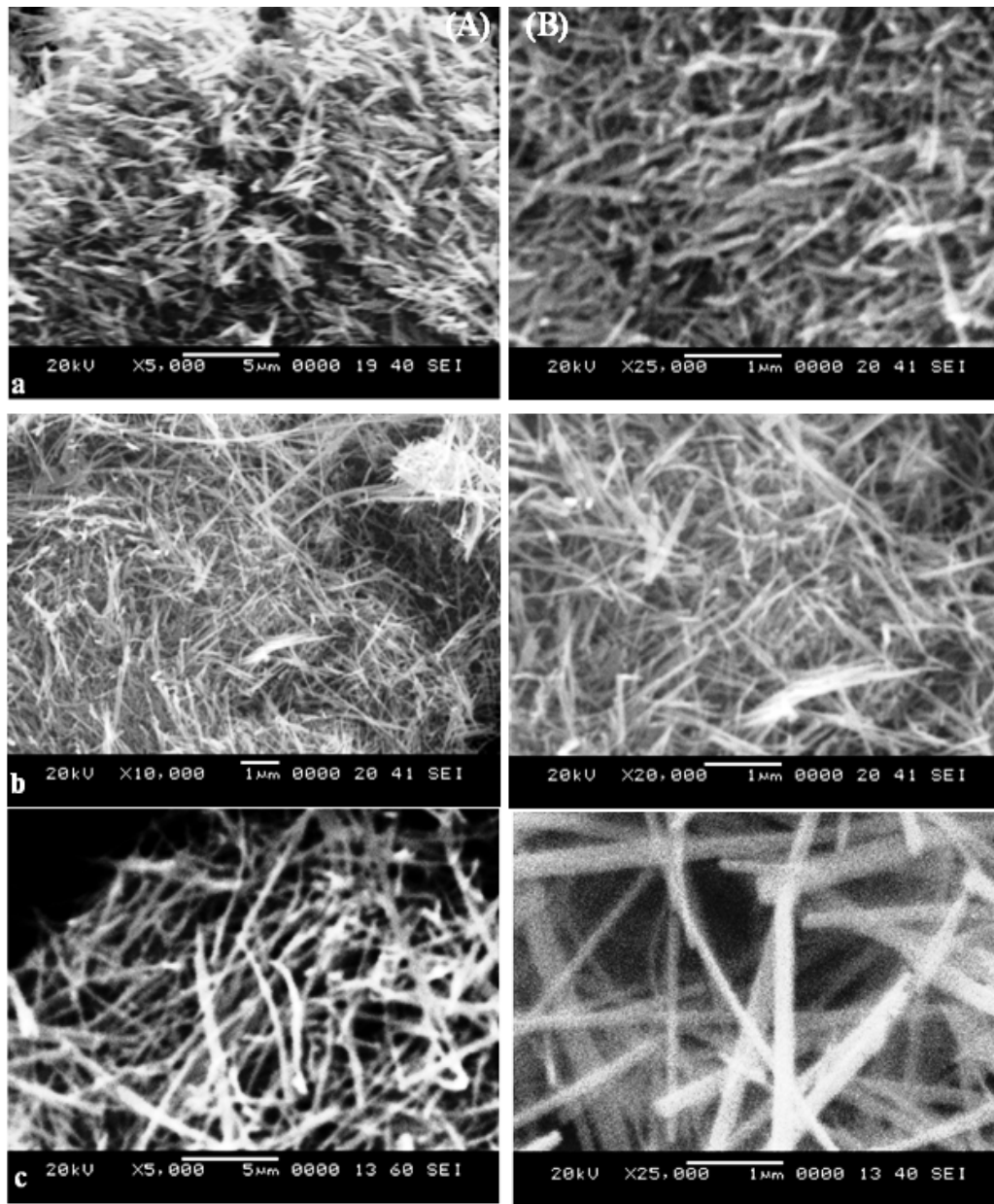


Fig. 2.2 (A) Low-magnification and (B) High magnification of SEM images of α - MnO_2 NWs at oxidizer concentration (a) 0.21 M (b) 0.42 M and (c) 0.63 M.

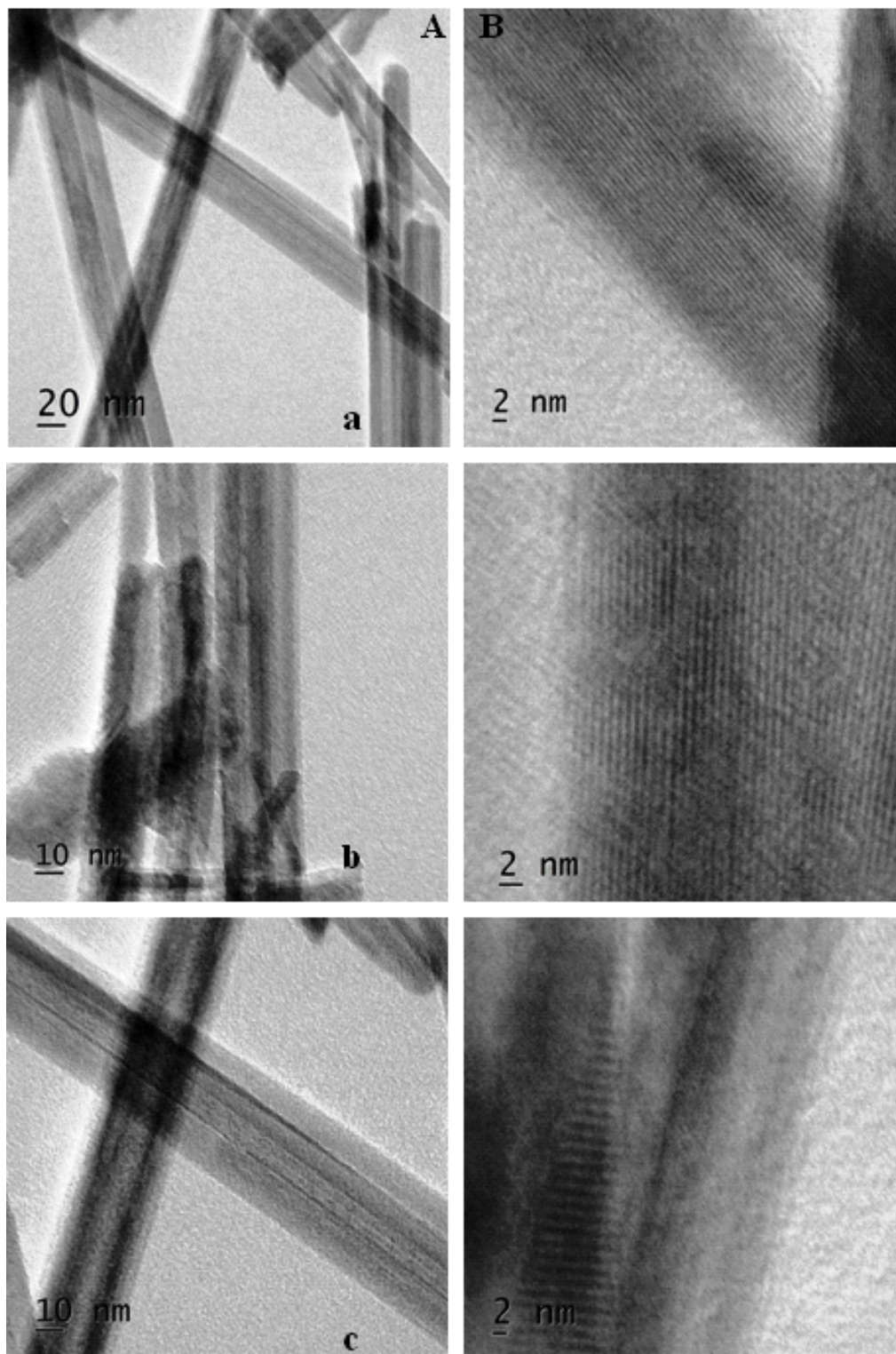


Fig. 2.3 (A) Low-magnification and (B) High magnification of HRTEM image of α -MnO₂ NWs at oxidizer concentrations (a) 0.21 M (b) 0.42 M and (c) 0.63 M.

From EDS analysis (Fig. 2.4) it was found that the NWs are composed of the following elements: Mn, O and K. The peak of K was caused by the very small amount of potassium in the synthesized products because the structure of MnO_2 consists of double chains of edge-sharing MnO_6 octahedra to form 1D (1×1) tunnels; it attributes to accommodate the K ions. The production yield of MnO_2 NWs is above 90% based on Mn quantity in the starting reagents.

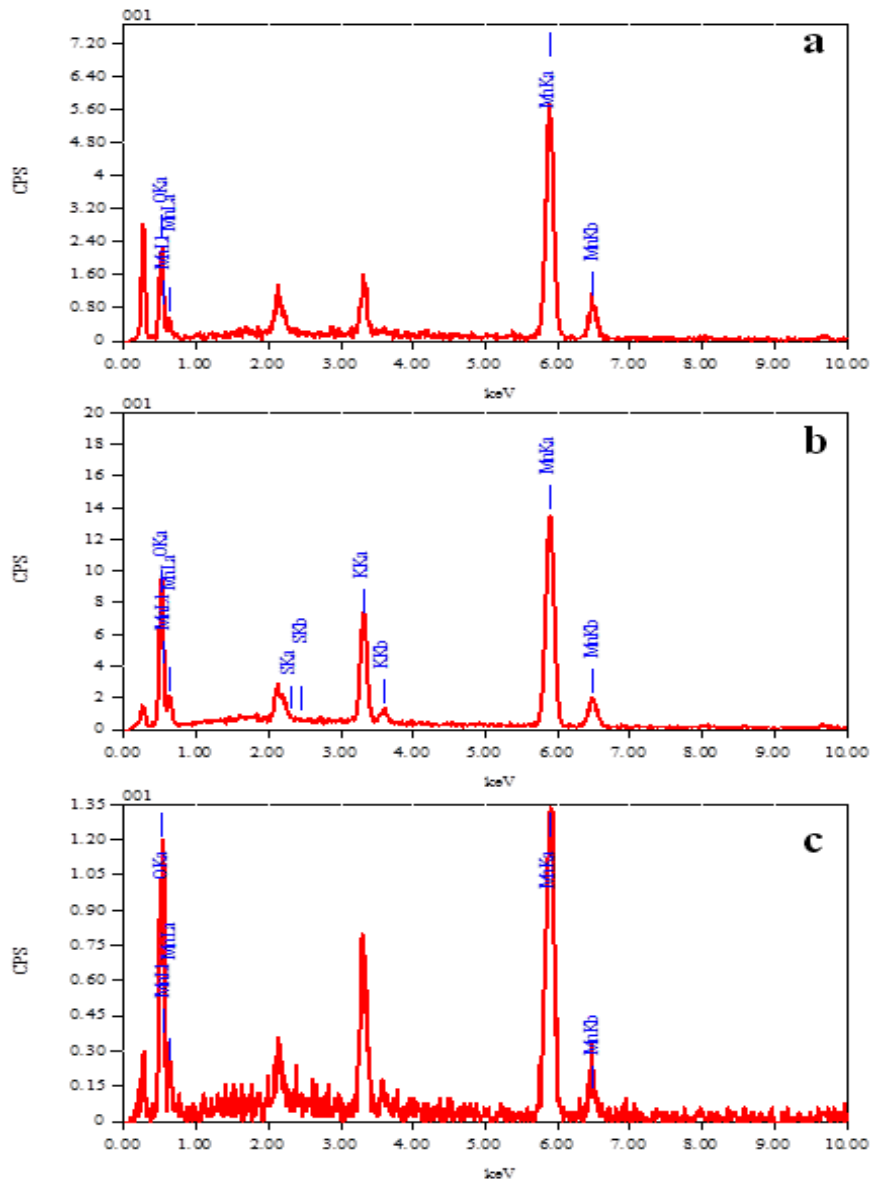


Fig. 2.4 EDS images of $\alpha\text{-MnO}_2$ NWs at oxidizer concentrations (a) 0.21 M (b) 0.42 M and (c) 0.63 M.

2.3.2 Structural and optical properties MnO₂ nanocomposites

Fig. 2.5 (a) shows the Raman spectra of Sn@rGO-MnO₂, rGO-MnO₂ and MnO₂ hybrids. Three distinctive peaks located at 506, 565, and 648 cm⁻¹ are identified for the MnO₂ NWs. The Raman band at 648 cm⁻¹ and 565 cm⁻¹ is due to the symmetric $\nu_2(\text{Mn-O})$ and $\nu_3(\text{Mn-O})$ stretching vibration of MnO₆ groups, respectively (Li et al. 2012). The Raman band located at 506 cm⁻¹ is in good agreement with the translational motion of the MnO₆ octahedra, thus revealing birnessite-type α -MnO₂. The rGO is characterized by two specific features, G band (the E_{2g} mode of sp²-hybridized C-C bonds) at 1596cm⁻¹, and D band (defects) at 1345.8 cm⁻¹. As shown in Fig. 2.5 (a), the Raman D/G intensity ratio is reduced slightly from 0.99 for rGO nanosheets to 0.97 for rGO/MnO₂ NWs due to the larger in-plane sp² domains are formed during the reduction of GO (Ma et al. 2016a).

Fig. 2.5 (b) shows XRD of synthesized nanocomposites. The related diffraction peaks were indexed and matched well with the body-centered tetragonal phase [JCPDS, No. 44-0141, a = b = 9.7847Å and c = 2.8630Å]. The appearance of the broad diffraction peak at 23.7° in rGO/MnO₂ reveals the presence of rGO on the surface of MnO₂ NWs (Fu et al. 2013). The average grain size of prepared nanoproducts is obtained using eqn 5. The measured grain/crystallite size of undoped and rGO &/or Sn doped MnO₂ NWs is in the range of 10-8 nm. Using the above crystallite values, the dislocation density has been estimated using Eq. (2). As shown in Table 2.2, Sn@rGO doped MnO₂ NWs consist of more dislocations compared to undoped MnO₂ NWs due to the existence of interfaces between the MnO₂ lattice and Sn@rGO nanosheets (Abdolhosseinzadeh et al. 2015).

Table 2.2 The structural parameters of pristine and doped α -MnO₂NWs.

S.No	Naomaterials	Crystallite size (nm)	Dislocation density (10 ¹⁶ m ⁻²)	BET Specific surface area (m ² /g)
1	Sn-rGO-MnO ₂	8.11	1.52	55.8
2	rGO-MnO ₂	8.40	1.42	59.1
3	MnO ₂	10.00	1	37.7

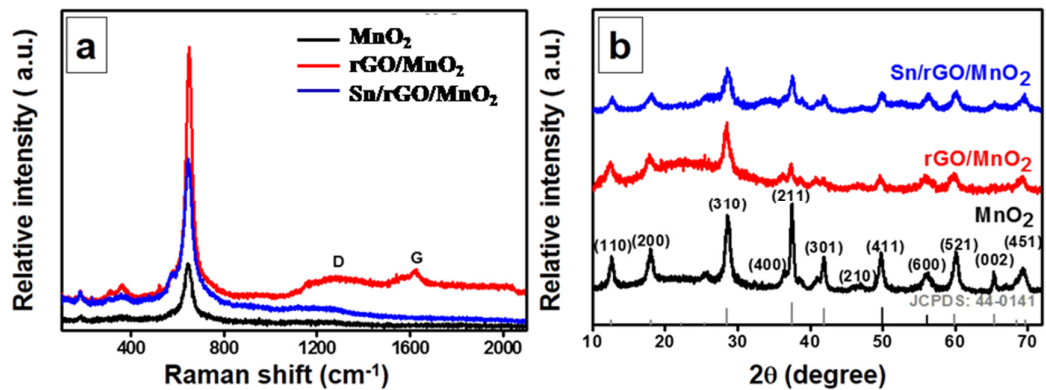


Fig. 2.5 (a) XRD and (b) Raman spectra of NWs like various α -MnO₂ based nanostructures.

Fig. 2.6 (A) shows SEM micrographs of MnO₂ nanocomposites. As-shown in Fig. 2.6 (B-C), all the nanocomposites reveal shape of NWS and rGO single atomic layers wounded over the NWs due to the strong electrostatic interaction between the manganese ions and carbon ions during the hydrothermal process. During reaction with GO, the solution became cloudy resulting in the formation of a large number of MnO₂ nuclei in a short time, leading to the larger diameter of NWs. Thus resulting in a higher surface area. By BET (Fig. 2.7) the specific surface area measured for pristine MnO₂ NW is about 37.7 m²/g, whereas for rGO/MnO₂ NWs is about 59.1 m²/g. The enhanced surface area of rGO/MnO₂ NWs is due to the more pore volume as shown in Table 2.2 (Samejima et al. 1977). Fig. 2 (B-a) shows the rippled morphology of the rGO sheets, bundling MnO₂ NWs at lower magnification. Hence, from SEM and Raman studies, it is evident that MnO₂ NWs are wrapped with rGO sheets, which prevents the agglomeration of MnO₂ NWs. The inset in Fig. 2.6 (B-b) shows the morphology of rGO which appeared as a single sheet with wrinkled surfaces after exfoliation (Kakaei and Hasanpour 2014).

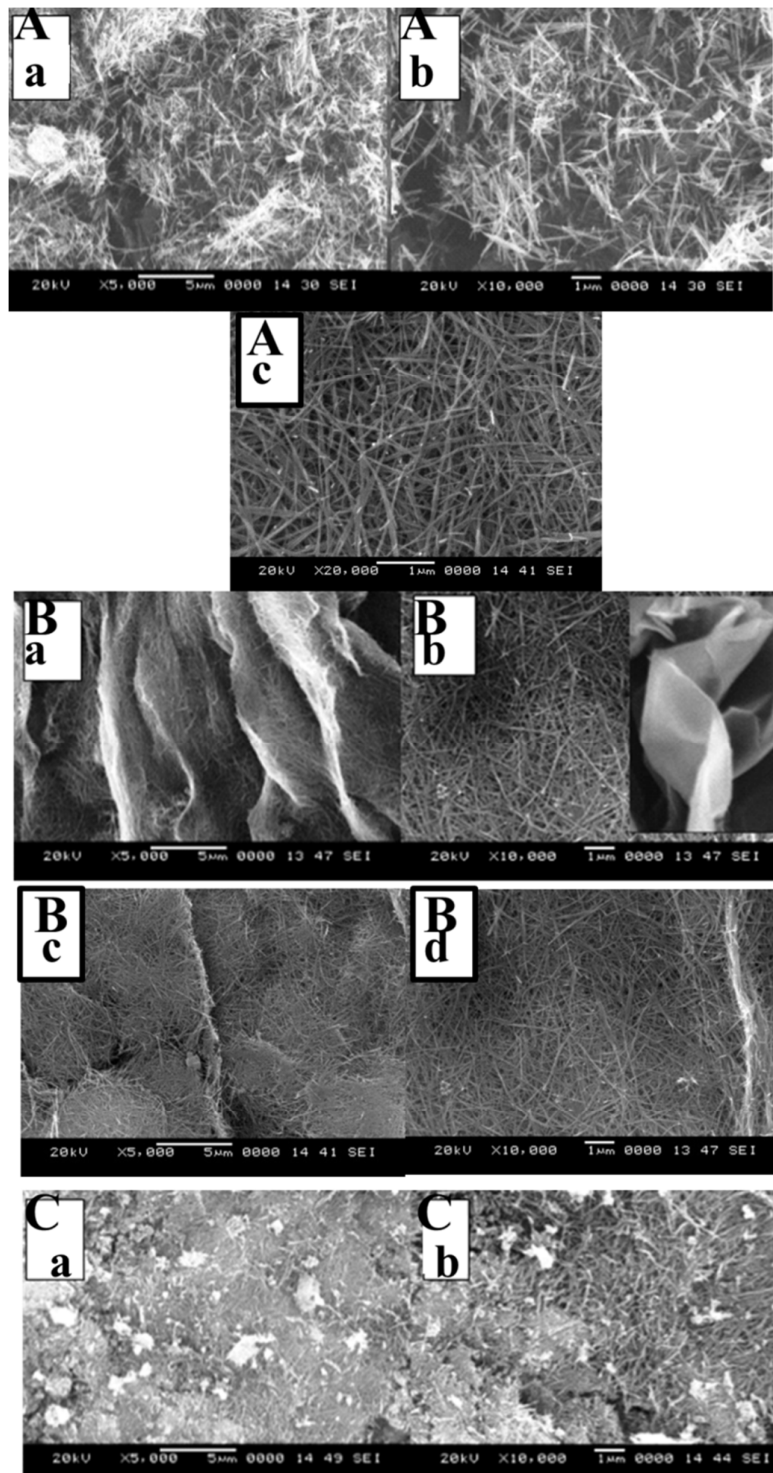


Fig. 2.6 SEM images of (A) MnO₂ NWs at the various magnification (a, b, c = 5k, 10k, 20k), (B) rGO-MnO₂ NWs (a-c, b, d= 5k, 10k, 20k) and (C) Sn-rGO-MnO₂ NWs (a, b=5k, 10k), respectively. k=1000 in number

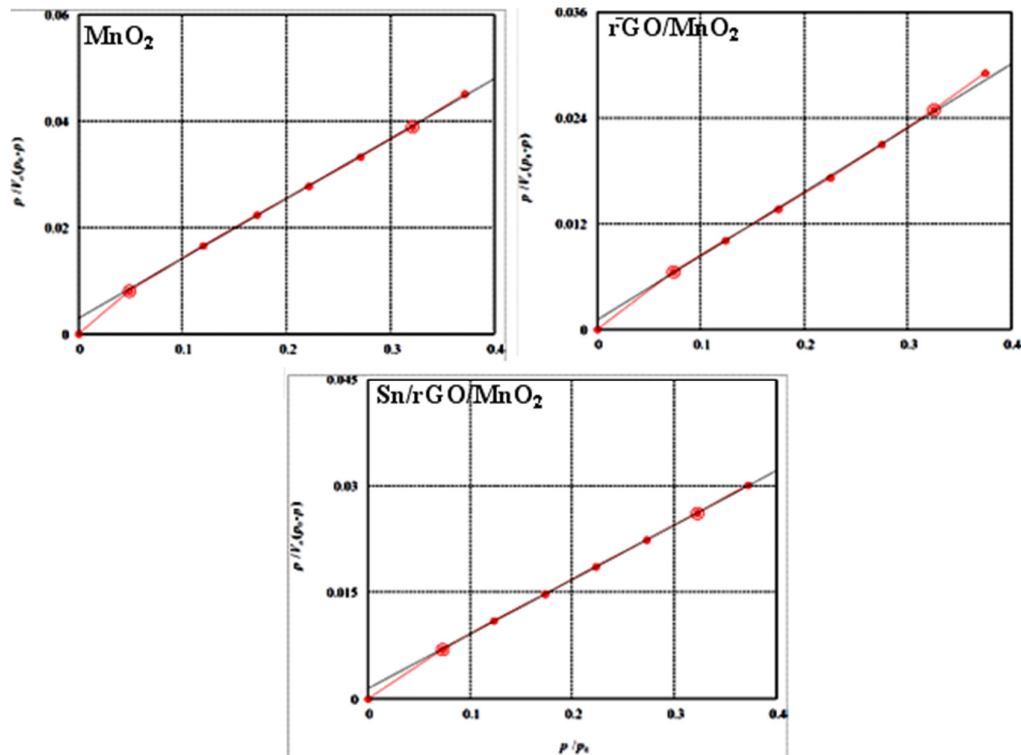


Fig. 2.7 BET surface area images of (a) MnO₂, its nanocomposites using (b) rGO and (c) Sn@rGO.

Fig. 2.8 (a) depicts the lower-magnification HRTEM micrographs of MnO₂ and its nanocomposites using rGO. The micrographs, as shown in Fig. 2.8 (b), reveal a single set of parallel planes with inter atomic spacing of 0.241 nm for MnO₂ NWs and 0.133 nm for rGO/MnO₂ NWs, which are in good agreement with the [211] and [541] planes observed in the XRD spectrum. The SAED micrographs are shown in the inset of Fig. 2.8 (b) indicates simple tetragonal crystalline structure of MnO₂ and its nanocomposites using rGO.

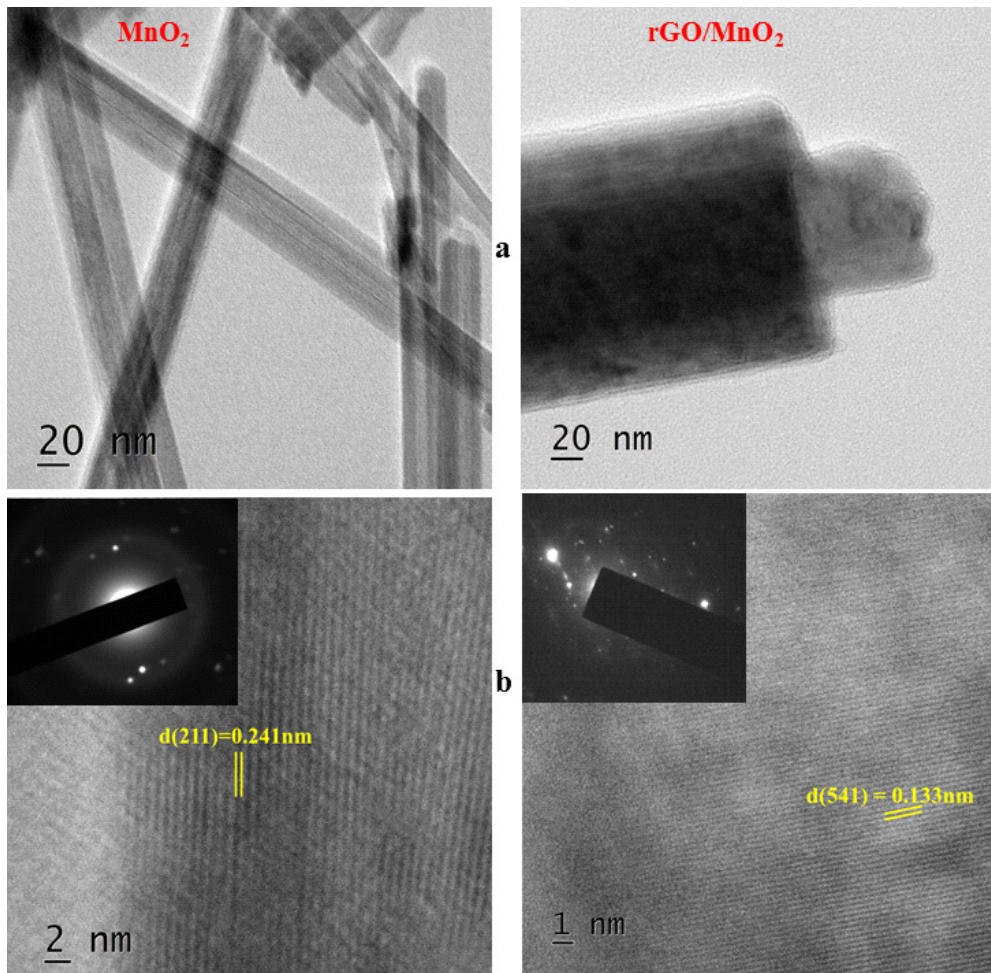


Fig. 2.8 (a) Low and (b) high magnification of NWs like MnO₂ based nanostructures. The inset of b displays the SAED pattern of NWs.

2.4 Applications:

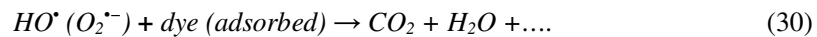
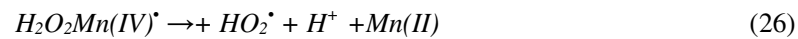
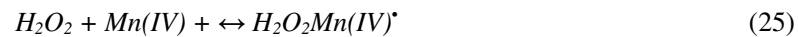
2.4.1 Catalysis

2.4.1.1 Catalytic Properties of pure MnO₂ NWs

The catalytic activity was performed in a 250 mL borosil beaker, which contained 1×10^{-5} M, PH5, of the RB5 solution, 100 mL of D.I water, and 20 mg of catalyst MnO₂. After taking 6 mL of hydrogen peroxide in it, the resultant solution was permitted to stir on the magnetic stirrer at room temperature. Later, this solution was

immediately filtered with PVDF membrane paper to take out the catalyst particles from the suspension. The remaining dye solution to be quantized using a UV–Vis spectrophotometer within an equal interval of time.

We propose a Fenton process for the RB-5 dye decolorization by MnO₂ NWs, as shown in Fig. 2.9. The reaction mechanism involves free radical species governed by the following equations (Yu et al. 2014):



The mechanism is followed by a desorption-oxidation-adsorption process as shown in schematic Fig. 2.8A. The first step in reactions is the adsorption of H₂O₂ over the surface of MnO₂ NWs, Eq. (25), which is proceeded by the breakdown of H₂O₂ into free primitive species, such as HOO[•], or HO[•], O₂^{•-} primitive species, Eqs. (26) – (29). The formed chemical groups (O₂^{•-}, HO[•]) contain the high oxidative capability to decolorize the adsorbed colorants to H₂O, CO₂, or other tiny products, Eq. (30). The created tiny products from the dye decolorization could rapidly leave from the MnO₂ NWs surface by desorption and the MnO₂ NWs is thus regained. The generated free radical species from H₂O₂ are acted by two ways. One way is that free primitive groups speedily oxidize the colorants. Another way is that the created free primitive species join each other and form O₂, Eq. (31), but O₂ cannot break up the colorants.

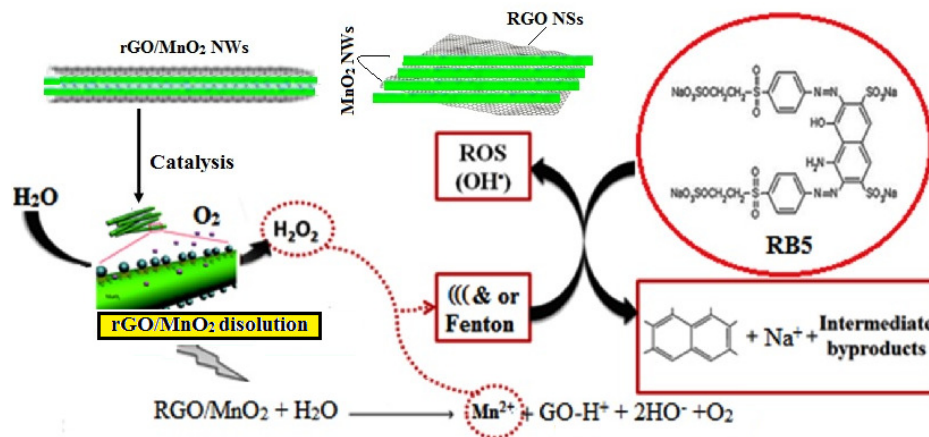


Fig. 2.8A The schematic showing application of rGO/MnO₂ NWs for decompositions of RB5.

Fig. 2.9 (a) depicts the optical spectra of RB-5 at the different quantity of oxidizer. The absorbance of RB-5 dye was detected with respect to the reaction time at the maximum wavelength (λ_{max}) of 596 nm. By increasing the reaction time, a large amount of dye elimination or less absorbance is expected due to the high amount of OH[•] species followed by the speedy break up of H₂O₂ (Laohaprapanon et al. 2015). Meanwhile, the slight blue shift of peak at 596 nm mentioned the catalytic decolorization of the dye.

Fig. 2.9 (b) shows the estimation of the degradation rate of RB5 by plotting in decolorization (%) Vs reaction time (t) for various amount of KMnO₄. The decolorization percentage was calculated according to the Eq. (12). At the time of 60 min, the dye removal efficiency was estimated to in the range of 70-30 % with respect to the molarity of KMnO₄ in the range of 0.21-0.63 M, respectively.

The improved catalytic efficiency can be revealed in terms of surface area. According to Table 2.2, as for enhance in the molarity of oxidizer, the surface area of NWs increases. Hence, the enhance in the surface area of NWs results in enhanced in a number of MnO₂ active sites on the surface enhances, which in turn enhances the number of colorant and H₂O₂ species being attached to the surface of NWs. It enhances the amount of O₂^{•-} and [•]OH free primitives striking the colorant molecules, resulting in an increment of decolorization (Mehta et al. 2011).

The stability of catalyst is also a prime factor in Fenton catalysis. Results pointed out that the yields of NWs decrease only from 67 to 63% with increase in the cycle number from 1 to 5 (Fig. 2.9 (c)). It might be due to the accumulation of by-products in the cavities of the active surface sites of the catalysts or loss of some amount of catalyst that attaches to the membrane paper during the filtering process. It reveals that the catalyst α - MnO_2 NWs grown via hydrothermally is a capable catalyst for RB-5 decomposition.

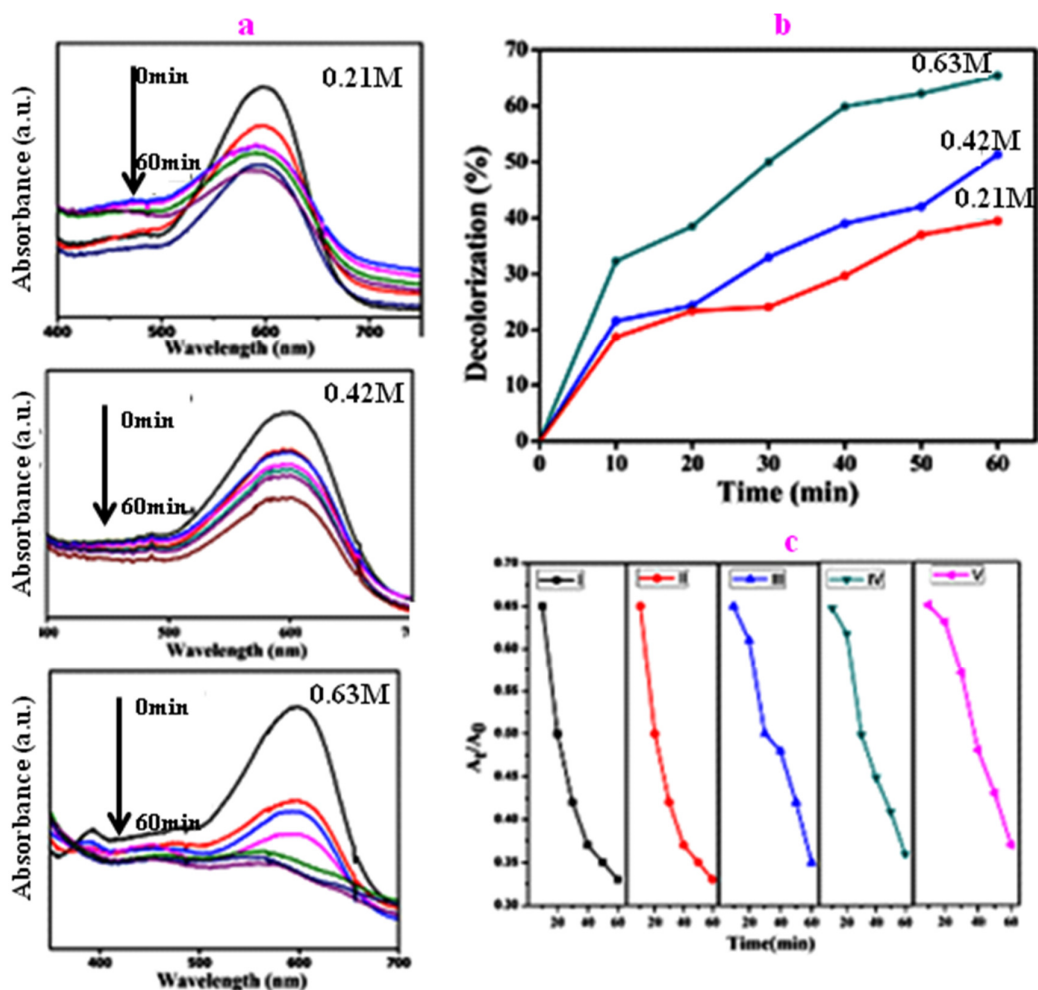


Fig. 2.9 (a) RB-5 dye concentration spectra over the MnO_2 NWs with different oxidizer contents, (b) Fenton decomposition of MnO_2 NWs with different oxidizer contents and (c) Reusability of MnO_2 NWs prepared at the oxidizer content of 0.63M

2.4.1.2 Catalytic Properties of rGO/MnO₂ NWs using Fenton and sono-Fenton process

The catalytic activity of the products was tested in a 250 mL borosil glass beaker, which contained 1×10^{-5} M of RB5 solution, 100 mL of distilled water, and 20 mg of catalyst MnO₂ or rGO/MnO₂, PH=5. After mixing 6 mL of 30 wt% hydrogen peroxide solutions, O₂ bubbles were produced simultaneously. The resulting mixture was stirred till attaining the adsorption/desorption equilibrium. In addition, an rGO/MnO₂ stock solution was dispersed with a probe sonicator (frequency $\sim 20 \pm 2$ kHz and power ~ 120 W). The tip of the horn was 1cm in diameter and 6 cm in length. A constant temperature of 40 ± 2 °C was maintained by circulating water and pH was again tuned to a predetermined value using H₂SO₄ or NaOH solution. Sono-Fenton experiments were performed in a 50 mL polypropylene beaker at a regular time interval from 0 min to 60 min. The samples named as MnO₂, rGO/MnO₂, and US/rGO/MnO₂ were used for catalysis. After achieving the complete adsorption/desorption equilibrium state, the analytical samples (5 mL) were taken out from the solution in the regular time interval from 0 min to 60 min. Subsequently, the sample was washed away with water to separate catalyst from it and the remaining solution was monitored using UV-Vis spectroscopic techniques to measure the dye concentration.

Fig. 2.10 (a) shows the plot of absorption vs wavelength of RB5 based on the ultraviolet visible absorption spectra as a function of the catalytic reaction period for the various catalysts. The intensity of the maximum absorption peak of the RB5 gradually shifts towards the lower wavelength with respect to the time, which is known as blue shift, referred the catalytic decay of the RB5 (Weng et al. 2013). Eventually, the unique absorption peak became wide and weak in the intensity, indicating the decolorization of RB5.

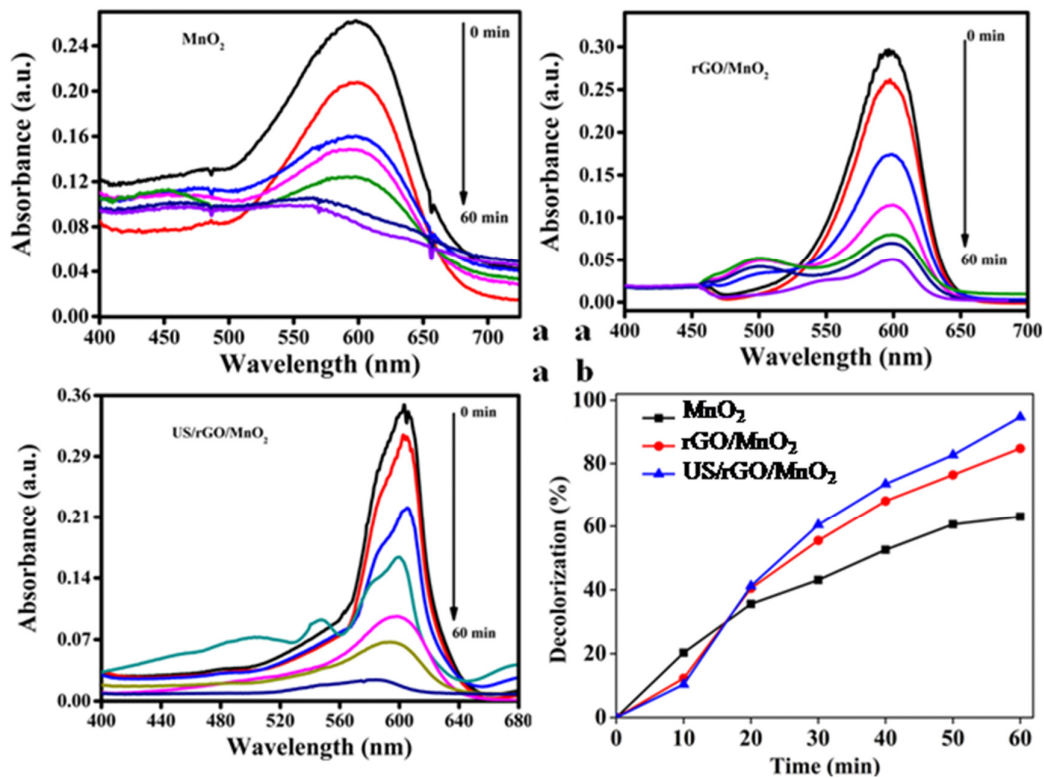


Fig. 2.10 (a) RB-5 dye concentration and (b) the % decolorization of RB-5 over MnO_2 based catalysts as a function of time.

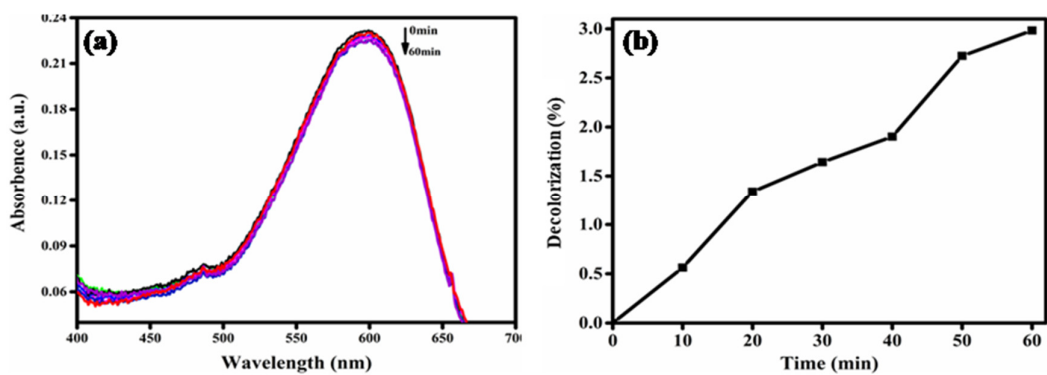


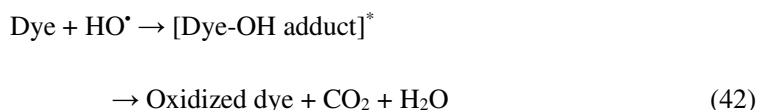
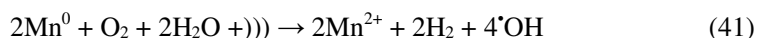
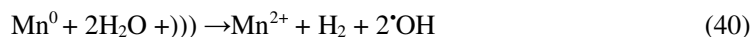
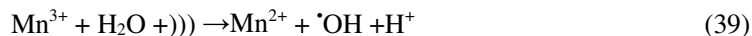
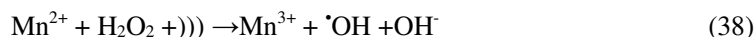
Fig. 2.10A Time dependent (a) concentration and (b) decolorization percentage of RB5 in the sonolysis process.

Fig. 2.10 (b) shows the estimation of the degradation rate of RB5 by plotting in decolorization (%) vs reaction time (t) for three different catalysts. The color removal efficiency was estimated using Eq. (8). It may be noted that the use of MnO_2 , rGO/MnO_2 , and US/rGO/MnO_2 as a catalyst resulted in the decolorization rate of 63 %, 84 % and 95 % in 60 min, respectively. We suggest the same mechanism (Fenton) as described in the earlier section for the degradation of RB5 using the catalyst of MnO_2 and rGO/MnO_2 . As seen in the Fig. 2.10A, the sonolysis process itself resulted in the decolorization rate of 1.35 % in only 20 min and as high as 3% in 60 min. The results clearly indicate the significant reduction in the sonolysis than Sono-Fenton process and Fenton's alone, due to the reduction of radical generation and slower catalytic reaction between the reagents.

The highest catalytic performance of rGO/MnO_2 towards the degradation of RB5 is attributed to the synergistic effects between rGO and MnO_2 in the presence of H_2O_2 . Graphene with 2D layers of sp^2 -bond structure can provide strong chemical and mechanical interactions, as well as increased electron transport between MnO_2 NWs and rGO matrix (Qu et al. 2014). The RB5 molecules are easily adsorbed to the surfaces of GO through π - π conjugation based on its giant π -conjugation frame and two-dimensional planar configurations until the adsorption-desorption equilibrium. This accounts for the high quantity of OH^\bullet on the surface of rGO doped MnO_2 NWs compared to undoped MnO_2 .

To study further degradation of RB5, we combined ultrasonication to Fenton reagent using rGO/MnO_2 catalyst. In sono-Fenton process, the collapse of the cavitation bubbles leading to the generation of high pressure and temperature. These high-energy phenomena cause disintegration of pollutants in aqueous solutions. The heat from the cavity collapse divides H_2O molecules into reactive H and OH radicals (Eq. 32). The OH radicals come together to create H_2O_2 and hydrogen radicals come together to create molecular hydrogen {Eqs. (33-34)}. In the meantime, oxygen and H_2O_2 molecules from the aqueous solution reason creation of oxide and other radicals (Eq. 35-36), where [U]] refers the ultrasound. rGO/Mn-OOH^{2+} degenerate into OOH^\bullet and Mn^{2+} (Eq. 37) due to a synergetic effect amid ultrasound and Fenton's reagent. The separated Mn (II) ions can react finally with H_2O_2 to create OH radicals, leading

to a cyclic process (Bagal and Gogate 2014). Hence, the synergy of Fenton's and ultrasound together increases the reaction rate of Mn^{2+} isolation from $Mn-OOH^{2+}$ and accelerates the OH radical formation due to the reaction among Mn^{3+}/H_2O Mn^{2+}/H_2O_2 or Mn^0/H_2O , or as shown in Eqs. 38-41. The generated OH radicals decompose the adsorbed RB5 molecules to CO_2 , H_2O (Eq. 42)



From Fig. 2.10 (b), after 60 min, the decolorization efficiency in Fenton's route is 84.5%. Nevertheless, in the same time, sono-Fenton route results in about 95% degradation. The results obviously point out the remarkable enhancement in sono-Fenton route than Fenton's route could due to the synergistic effects. The maximum decolorization efficiency of RB5 in the current work is comparatively more than the literature values, as given in Table 2.3. rGO@MnO₂ NWs catalyst shows superb performance in terms of short reaction time, efficiency and low dosage.

Table 2.3 Reported values for decolorization of RB5 using MnO₂ and GO.

Material	Method	Catalyst dose (mg)	RB5 Dye concentration	Degradation (%)	Time (min)	Ref
α -MnO ₂	Fenton	20	1×10 ⁻⁵ M	38	60	(Ramesh et al. 2016)
Mn-alginate	Fenton	6000	air flow 1 L/min	98	100	(Fernández de Dios et al. 2015)
MnP	Biodegradation	20	25 mg/L	80	90	(Mahmoudian et al. 2014)
GO	Fenton	300	1×10 ⁻⁵ M	57-75	5h	(Cheng et al. 2012)
Magnetic GO	Fenton	20	20 mL	62	60	(Ali et al. 2014)
rGO	Photo catalytic	30	10 mg/L	26	60	(Wong et al. 2015)
GO NPs	Fenton	1000	1×10 ⁻⁵ M	80	2h	(Kyzas et al. 2014)
Fe alginate	Fenton	500	2.68 mM	85	60	(Iglesias et al. 2013)[106]
FO	Fenton	100	100 mg ⁻¹	68	120	(Meriç et al. 2004)
Fe	Fenton	300	50 mg ⁻¹	63	120	(Rahmani et al. 2010 p. 5)
FeSO ₄	Fenton	250	50 mg ⁻¹	63	20	(Lucas and Peres 2006)
NiO/Al ₂ O ₃	Fenton	200	100 mg ⁻¹	53	250	(Bradu et al. 2010)
CuO/Al ₂ O ₃ /phospahte	Fenton	200	100 mg ⁻¹	37.5	250	-----
β - MnO ₂	Fenton	160	40 mg ⁻¹	56	40	(Yu et al. 2014)
α - MnO ₂	Fenton	20	1×10 ⁻⁵ M	63	60	Present work
rGO/ α -MnO ₂	Fenton	20	1×10 ⁻⁵ M	84	60	Present work
rGO/ α -MnO ₂	Sono-Fenton	20	1×10 ⁻⁵ M	95	60	Present work

The degradation yield formed at the end of reaction period (60 min) was estimated by GC–MS and recognized with mass spectra data for different catalysts (20 mg L⁻¹ each) of MnO₂ (Fig. 4a), rGO/MnO₂ (Fig. 4b) and US/rGO/MnO₂ (Fig. 4c).

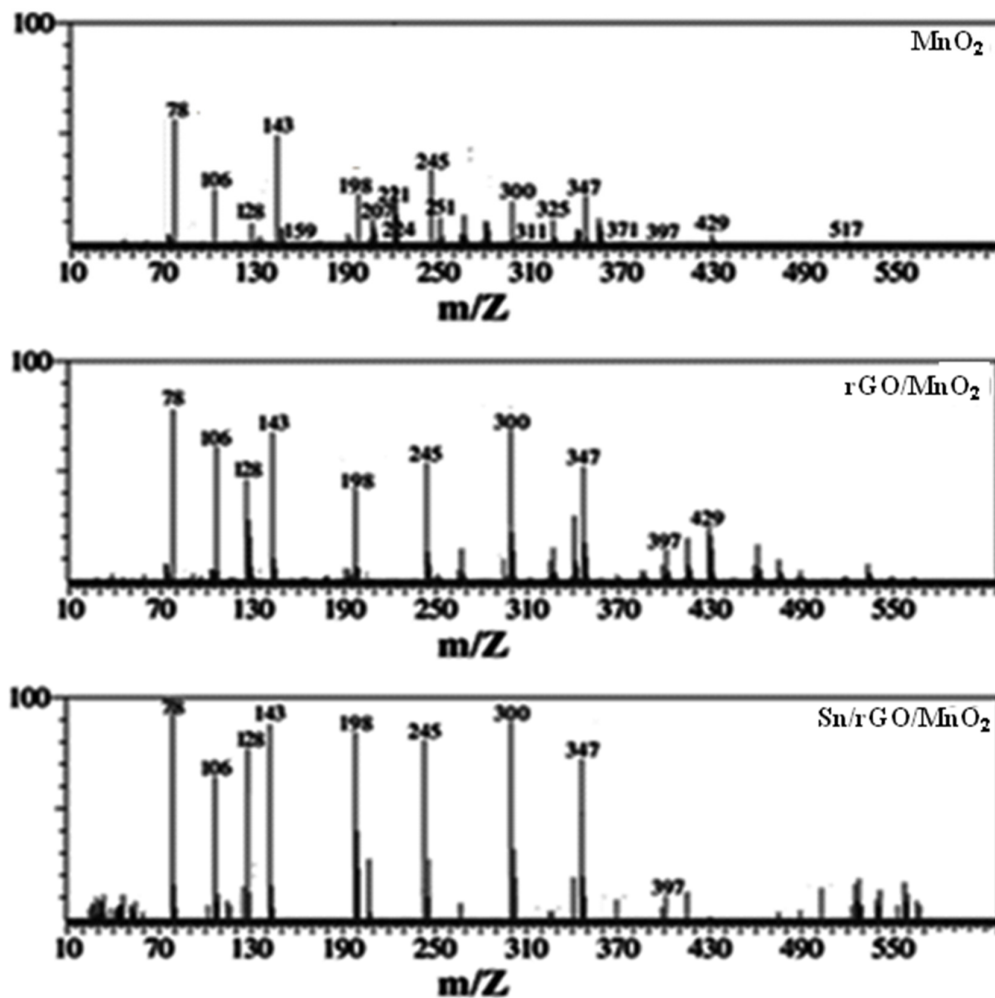
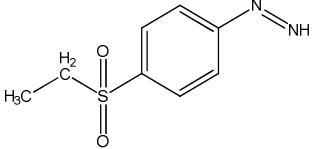
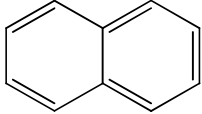
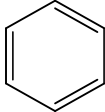
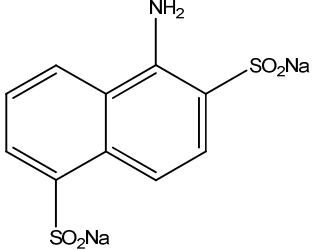
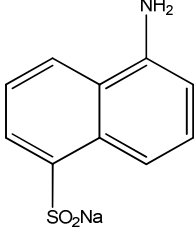
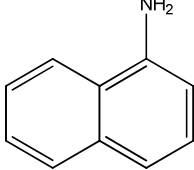
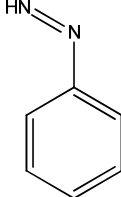
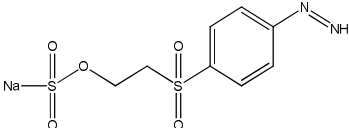


Fig. 2.11 GCMS chromatograms obtained for decolourization of dye RB5 with the MnO₂ based catalysts observed after 60 min.

It is obvious as shown in Fig. 2.11 that the intensity of the spectra peaks enhances consistently from MnO₂ rGO/MnO₂, to US/rGO/MnO₂, representing higher degradation rate of RB5 by sono-Fenton treatment. Mainly, the determined peaks at *m/z* ratio value 300, 198, 143, 106 and 78 coincide very well with the organic intermediates as shown in Table 2.4.

Table 2.4 Degradation products of RB5 after the catalytic reaction as determined using GC-MS spectrum.

Intermediates formed during degradation of RB-5	Name of the intermediate
	(4-(ethylsulfonyl)phenyl)diazene
	naphthalene
	benzene
	sodium 5-aminonaphthalene-1,6-disulfinate
	sodium 5-aminonaphthalene-1-sulfinate
	naphthalen-1-amine
	phenyldiazene
	sodium 2-((4-diazenylphenyl)sulfonyl)ethyl sulfite

The different organic molecules after the decomposition of RB5 may have been formed through the following steps, (i) –N N– double bond split (ii) break of various C–C and N-C bonds of the chromophore compound, loss of sodium ions plus the gain of hydrogen's (iii) cleavage of the S-C bond between the sulfonate groups and aromatic ring by the hydroxyl radicals attack and (iv) cleavage of the benzene ring (Sharma and Roy 2015).

2.4.1.2.1 Influence of functional parameters

In order to detect the influence of other parameters on the degradation of dye, experiments were conducted at the constant pH = 5 for a reaction period of 60 min, using sono-Fenton catalysis, with different amount of rGO/MnO₂, H₂O₂, and dye,

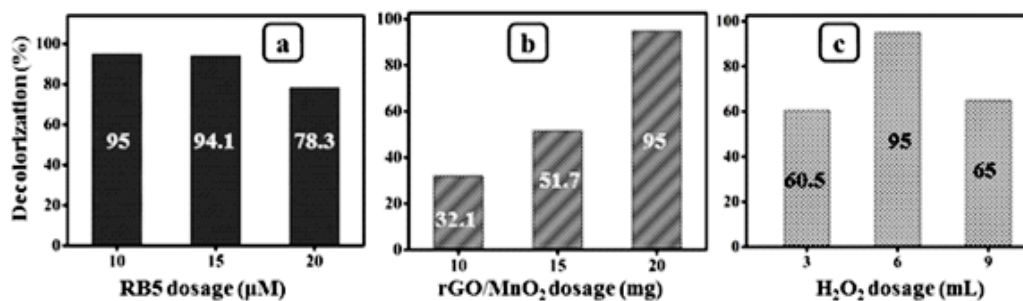


Fig. 2.12 Effect of variation in the dosage of (a) dye, (b) catalyst, and (c) H₂O₂ on the decolorization of RB5 dye in the ultrasonication combined Fenton reaction at pH of 5 for the period of 60 min.

(a) Influence of Dye (RB5) quantity

The quantity of RB5 is one of the principal factors in a sono-Fenton reaction. The degradation of the RB5 was detected by altering the initial quantity range from 10 to 20 μM. The results are given in Fig.2.12 (a). As the quantity of the RB5 increases, the chemical species attached sturdily to catalyst surface and then decreases the effectiveness of the catalytic reaction due to the decay in OH₂[•] and OH[•] quantities, leading to lower degradation rate and saturation. Also, the presence of large quantity

of adsorbed dye reduces the probability of interaction with the OH radicals, resulting in an inhibitive effect on the RB5 decomposition (Tayeb and Hussein 2015).

(b) Influence of catalyst quantity

The quantity of catalyst in the sono-Fenton reaction is another parameter taken into consideration. Usually, it is observed that the dye color removal enhances with increasing quantity of catalyst, while keeping other parameters set. As the catalyst quantity enhances, more amount of dye is adsorbed on the surface of the catalyst. This increases the probability of interaction amid RB5 molecules and oxidizing groups, thus causing an improvement in decolorization percentage (Akpan and Hameed 2009). Fig.2.12 (b) displays the Influence of catalyst amount on the dye degradation percentage.

(c) Influence of H₂O₂ concentration

The sono-Fenton decolorization of RB5 is also affected by the dosage of H₂O₂ in the aqueous solution. To detect the optimal amount of the H₂O₂, 3-9 mL was taken in the 100 mL RB5 solution. The decolorization increased noticeably with increasing the initial H₂O₂ dosage from 3 to 6 mL as depicted in Fig. 2.12 (c). It is ascribed to increase in the adsorption and interfacial reactions, which in turn increases the number of OH radicals. As the dosage of H₂O₂ is further enhanced from 6 to 9 mM, the solution becomes thick and stops the Fenton reaction, and hence the decolorization of the RB5 reduced (Kim et al. 2015). Nevertheless, H₂O₂ itself acts as an effective OH[•] scavenger at dosages that are specific for the affluent, accordance with the empirical Eq. (43)



Thus, the presence of surplus H₂O₂ can reduce the treatment effectiveness of Fenton reaction.

The recycling ability of the prepared catalyst rGO/MnO₂ and MnO₂NWs was also estimated using the decolorization of the RB5 as depicted in Fig.2.13. In order to verify the reusability of catalyst, it was washed with D.I water and dried in air at 60 °C for 4 h, and reused in the number of cycles from the 1st to 5th cycle. The decolorization efficiency decreases slightly from 84.5% to 81.2% for GO/MnO₂ NWs, while, the decolorization efficiency largely decreased from 63.1% to 55.5% in the case of bare MnO₂ NWs, because some quantity of catalyst is lost during filtration and washing. The wrapping of MnO₂ NWs with rGO sheets decreases the contact of NWs during washing, as well as they're dissoluble in the water. It is ascribed to the lower mass loss of the rGO/MnO₂ NWs compared to the bare MnO₂NWs. Hence, rGO/MnO₂ NWs has cyclic stability and can be reused without a considerable decrease in catalytic performance for decolorization of the RB5 in water.

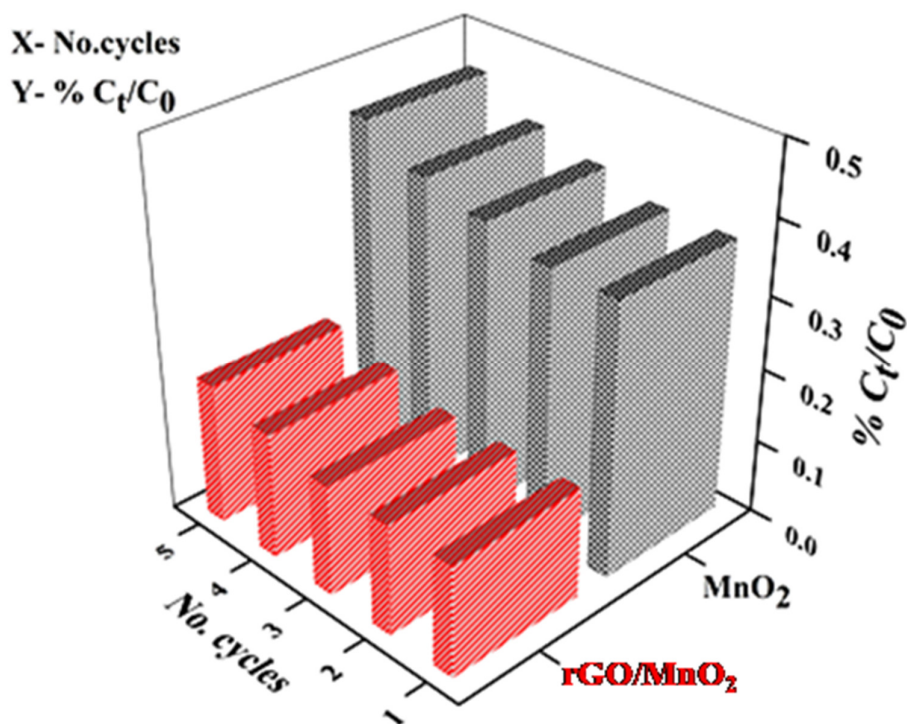


Fig. 2.13 Recycling (5 cycles) performance of the α -MnO₂ NWs and rGO/MnO₂ NWs for the degradation of the RB5 after 60 min.

2.4.2 Super capacitors

2.4.2.1 Electrode fabrication

In a typical process, certain amount of nanopowder of active material and acetylene block (conducting agent) were taken in to the grinder, which was followed by the adding of polyvinylidene difluoride, which acted as binder. After being crushed it for some time, a few drops of N-methyl-2-pyrrolidone was injected slowly in it to prepare a fine slurry and then rubbed on freshen Titanium sheet over an area of $1 \times 1 \text{ cm}^2$. The resultant product dried in a vacuum oven for 12-15 hours at $55 \text{ }^\circ\text{C}$. The average weight of the active material was found to be around 0.14 mg.

2.4.2.2 Electrochemical characterization

To study the electrochemical properties of MnO_2 and its nanocomposites, a conventional electrochemical cell was made with active material coated titanium foil as a working electrode, platinum counter electrode, Ag/AgCl as a reference electrode and 1M Na_2SO_4 solution were used as an electrolyte.

Fig. 2.14 depicts the CV curves of MnO_2 and its nanocomposites in 1 M Na_2SO_4 electrolyte at a scan rate of 20 mV s^{-1} . It can be seen that the geometrical area of CV curve is in the order of $\text{Sn@rGO-MnO}_2 > \text{rGO@MnO}_2 > \text{MnO}_2$. The corresponding redox reactions occur at the interface of electrode/electrolyte may be mentioned as.



The prepared working electrodes are used for determination of specific capacitance of super capacitors from the galvanic discharging and CV plots using Eqs. (12-13). In all the products, the obtained specific capacitance is responsible partly from electrical double layer capacitance of graphene and mainly from the pseudo-capacitance of MnO_2 . As illustrated in Fig. 2.15 the specific capacitance of the active materials are in the order of $\text{Sn@rGO-MnO}_2 > \text{rGO@MnO}_2 > \text{MnO}_2$ at the scanning rate of 20 mV/s . The specific capacitance of nanocomposites is more compared to the pure MnO_2 which is due to the synergistic effect between MnO_2 and graphene. Though the

graphene content is equal in the nanocomposites, the positive effect of Sn@rGO@MnO₂ is contributed from Sn. It is also initiated that the specific capacitance reduces with raise in scan rate as depicted in Figure 2.15.

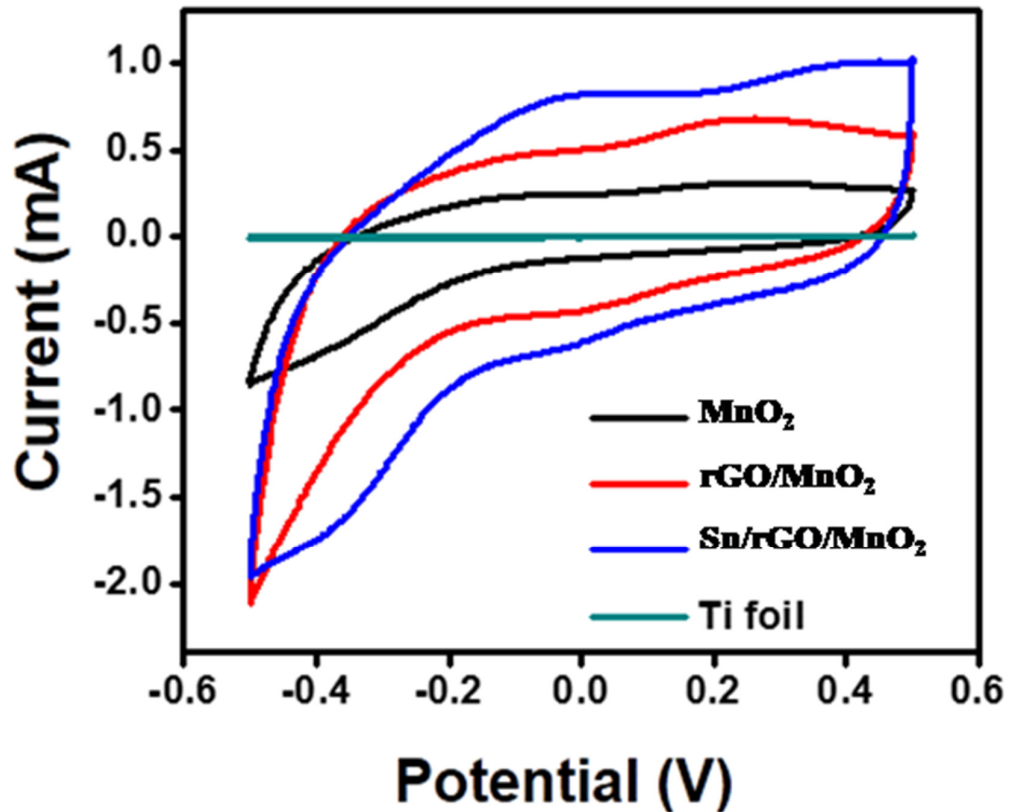


Fig. 2.14 CV curves for various working electrodes in aqueous 1M Na₂SO₄ at a scan rate of 20 mV/s.

The specific capacitance of electrodes is also explained in terms of their structural parameters such as the dislocation density and crystallite size. As illustrated in Table. 2.2 the crystallite size in the nanocomposites is less compared to pristine MnO₂ NWs. The smaller crystallite size is ascribed to reduction in ion diffusion path length. Hence, the reduction in the ion diffusion path length favors faster a change transfer between electrolyte and electrode, leading to more specific capacity. The specific capacitance of present electrodes were compared well with the reported values as illustrated in Table. 2.5

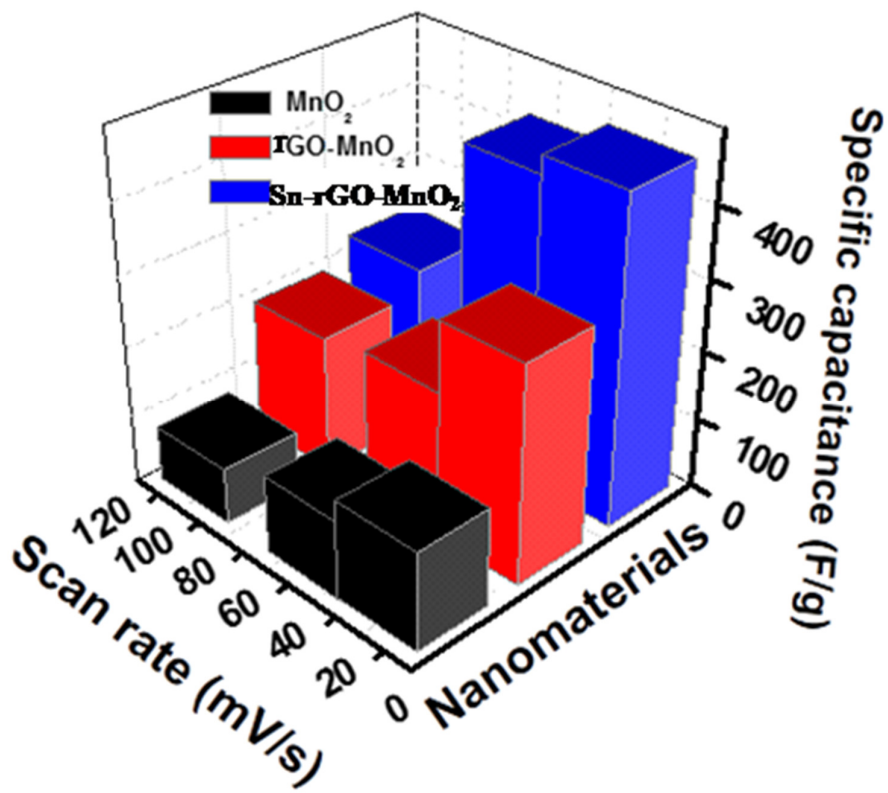


Fig. 2.15 Specific capacitance versus scan rates curves for various working electrodes in aqueous 1M Na₂SO₄ at a scan rate of 20 mV/s.

Table 2.5 Specific capacitance of MnO₂based nanomaterial compared with reported values.

Electrode	Electrolyte	Specific Capacitance (F/g)	Reference
Sn@rGO-MnO ₂	1 M Na ₂ SO ₄	460.9	Present work
rGO-MnO ₂	1 M Na ₂ SO ₄	309.7	Present work
MnO ₂	1 M Na ₂ SO ₄	144.1	Present work
sponge@rGO@MnO ₂	1 M Na ₂ SO ₄	450	(Ge et al. 2013)
RGO/MnO ₂ NS	1 M Na ₂ SO ₄	446	(Zhou et al. 2015)
MnO ₂ /CNT- textile	0.5 M Na ₂ SO ₄	410	(Hu et al. 2011)
C@MnO ₂	1 M Na ₂ SO ₄	321	(Mu et al. 2015)
G/MnO ₂	1 M Na ₂ SO ₄	319	(Hao et al. 2015)
MnO ₂ -N-rGO	1 M Na ₂ SO ₄	275.2	(Mei and Zhang 2015)
MnO ₂ NT array	0.5 M Na ₂ SO ₄	231	(Grote et al. 2014)
α-MnO ₂	1 M Na ₂ SO ₄	180	(Yin et al. 2014)
α-MnO ₂ @ δ-MnO ₂	6 M KOH	153.8	(Ma et al. 2016b)
MnO ₂ /C	0.25 M KCl	112	(Kim et al. 2015)

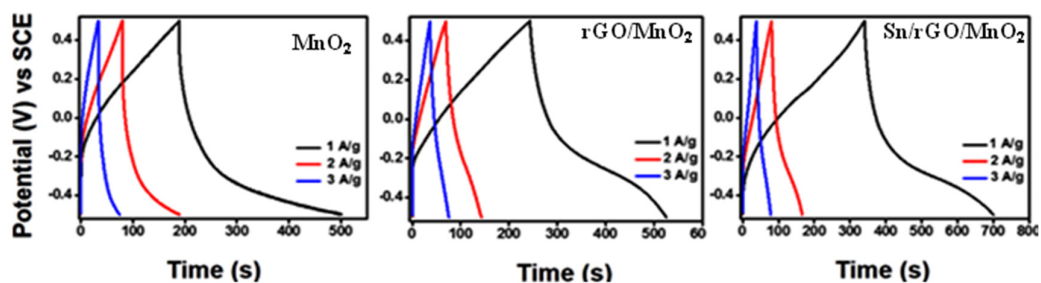


Fig. 2.16 Galvanostatic curves for various working electrodes in aqueous 1M Na₂SO₄ at a scan rate of 20 mV/s.

As seen in Fig. 2.16, Sn@GO-MnO₂ nanocomposite has the longest discharge-charge time compared to the GO-MnO₂ and MnO₂, which means it has the more specific capacitance which was around 622.4 F/g at a current density of 1 A/g.

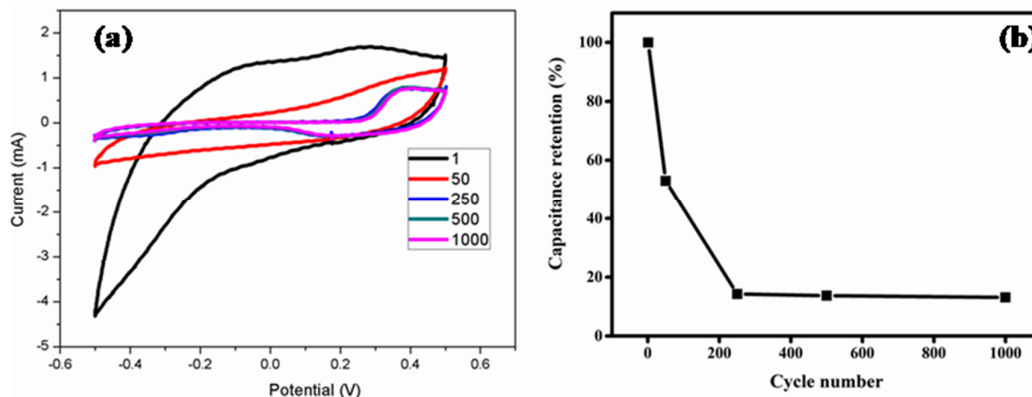


Figure 2.16A shows the long term stability of the MnO₂ NWs as working electrode in the electrolyte of 1M Na₂SO₄ at scan rate of 20 mV/s, (a) cyclic voltammograms and (b) capacitance retention of electrode at the various cyclic number.

In above figure 2.16A, the multiple cycle stability of MnO₂ NWs was evaluated by cyclic voltammetry up to 1000 cycles, where the applied potential range is from -0.5 V to 0.5 V and scan rate at 20 mV/s. The cyclic data indicates that the capacity is reduced to almost 1/3 of initial value after 50 cycles, to 14% after 250 cycles and then remained almost constant for 1000 cycles. The degradation in the performance may be linked to the structural changes in the sample. Na₂SO₄

In order to gain further understanding of the differences in the electrochemical performances of working electrodes, EIS testing was carried in Fig. 2.17 in a frequency range from 100 kHz to 1 kHz at the applied voltage of 10 mV vs. Ag/AgCl reference electrode. The obtained EIS data of all the samples was composed of semicircles and fitted with an equivalent circuit as depicted in the inset of Fig. 2.17. In

the EIS spectra, the intercept of high frequency arc on real axis is related to solution resistance (R_s) and slope of the inclined line at low frequency area indicates capacitive region [127]. Experimental outcomes display that R_s is the surface resistance of active materials, and it is less for Sn-rGO-MnO₂ than rGO-MnO₂ and MnO₂, which suggests its better charge conductivity due to incorporation of Sn atoms in the composite (Bindu et al. 2016). It may be observed that all the samples exhibits an inclined line above 45°, which represents the pseudo capacitive behaviour of the electrodes (Shanmugavani and Selvan 2014).

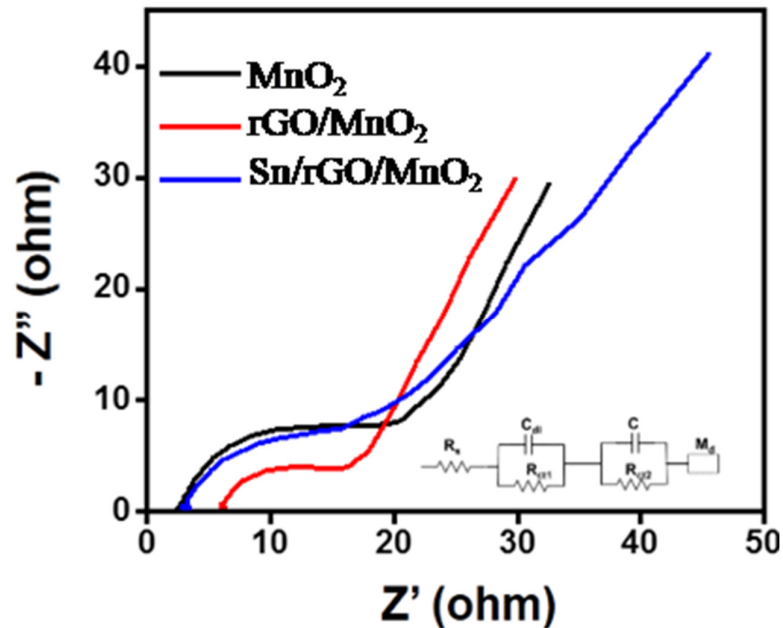


Fig. 2.17 Nyquist plots of active materials prepared using Sn@rGO-MnO₂, rGO-MnO₂ and MnO₂ in 1 M Na₂SO₄.

2.5 Conclusions

Pristine MnO₂ NWs and its nanohybrids using Sn and rGO doping were prepared by hydrothermal process. The band gap of hydrothermally grown MnO₂ NWs decreases and the surface area enhances with the enhancement in amount of KMnO₄. Raman, SEM study shows rGO nanosheets wrapped MnO₂ NWs and XRD declares smaller crystallite size of rGO/MnO₂ NWs compared to pristine MnO₂ NWs. The degradation

rate of RB5 was found to increase with increasing concentration of KMnO_4 . rGO/MnO_2 NWs show higher catalytic activity than pure MnO_2 NWs towards decomposition RB5 colorant. Hence, rGO/MnO_2 NWs show superior catalytic activity on the degradation of the RB5 colorant with H_2O_2 based on the sonolysis combined-Fenton catalysis. Also, rGO/MnO_2 NWs exhibit better reusability due to the wrapping of NWs with rGO. From the galvanic discharge and CV study, the specific capacitance of Sn@rGO-MnO_2 electrode was found to be more than that of rGO-MnO_2 and MnO_2 electrodes, which is attributed to the synergistic effect of the system of $\text{MnO}_2/\text{graphene}$, and electrical conductivity of the Sn particles. The enhanced performance of MnO_2 and its nanocomposites towards their catalytic activity and electrochemical performance might be related to its optical and structural properties.

CHAPTER 3

GROWTH, CHARACTERIZATION AND CATALYTIC ACTIVITY OF NiO AND CuO NANOPARTICLES

3.1. Introduction

In this section, the preparation and characterization of NiO and CuO nanoparticles, and their photocatalytic/adsorption activity towards various dyes such as methylene blue (MB), acid yellow 23 (AY-23) and reactive black 5 (RB-5) in the presence/absence of visible light are studied. NiO nanoparticles are prepared using thermal decomposition technique. The results on the effect of annealing temperature on the adsorption and photocatalytic properties of NiO nanoparticles towards RB-5 removal and MB degradation, is reported. The CuO nanoparticles are prepared by modified chemical precipitation technique. Finally, this chapter ends with the kinetics study in order to understand the rate of degradation of respective dyes.

3.2 Experimental procedure

3.2.1 Preparation of NiO NPs

0.1M of nickel nitrate hexahydrate ($\text{Ni}(\text{NO}_3)_2 \cdot 6\text{H}_2\text{O}$) and 0.2M of sodium hydroxide (NaOH) were dissolved in 100 mL of deionized water. The obtained solution was magnetically stirred at room temperature for about 1 h. The resultant green colored solution was washed with ethanol and deionized water several times to remove formed contaminants during the reaction and dried at 55 °C for 12 h. Afterwards, dried precipitates were calcined at 200 °C, 300 °C, and 400 °C for 2 h respectively.

3.2.2 Synthesis of CuO NPs

0.5 g of sodium dodecyl sulfate and 0.4 M potassium hydroxide were added to 100 mL of copper (II) nitrate trihydrate (0.2 M) solution under constant stirring. After 30 min, 50 mL of ammonia (12.5 wt %, ~7.0 M) was injected slowly in it and continued to stir for 15 h. The resultant mixture was centrifuged several times with ethanol and double distilled water to remove its impurities and dried at 80 °C for 12 h in vacuum. Finally, the dried precipitates were annealed at 400 °C for 4 h.

3.3 Results and discussions

3.3.1 Structural and optical properties of NiO NPs

In order to evaluate the crystal properties of annealed NiO NPs, XRD was registered as shown in Fig. 3.1. All diffraction peaks of NiO NPs were well indexed in a cubical phase according to the standard spectrum (JCPDS card No. 01-175-0269). From XRD, the variation in peak widening is associated with crystallite size, as given in Table 3.1. We calculated the average size of the NPs using Eq. (5). As shown in Table 3.1, the crystallite size enhances with the rise in annealing temperature. By increasing the annealing temperature, the XRD peak broadening (FWHM) reduces and hence the crystalline volume increases, suggesting the size of NiO NPs becomes larger.

Table 3.1 The optical and structural parameters of NiO NPs (Where d - mean size of the crystallite, D - average particle diameter and SA - surface area).

Temperature (°C)	d (nm)	D (nm)	SA (nm ²)	Band gap (eV)
200	2.0	2.5	79.1	3.7
300	3.1	4.2	224.7	3.2
400	5.4	7.6	742.7	2.7

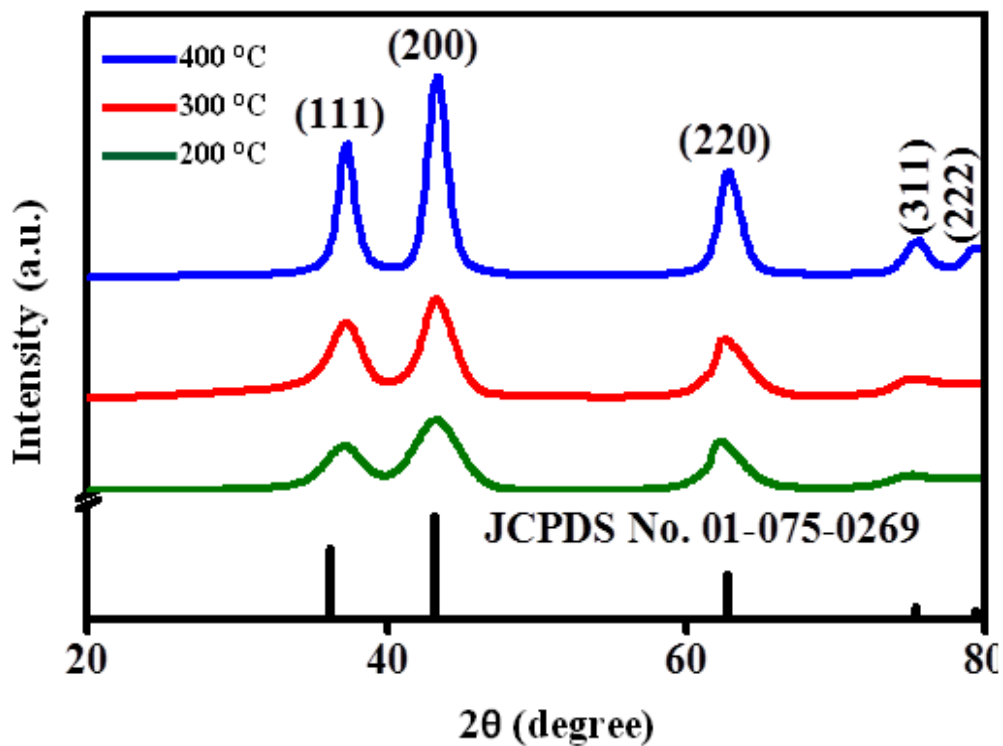


Fig. 3.1 XRD of the NiO NPs at different annealing temperatures (200-400 °C).

UV-Vis absorption spectra NiO NPs were registered as shown in Fig. 3.2 (a). It may be noticed that the absorption edge was red shifted with rising annealing temperature, which is ascribed to the better quantum confinement effect. It is necessary to detect the energy band gap of NiO NPs by Tauc's Eq. (7) as depicted in Fig. 3.2 (b). As shown in Table 3.1, E_g decreases with the rise in the annealing temperature due to increased crystallite size (Al-Sehemi et al. 2014).

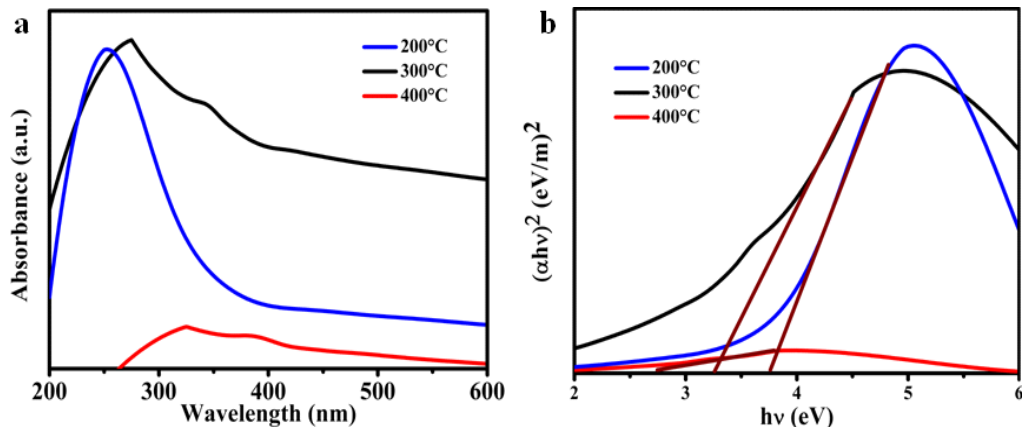


Fig. 3.2 (a) UV–visible absorption spectra and (b) band gap energy (E_g) of the NiO NPs at different annealing temperatures.

In order to look into the morphology of NiO NPs, SEM images are displayed in Fig. 3.3. We can conclude that the measured size and surface area of NiO NPs based on image J software were found to mainly depend on the annealing temperature. At lower (200°C) annealing temperature, the particle growth is not thermodynamically favored, with only the least number of atoms can diffuse into the cluster but remaining atoms soluble, which results in a smaller particle size and lower surface area as given in Table 3.1. However, at an elevated (200 °C) annealing temperature, a great number of atoms acquire activation energy and diffuse over the nucleation barrier to creating clusters, resulting in particles of larger diameter and higher surface area. The morphology of the NiO NPs has been investigated using high-resolution TEM techniques. Fig. 3.4 is the respective TEM images of the NPs obtained from A, which indicate the particle size around 5–50 nm. It reveals that there is large homogeneity at the sample surface, with particle agglomeration and the particles are nearly spherical. The presence of aggregates shows that the mild conditions of thermal cluster degradation favour the coalescence of the NiO NPs and that the growth of some particles by coalescence can reveal the presence of the spherical shapes observed in the TEM analysis. The lattice fringes as shown by the arrows in B indicate clear crystalline structure that is further supported by SAED pattern by the formation of clear rings. The choice of nickel precursor and method is the main step in the synthesis of NiO NPs.

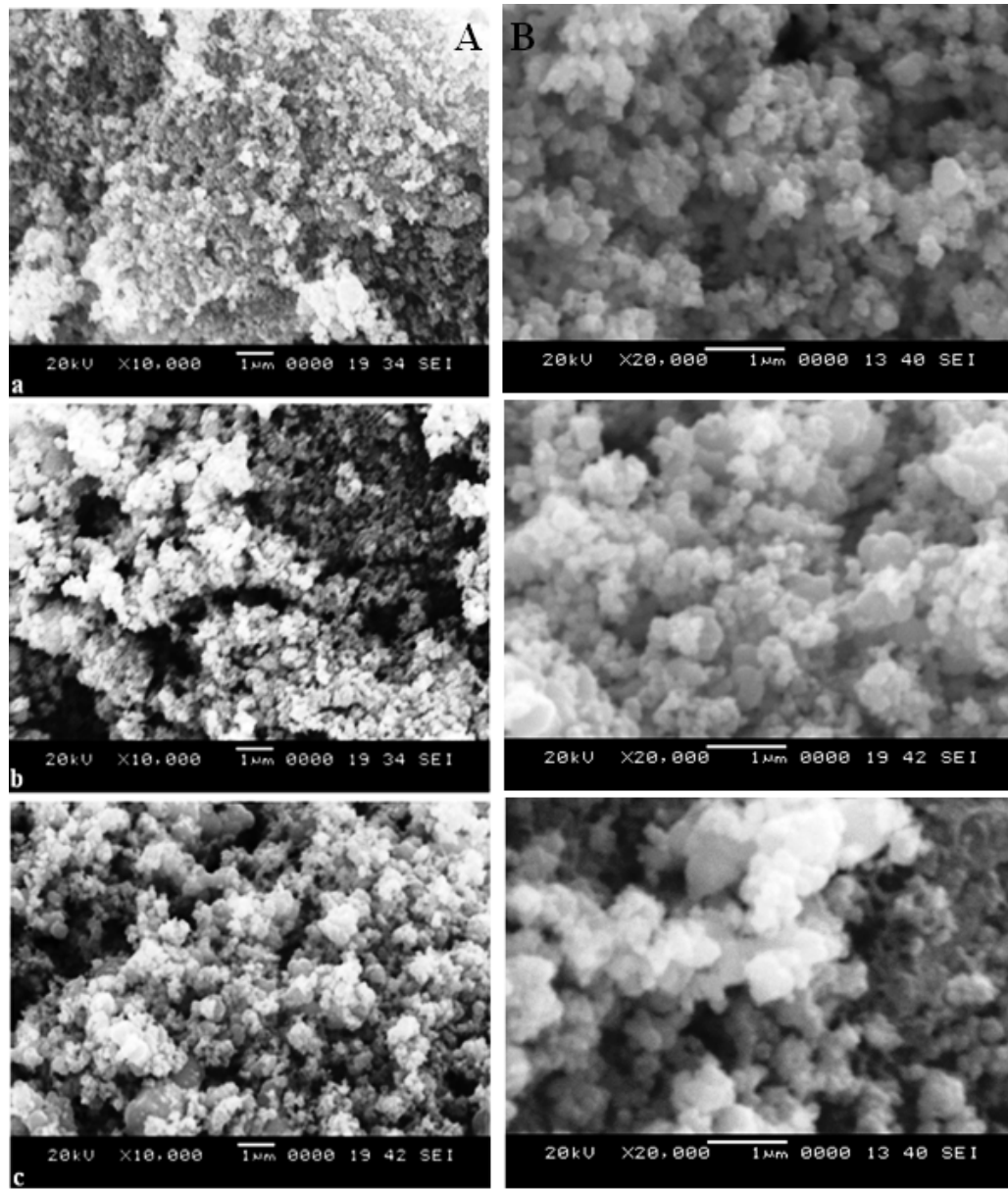


Fig. 3.3 (a) Low-magnification and (b) High magnification of SEM image of the NiO NPs at the temperature of (a) 200 °C, (b) 300 °C and (c) 400 °C.

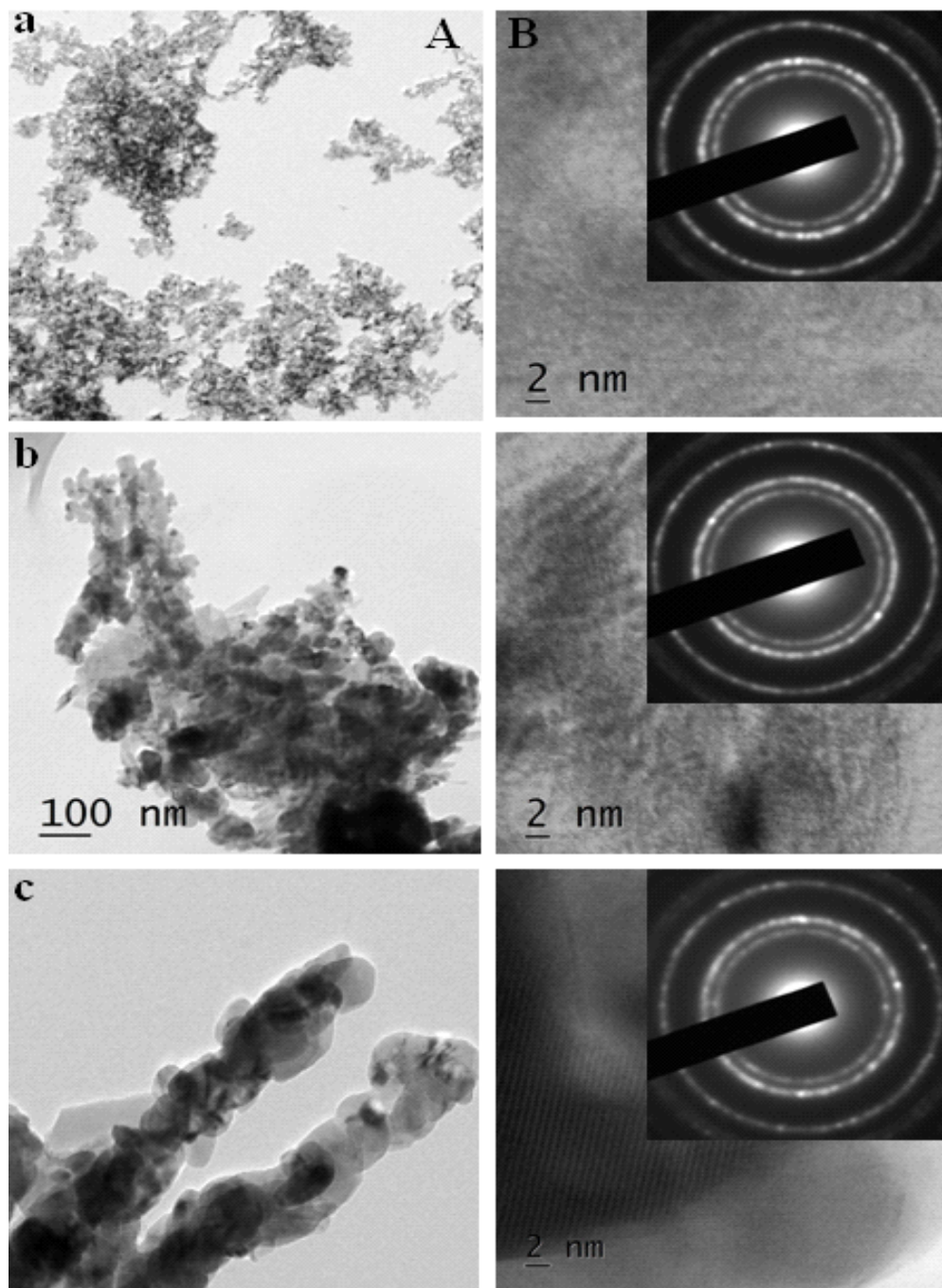


Fig. 3.4 (a–c) TEM images of NPs generated at different annealing temperature of (A) low magnification and (B) high magnification with inset showing SAED patterns of the corresponding NPs.

3.3.2 Structural and optical properties of CuO NPs

To study the structural properties of CuO NPs, XRD was registered as shown in Fig. 3.5 (a). All the diffraction peaks were indexed to the monoclinic phase of CuO with lattice constants of $a = 4.6500 \text{ \AA}$, $b = 3.410 \text{ \AA}$, $c = 5.110 \text{ \AA}$ and $\alpha = \gamma = 90^\circ$, $\beta = 99^\circ$ according to the standard spectrum (JCPDS card No. 00-002-1041) (Maddinedi and Mandal 2014). SEM micrographs were used to evaluate the surface morphology of the CuO NPs. As can be seen in Fig. 3.5 (b) that the CuO NPs consisted spherical shape with a smooth surface and connected homogeneous rod like architecture. In order to detect the optical properties of the CuO NPs, UV-vis spectra are depicted in Fig. 3.5 (c). The figure depicted maximum absorption peak at about 437.6 nm was assigned to the electronic transition from n to π^* molecular orbitals of the ligand, which was a good evidence for the presence of CuO NPs (Bouazizi et al. 2015). This optical spectra can be used to estimate the energy gap of CuO NPs through the Tauc's Eq. (7). As shown in Fig. 3.5 (d), the extrapolation of the linear portion of the curve to energy axis referred to the energy gap of CuO NPs, which was estimated to be 1.76 eV.

To reveal nanomorphology of the synthesized products, typical HRTEM images have been recorded, as shown in Fig. 3.6. Fig. 3.6 (a) shows the TEM bright-field images of CuO nanoparticles calcined at 400°C. It can be clearly observed that the synthesized product consists of nearly spherical-shaped particles with a size around 5-10 nm. The lattice fringes can be clearly seen from the HRTEM image (Fig. 3.6 (b)), in which interplanar distance is determined to be about 0.25 nm, which is consistent with the d spacing of (002) of CuO. From HRTEM image the unidirectional fringe patterns are clearly observed, which indicates single crystalline nature of CuO nanoparticle. Selected area electron diffraction pattern (SAED) originated from the CuO nanoparticle is shown in Fig. 3.6 (c).

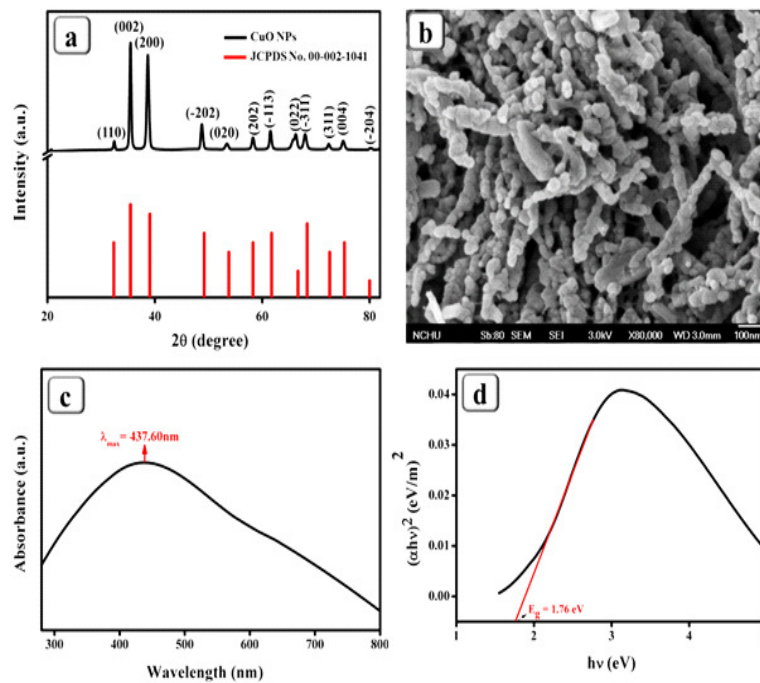


Fig. 3.5 (a) XRD pattern, (b) SEM image, (c) UV-Visible spectrum and (d) Tauc plot of the CuO NPs.

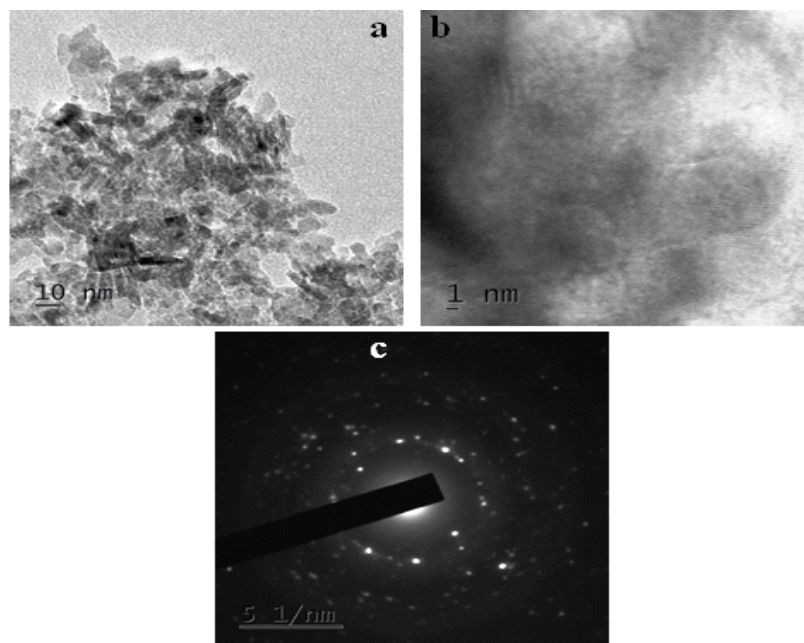


Fig. 3.6 (a) Low-magnification and (b) High magnification of HRTEM image of CuO NPs calcined at 400°C and (c) SAED patterns of the corresponding NPs.

3.3.3 Adsorption and photo-catalysis experiments

Here, MB, RB-5, and AY-23 dyes were used as model pollutants. Initially, adsorption study was performed in 250 ml borosil beaker at room temperature. For the reaction, 30 mg/20 mg of NiO/CuO powder added separately to the 100 mL of 30 μ M dye solutions and magnetically stirred. After attaining adsorption equilibrium, 5 mL of aliquots were taken at regular time intervals and filtered with PVDF (0.45 μ m) filters to separate the adsorbent particles. The concentration of the residual dye was measured using Eq. (12).

The photo-catalytic treatment was carried out in a photo-catalytic chamber assembled with three tungsten halogen lamps (Osram, 150 W/24 V), which emit the radiations in the visible region of electromagnetic spectrum. The prepared aqueous solution was irradiated in presence of visible light at different reaction time ranging from 0 to 5 h. Prior to irradiation, the above mixture was magnetically stirred in the dark for 30 min, in order to get desorption/adsorption equilibrium.

As can be seen in Fig.3.7, the UV-vis spectra studied during the adsorption of MB exhibits the peaks at 292 nm and 664 nm, and RB5 exhibits the peaks at 313.6 nm and 601 nm respectively, due to structural units and various groups in the dye molecules. The peaks of both dyes in visible region were attributed to the absorption of the $n \rightarrow \pi^*$ transition related to the $-N=N-$ group in the dye molecule, while the peaks in UV region were ascribed to the absorption of the $\pi \rightarrow \pi^*$ transition related with the naphthalene ring and benzene ring. The lower rate in the UV region is attributed to the partial removal of organic molecules due to the high energy band amid aromatic rings (Sun et al. 2007).

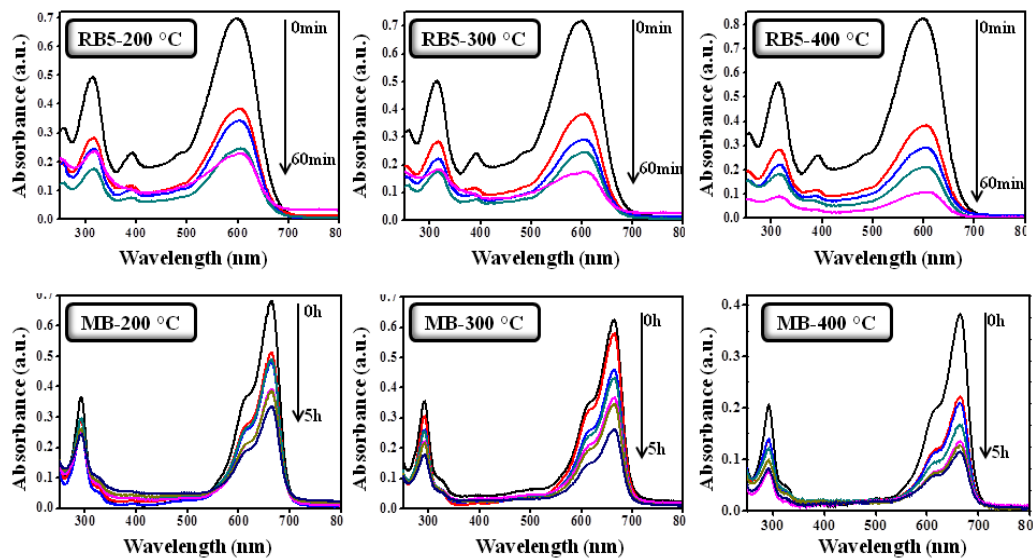


Fig. 3.7 Adsorption and photocatalytic performance of NiO NPs prepared at various temperatures towards RB-5 and MB dyes.

Fig. 3.8 (a) illustrates the optical absorption spectra of dye (MB, RB-5 and AY-23) solution over CuO NPs. By increasing the reaction time, the dye absorbance decreases because of the more dye molecules being adsorbed on the surface of CuO NPs. Therefore, less number of photons reach the catalyst surface and therefore less radical species, thus resulting in less absorbance of dye.

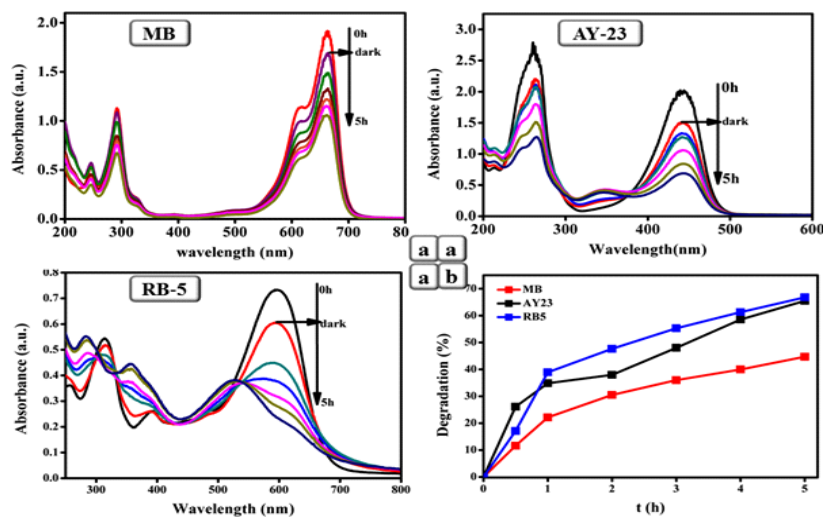


Fig. 3. 8 (a) Absorption spectral changes and (b) photo-catalytic degradation of various dyes by CuO NPs under visible light.

Fig. 3.8 (b) displays the graph of degradation efficiency against irradiation time for AY-23, RB-5, and MB. At the time of 5h, the dye degradation was estimated ~ 43.5, 66.3 and 67.8 % for MB, AY-23, and RB-5, respectively. According to these results, the photo-catalytic degradation of RB5 was found to be more than that of AY-23 and MB, because of its molecular structure which is more favorable for oxidation. The improved degradation percentage in RB-5 can be interpreted in terms of Molecular weight of dye. Molecular weight defines a number of particles in the dye. More the molecular weight, more particles is exposed towards the photo-catalyst and thus creates a more adsorbed layer over the catalyst surface. According to the second law of photochemistry, each atom or molecule receive one photon; therefore RB-5 receives the excess number of photons compared to AY-23 and MB, intern increase the rate of photo catalytic reaction in the system of RB-5-CuO, therefore, enhancing the RB-5 degradation efficiency (Okabe 1978).

The photo-degradation and adsorption efficiency of NiO NPs towards dye MB and RB5 are depicted in the Fig.3.9. During initial 30 min, RB - 5 dye removal was fast, in the range from 0 % to 72.4 %. Afterwards it was found to be slow due to the adsorption limit, estimated in the range from 64.5 % to 87.2%. The removal of dye is mainly affected by the annealing temperature of the NiO NPs. The dye RB-5 removal efficiency was approximated to be in the range from 65 % to 87.2 % when NiO NPs are annealed with a temperature range from 200 °C to 400 °C, at the reaction time of 60 min. Table 3.2 shows the comparison of removal of RB-5 dye under various laboratory conditions.

Table 3.2 Comparison of RB-5 Removal of NiO NPs with reported literature values.

Catalyst	Amount	Dye concentration	Time	Source	Degradation (%)	Reference
N-doped TiO ₂	0.24 g/200 ml	10 ppm	3 h	Visible light	52.4	(Kaur et al. 2015)
Micrococcus luteus		20 mg/L	3 days	Bio-degradation	66	(Saratale et al. 2010)
TiO ₂	-----	10 mg/L	10 h	UV light	80	(Puentes-Cárdenas et al. 2012)
TiO ₂	-----	10 mg/L	300 min	UV light	70	(Kodom et al. 2013)
CuO	250 mg/L	10 ppm	60 min	Ultrasound	50	(Saravanan and Sivasankar 2016)
NiO (400 °C)	30 mg	3×10 ⁻⁵ M	60 min	No light	87.2	Present work
NiO (300 °C)	30 mg	3×10 ⁻⁵ M	60 min	No light	70.2	Present work
NiO (200 °C)	30 mg	3×10 ⁻⁵ M	60 min	No light	65	Present work

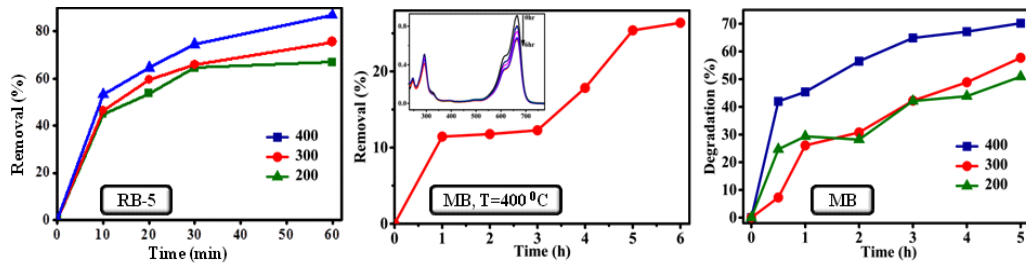


Fig. 3.9 Effect of time on removal/degradation of dye over NiO NPs.

In the case of MB adsorption over NiO, the removal of dye is fast in the beginning due to the availability of vacant surface sites and gets nearly saturated, when the reaction time was increased from 3h to 5h. On the contrary, the degradation of the MB was about 50.8 %, 57.6 % and 70.2 % for the catalyst at an annealing temperature of 200 °C, 300 °C, and 400 °C respectively, after irradiation under visible light. Hence, it is noticed that the degradation rate of MB increases with the rise in annealing temperature of the catalyst. A rise in the annealing temperature of NiO NPs results in the reduction of the band gap of NPs as depicted in Fig.3.9. The maximum degradation efficiency of MB in the current work is comparatively better than the literature values, as displayed in Table 3.3.

Table 3.3 Comparison of photocatalytic degradation of MB dye using NiO with reported literature data.

Catalyst	Dye concentration	Amount	Source	Time (h)	Degradation (%)	Reference
α -Bi ₂ O ₃ (Sol-gel method)	2×10 ⁻⁵ M	100 mg	Visible light	6	30	(Jalalah et al. 2015)
α -Bi ₂ O ₃ (Hydrothermal)	2×10 ⁻⁵ M	100 mg	Visible light	6	50	
Hematite (α -Fe ₂ O ₃)(0.5% - spheres)	20 mg/L	2.5 g/L	Sun light	8.3	51	(Tan et al. 2013)
Hematite (α -Fe ₂ O ₃)(1% - ellipsoids)	20 mg/L	2.5 g/L	Sun light	8.3	33	
CuO (CTAB)	3×10 ⁻⁵ M	20 mg	Visible light	6	43	(Rao et al. 2015)
HNbWO ₆	5×10 ⁻⁵ M	50 mg	UV light	6	62.5	(Hu et al. 2015)
poly(TPT)/TiO ₂	1×10 ⁻⁵ M	40 mg	UV light	7	51.5	(Jamal et al. 2014)
Flower like CuO	10 mg/L	20 mg	H ₂ O ₂	8	65	(Yang and He 2011)
ZrO ₂	20mg/L	10 mg	UV	2	33	(Khaksar et al. 2015)
ZnS: CdS (Wt% 50:50)	10mg/L	100 mg/L	Visible light	6	65	(Soltani et al. 2012)
NiO (200 °C)	310 ⁻⁵ M	30 mg	Visible light	5	50.8	Present work
NiO (300 °C)	310 ⁻⁵ M	30 mg	Visible light	5	57.7	Present work
NiO (400 °C)	310 ⁻⁵ M	30 mg	Visible light	5	70.2	Present work

The photocatalytic activity of the catalyst was commonly associated to its E_g . The detected E_g of catalyst is in the range from 2.3 eV to 4.1eV, as displayed in Table 3.1. Considering the large E_g of catalyst, the wavelength of the irradiation for the generation of charge carriers over the NiO- MB system should be less than 400 nm. However, in the present case, the visible light absorption can be interpreted utilizing the oxygen molecules in the catalyst. The temperature creates the intermediate energy levels near the valance band, to induce the absorption in the visible region. This was attributed to the creation of oxygen species, whose π^* and π atomic orbital's lie just above and below the valance band of catalyst (Naldoni et al. 2012). The catalytic/adsorption process is related with degradation/removal efficiency as depicted in schematic Fig.3.10.

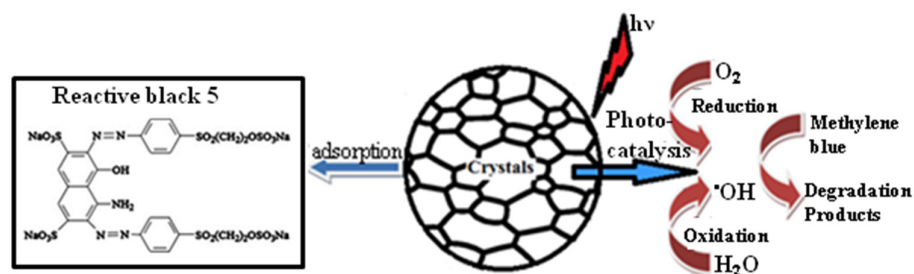


Fig. 3.10 A schematic illustrations for removal of azo dyes from water through combination of adsorption and photocatalytic oxidation of NiO

3.3.4 Reaction Kinetics

In order to study the further details for the adsorption and photocatalysis of NiO NPs, kinetic isotherms were examined:

Here q_e (mg/g) is the quantity of dye adsorbed over NiO at equilibrium and q_t (mg/g) is the quantity of dye adsorbed over NiO at time 't', respectively. K_1 (min^{-1}) and K_2 ($\text{g}/(\text{mg min})$) are the first and second order rate constants, may be determined empirically from the slopes in the plot of t against $\log(q_e - q_t)$ (Eq. 45) and t against t/q_t (Eq. 46), respectively. For photo degradation, rate constant was evaluated from t against $\ln(C_0/C_t)$.

As illustrated in Fig. 3.11, all the graphs are linear with R^2 (correlation coefficient value), which specified the validity of kinetics. The related kinetic values for both processes are presented in Table 3.4. It can be concluded that the adsorption of RB-5 over NiO NPs was found to obey the pseudo-second-order kinetic model because $R_2^2 > R_1^2$, whereas, photo degradation of MB over NiO NPs obey pseudo-first-order kinetic model because $R_1^2 > R_2^2$. The increment in the rate constant of the dye with annealing temperature is attributed to a reduction in the band gap, as well as an increment in the grain size. The evaluated K and R^2 values in the present work are found to be higher than the literature values are summarized in Table 3.5.

The enhanced removal/degradation efficiency of the catalyst can also be correlated to the surface area. As the annealing temperature enhanced, as evident from image J values, geometrical surface area increased, it results in an increase in a number of surface active molecules, which contribute to the adsorption of more number of dye molecules onto the surface of catalyst (Mehta et al. 2011).

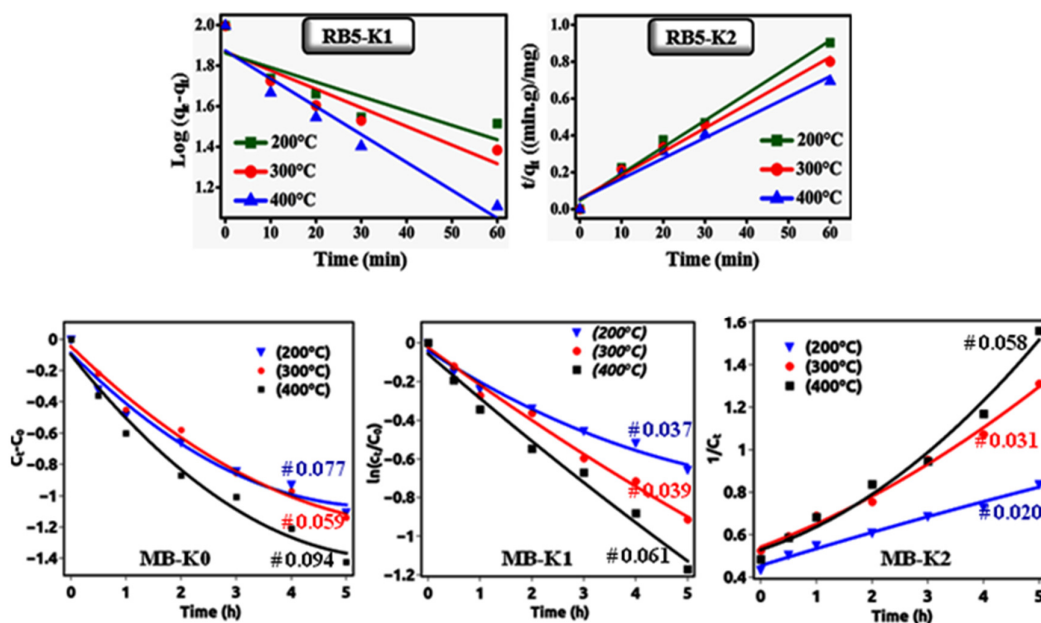


Fig. 3.11 Kinetic graphs for the different dye onto NiO NPs at various temperatures.

The degradation rate of dye (MB, RB-5 and AY-23) over CuO NPs is shown in Fig. 3.12. The related kinetic (k) and correlation coefficient (R^2) values are summarized in Table 3.6. It was noted that the the photo-catalytic degradation of three colorants on the prepared CuO NPs follows the first order kinetic type; $\ln(C_t/C_0) = k_1t$, where k_1 is the first order rate constant. The correlation constant for the fitted line was found to be $R_1^2 = 0.981, 0.992$ and 0.993 for MB, AY-23 and RB-5 respectively. The rate of degradation in the presence of visible irradiation was estimated to be $k_1 = -0.201, -0.174$ and -0.112 h^{-1} respectively. Among three colorants, the decomposition rate of RB-5 is much higher than the MB and AY-23. An increase in the rate constant of RB-5 could be attributed to the increased efficiency rate of absorbance of RB-5 in an aqueous solution that caused by enhanced correspondence to the electron transition in a RB5-CuO system (Abdul Rahman et al. 2014).

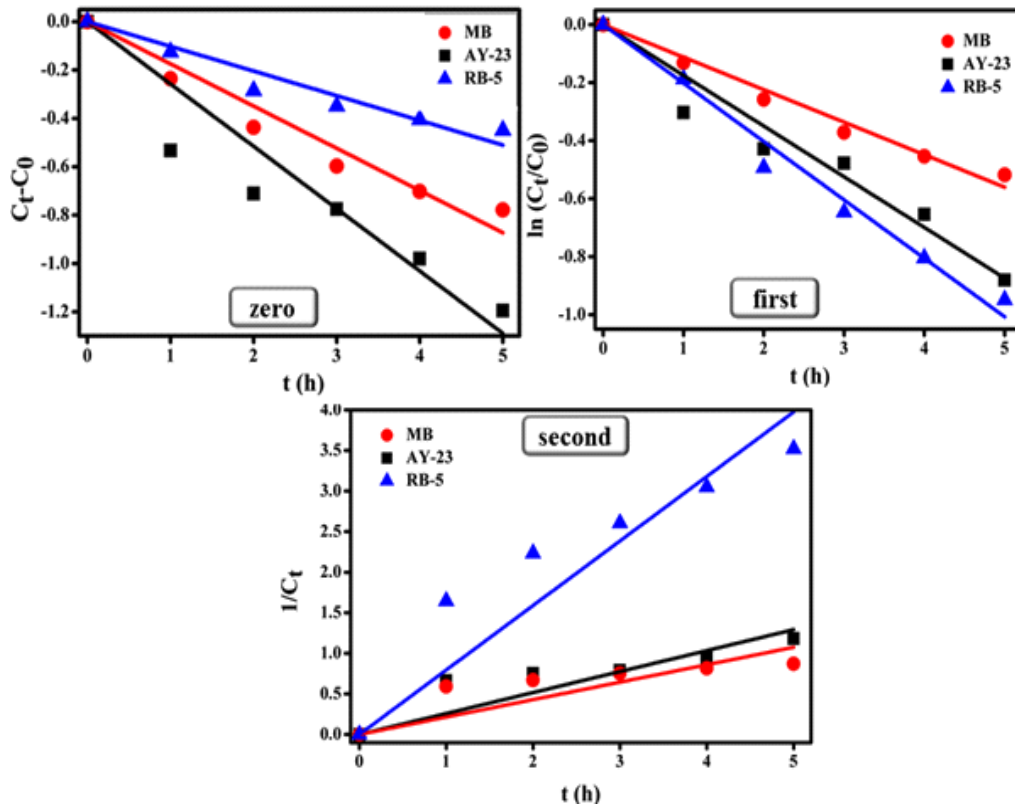


Fig. 3.12 Zero, first, and second, order kinetics for degradation of various dyes after light illumination.

Table 3.4 Kinetic constants for dye (RB5 & MB) removal on NiO NPs.

Temp.	Kinetic constants					correlation coefficients				
	$k_{1, RB5}$	$k_{2, RB5}$	$k_{0, MB}$	$k_{1, MB}$	$k_{2, MB}$	$R_{1, RB5}^2$	$R_{2, RB5}^2$	$R_{0, MB}^2$	$R_{1, MB}^2$	$R_{2, MB}^2$
200	0.0071	0.0111	0.067	0.169	0.154	0.6296	0.9847	0.892	0.937	0.929
300	0.0071	0.0128	0.077	0.710	0.289	0.7875	0.9778	0.961	0.955	0.923
400	0.0137	0.0144	0.079	2.085	0.824	0.9085	0.9708	0.931	0.985	0.890

Table 3.5 Comparison of rate constant (k) and correlation coefficient (R^2) values, with reported values in the literature for the removal of dyes.

Catalyst	Dye	k	R^2	Reference
10-ST/BB	Reactive black 5	0.03003	0.94444	(Kanagaraj and Thiripuranthagan 2017)
CeO ₂ /ZnTi-LDH composite	MO	0.0479	0.9615	(Xia et al. 2014)
CeO ₂ /ZnTi-LDH composite	MB	0.0429	0.9664	
Ir-Sn-Sb oxide	Acid Yellow 36	0.146	0.981	(Aguilar et al. 2017)
α -Fe ₂ O ₃ @GO	MB	0.0190	0.943	(Liu et al. 2017)
CO ₃ O ₄	Methylene blue	0.408	95.4	(George and Anandhan 2015)
TiO ₂	MB	0.0023	0.942	(Mukhlsh et al. 2013)
AAc/PVP/ZnO	MB	0.0056	0.961	(Ali et al. 2016)
ZnO	RB5	0.0090	0.9152	(Laohaprapanon et al. 2015 p. 5)
ZnS	RB5	0.3477	0.9382	(Goharshadi et al. 2013)
NiO	RB5	0.0144	0.9847	Present work
NiO	MB	2.084	0.985	Present work

Table 3.6 Kinetic parameters for photo catalytic degradation of MB, AY-23, and RB-5 on CuO NPs.

Dye	Zero order		First order		Second order	
	R_0^2	k_0	R_1^2	k_1	R_2^2	k_2
MB	0.960	-0.175	0.981	-0.201	0.890	0.215
AY23	0.973	-0.257	0.992	-0.174	0.926	0.258
RB5	0.981	-0.102	0.993	-0.112	0.953	0.794

3.4 Conclusions

The present study concludes that the prepared NiO and CuO NPs were found to be efficient catalysts for the quantitative removal of RB-5, MB& AY-23 from the aqueous solutions. Evidently, 87.2 % of the RB5 dye was successfully removed at the temperature of 400 °C in 60 min, whereas, 70.2 % of the MB dye was degraded. Among all dyes, dye RB5 displayed maximum degradation percentage around 67.8 % at 5h with degradation rate $\sim -0.112 \text{ h}^{-1}$, due to the electrostatic interaction between RB5 and CuO. The highest percentage of dye removal/degradation is attributed to the larger surface area, smaller crystallite size, lower band gap of the catalyst respectively.

CHAPTER 4

PREPARATION, CHARACTERIZATION AND ELECTROCHEMICAL PROPERTIES OF SILICON NANOSTRUCTURES

4.1 Introduction

This chapter consists of the details of fabrication silicon nanostructures (Si NSs) using electrochemical etching technique, and the effect of current density and etching time on structural and optical properties of Si NSs. Testing of synthesized Silicon nanowires (NWs) as anode in Li ion cell and the effects of cycling on the structural, optical, electrochemical properties and the performance of the anode is also discussed.

Silicon (Si) is semiconducting material with an indirect-band gap. Si is abundant, eco-friendly, has high theoretical charge capacity (4,200 mAh/g) and low discharge potential, making it suitable for battery applications. However, conventional crystalline silicon by itself has practical limitation due to its large volume changes upon charge transportation, which leads to loss of electrical contact and capacity fading (Su et al. 2014). To solve these issues, various nanostructures (NSs) are nanopores (PS) and nanowires (NWs) from crystalline Si needs to be developed. Si NWs provide short diffusion ion paths, as well as, accommodate reversible volume changes during lithium ion extraction/insertion (Battaglia 2015). However, there are only few studies on the mechanical and structural properties, and how to control the volume changes in the Si NSs, during electrochemical cycling.

4.2 Preparation of Si NSs

Silicon substrates of n-type, (100) crystallographic orientation and a diameter of 7.62 cm has been used in all the experiments. Here, the complete process is performed in the two electrodes of an electrochemical cell. The silicon (Si) wafer with an area of $1 \times 2 \text{ cm}^2$ as anode, graphite foil of equal area as cathode and the solution of hydrofluoric acid with ethanol in 1:2 ratio was used as electrolyte. A DC current source was used to supply the current density in the range of 10-60 mA/cm² at the etching time of 0.5-1h. Finally, the samples were rinsed in de-ionized water and dried.

4.3 Results and Discussion

4.3.1 Structural and optical properties of PS at the different etching time

Fig. 4.1 (a) shows the topographical images of various PS samples. The pores grown along $\langle 100 \rangle$ directions were attributed to the electrochemical dissolution. In order to check the surface elements, the EDX testing is performed at a spatial region in all SEM images shown in Fig. 4.1(b). The porous layer contains four elements; oxygen (O), fluorine (F), and Carbon (C), which possibly arise from the electrolyte, and detected in very low quantity and Silicon (Si) obtained from the substrate in large quantity.

Fig. 4.1 (c-d) shows the pore size distribution in the form of a histogram from the image J Software based on more than 200 particles. Table 4.1 summarizes the morphological factors of pore mean size and inter pore distance based on image J analysis. As the etching time was increased, the pore mean size increased and the inter pore distance decreased. The increase in pore size was the result of active dissolution of Si at the pore wall. As the electrochemical dissolution process continued, dissolution also proceeded in the $\langle 111 \rangle$ direction, creating side branches from the main pore due to the availability of more holes. Propagation of pore preferentially occurred in such direction along with pore tip (Hollister 2005). However, dissolution in this direction came to a halt once the holes are depleted. This was due to the high

energy barrier created by the inter-pore distance, which became smaller with the progress of dissolution. This is in agreement with the work of Milani et al. (2006), who prepared PS from a low doped n-type Si with an etching time that ranged from 10 to 50 min at 25 mA cm⁻².

Table 4.1. Morphological parameters of PS samples prepared for various etching time.

Sample	Average pore size (nm)	Average inter pore distance (nm)
S1	238.98	6434.33
S2	1117.32	4362.13

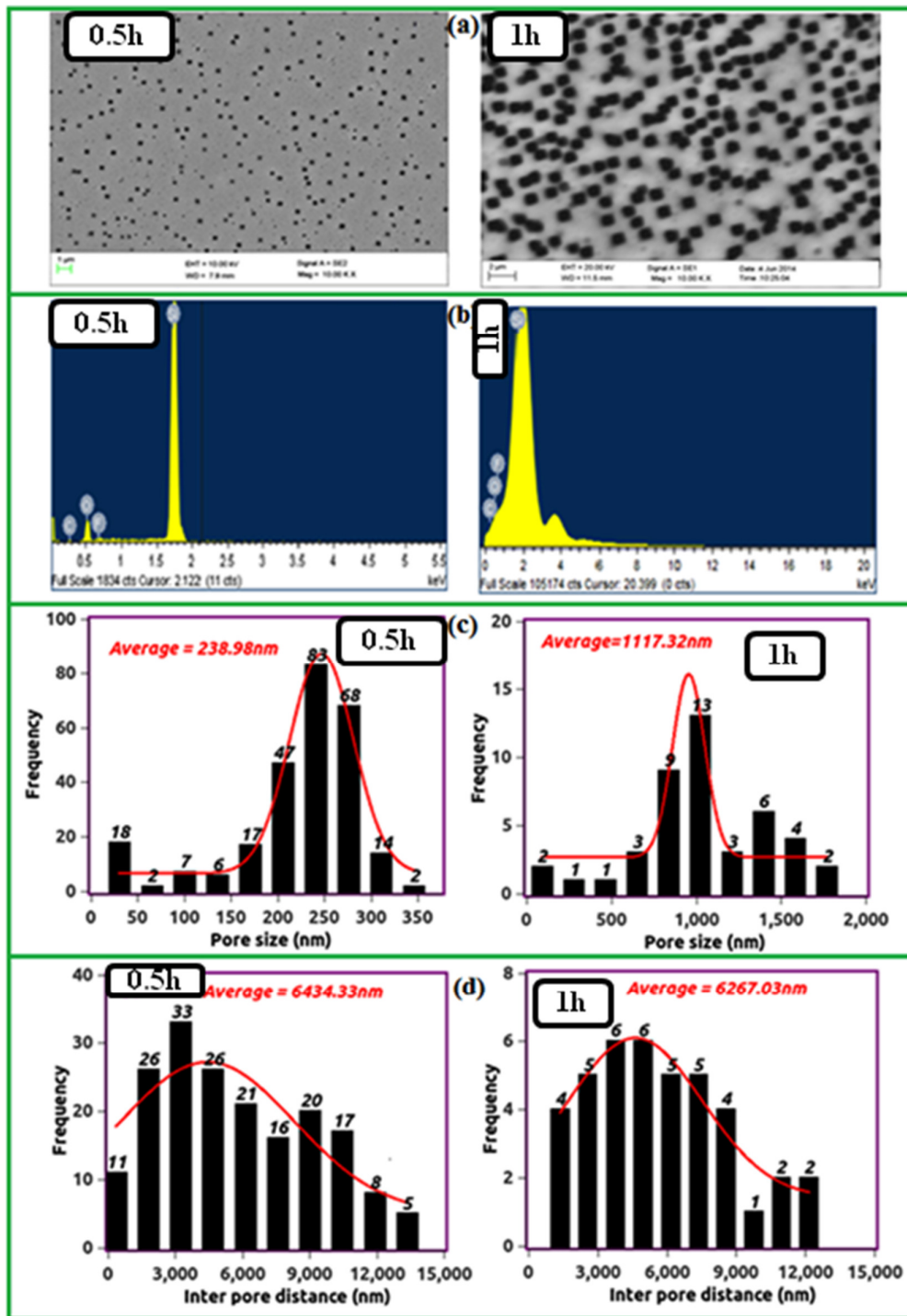


Fig. 4.1 (a) SEM images of PS on a (100) Si substrate at the various etching time, (b) EDAX pattern of the preparation of PS, (c) the porous size determination and (d) the inter pore size distribution based on image j software.

Fig. 4.2 shows IR spectrum in the range of 650-4000 cm^{-1} of PS/Si sample prepared at a constant current density of $10\text{mA}/\text{cm}^2$ for a time period of 1h. The spectrum reveals many distinct peaks with different intensities. The silicon-hydrogen bonds, such as wagging mode of SiH at 740.24, Scissor of SiH_2 at 899 and stretching mode at 2078.89 cm^{-1} are observed for hydrogen terminated silicon (Nayef 2013). The peak at 1031.73 and 1368 cm^{-1} indicates the presence of Si-O-Si wagging mode and SiOH, respectively, due to the interaction of surface of PS with moisture in the open atmosphere (Arce et al. 2006). A smaller peak at 1452 cm^{-1} corresponds to C=C stretching mode and another peak at 2346.94 cm^{-1} related to the presence of CO_2 (Yorikawa and Muramatsu 2000). The strong transmittance peak observed at $2850\text{--}2920\text{ cm}^{-1}$ indicates CH_2 symmetric stretching (Jayachandran et al. 2001). The carbon impurity originates probably from exposing PS to air, which is known to yield some carbon contamination (Thei\s s 1997), or due to washing in ethanol immediately after electrochemical anodization.

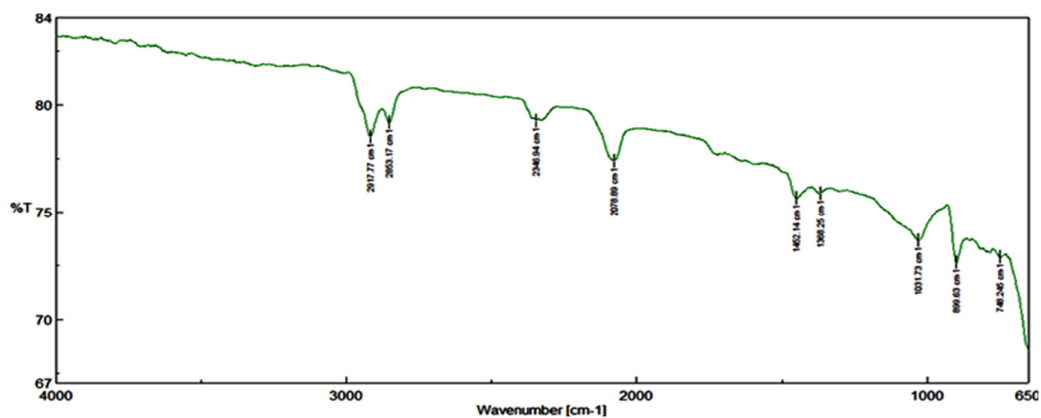


Fig. 4.2 FTIR spectra of freshly prepared PSLs at the etching time of 1h.

Fig. 4.3 (a) shows that the XRD spectrum of the sample of S2 in the range from 20° to 80° . Here, we have observed two diffraction peaks at $2\theta = 33.30$ and 69.50 with miller indices of (200) and (400), respectively. The peak at $2\theta = 33.3$ indicating the formation of pores on the Si surface and sharpness of the peak indicated that PS contained cubic crystalline structure. The peak at $2\theta = 69.50$ indicates crystalline silicon (c-Si). Fig. 4.3 (b) shows the Raman spectra for two PS samples with an etching time of 30 min and 1h. For all the samples, Raman line is narrow and

symmetric, centered at 520 cm^{-1} but the peak intensity increases with increasing etching time. The average size of the Si crystallites calculated using Eq. (4) are summarized in the Table 4.2.

Table 4.2. Raman parameters of PS samples prepared at various etching time.

Sample	Raman Peak (cm^{-1})	Crystallite size (nm)
30 min	520.87	122.77
1 h	520.32	24.88

Fig. 4.3 (c) shows the PL spectra of PS samples at the different etching times. There is a broad emission peak observed at 650 nm for the time period of 30 min. The origin of this peak is ascribed to radiative recombination of electron-hole pair in silicon nanocrystals, when the electrons transmit from a higher energy level to a lower energy level, followed by the absorbed energy corresponding to band gap. PS contained Si-H_x radicals interact with moisture and get oxidized, produce energy levels, and these energy levels are thought to be embedded in the silicon nanocrystallites in the PS (Lehmann and Gösele 1991). In longer etching time, the size of the silicon crystallite becomes smaller, distributed widely and their energy levels were discrete and have the large energy gap between them, which results in a intense emission peak. At the lower etching time, there is no luminescence observed because PS contains thin oxide layer on its surface and size of the crystallite becomes larger. They can act as photo absorptive states and their energy gaps are close to each other (Kim et al. 2004). When electron absorbs the photon energy, it is excited to higher energy level from lower energy level, after some time, it recombines with holes without losing energy because of the smaller band gap. In this case PL becomes almost undetectable.

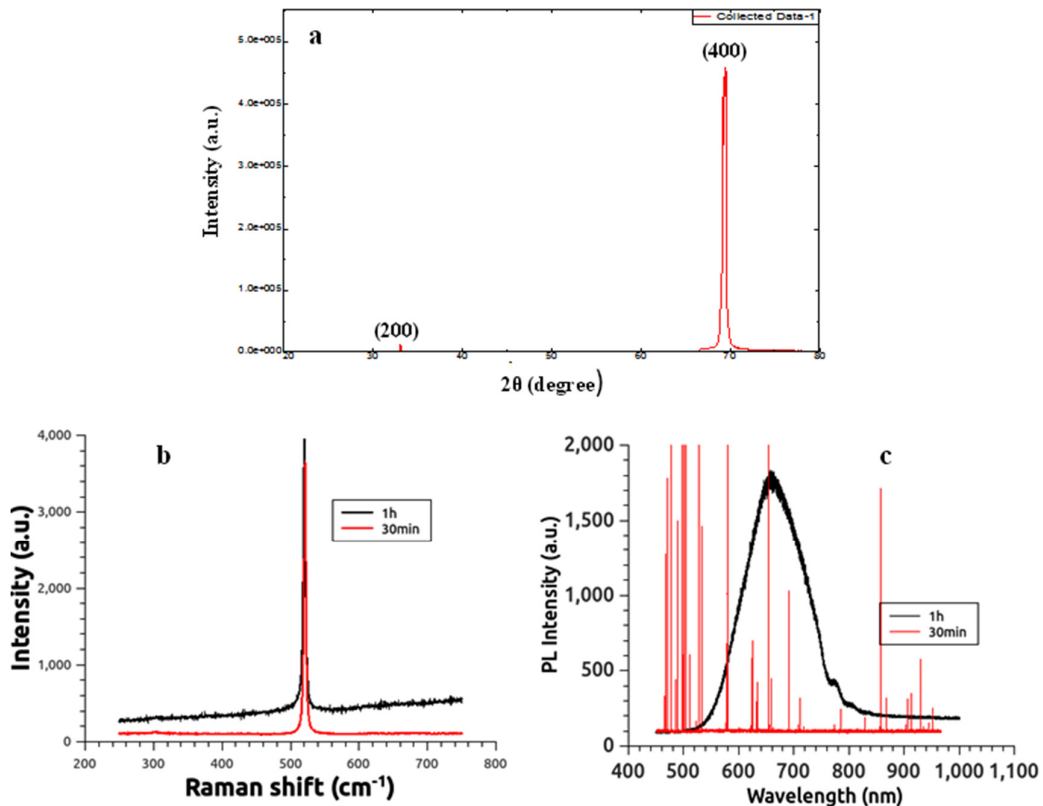


Fig. 4.3 (a) X-ray diffraction pattern of PS at the etching time of 30 min (b) Raman spectra of PS measured at the different etching time of 30 min and 1h. Fig. (c) PL spectra of PS.

4.3.2 Structural and optical properties of PS at the different current density

Fig. 4.4 (A) shows surface morphology of PS, consisting large number of pores distributed randomly over the surface. The pores are grown along $\langle 100 \rangle$ directions and attributed to the electrochemical dissolution. Fig. 4.4 (B) depicts the correlation of the pore depth (t) as a function of the current density. The pore depth increased with increase in current density due to increased rate of supply of holes. Fig.4.4 (C) shows the size distribution like pore dia (Fig. (C-a)) and the inter pore distance (Fig. (C-b)) based on image J Software. As shown in the Table 4.3, the increase in pore dia and decrease in the inter pore distance with current density was the result of active

dissolution of Si. The porosity was calculated from the following equation (Herino et al. 1987).

$$P = ((\pi/2) \times 1.732) [1/\{1+ (d/D)\}] \quad (46)$$

where, d is the inter pore distance and D is the pore dia.

Table 4.3 the structural parameters of PS samples. (where, t - pore depth, D - pore dia, θ - contact angle, d - inter pore distance, X – crystallite size, P – porosity, γ_s - surface free energy, w - base width, R - regularity ratio, R_{sk} surface skewness, R_q - RMS roughness, R_{ku} - surface kurtosis and R_a - average roughness).

Sample	t (μm)	D (nm)	d (nm)	X (nm)	θ^0	w	γ_s (mN/m)	P (%)	R	R_a	R_q	R_{sk}	R_{ku}
S1	12	312	1121	63	76	1.6	28	13	1	10	18	-4.2	26
S2	22	358	1009	35	112	1.2	6.9	19	6.2	13	21	-2.2	13
S3	48	524	930	20	120	1	4.4	35	17	66	69	0.08	1.2

Fig. 4.4 (D) shows the wettability graphs the PS. The contact angle enhanced with current density because of reduction in the base width. The surface tension of the PS is determined from the following equation (Shuttleworth 1950).

$$\gamma_s = (\gamma_L(1 + \cos\theta)^2)/4 \quad (47)$$

where, γ_s is surface free energy of PS, γ_L is the surface free energy of water (71.9 mN/m), θ is contact angle.

EDX analysis of sample S1 is shown in Fig. 4.4 (E). Si is present in large quantity from the substrate and oxygen (O), fluorine (F), Carbon (C) was detected in very low quantity from the electrolyte.

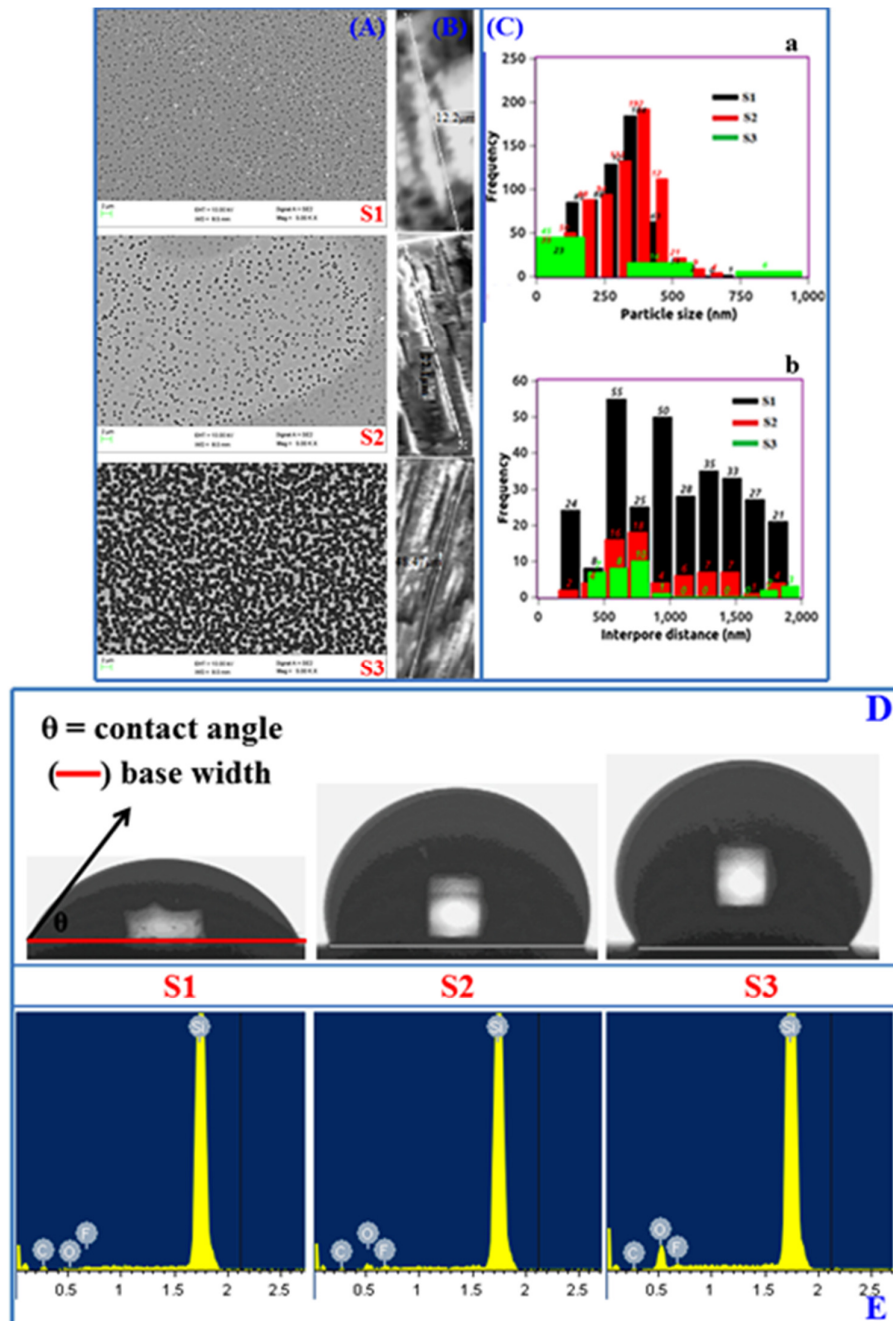


Fig. 4.4 (a) Plane view and (b) Cross-sectional views of SEM of PS samples (S1,S2,S3) at different current density, (c) Histograms showing particle size (up) and inter pore distance distribution (down) of PS samples, (d) Contact angle images of PS, (e) EDX spectrum of freshly prepared PS. The samples were labeled as S1-10, S2-20 and S3-30 mA/cm²

SEM images are analysed using two-dimensional FFT, to study the arrangement of nanopores as shown in Fig. 4.5 (a). The radial average is shown in Fig.4.5 (b) which helps in deriving the regularity ratio (R) of PS using equation (Stepniowski et al. 2014):

$$R = I/W \quad (48)$$

where, I is the intensity and W is the width of the radial average at half of its height. To measure the roughness parameters, such as average roughness (R_a), RMS roughness (R_q), surface kurtosis (R_{ku}) and surface skewness (R_{sk}) of the PS, as shown values in the table 1, the 3D topographical images of PS have been investigated using WSxM software as depicted in Fig. 4.5 (c-d). The average roughness of PS is 10, 13 and 66 for the sample of S1, S2, and S3, respectively. The surface average roughness increased with the increase in the current density due to increasing porosity and pore diameter (Sivakov et al. 2010). From Table 4.3, it can also be observed the RMS roughness of PS increased with increase in current density, because of increased number of nano-pores, leading to increase in the content of Si-H and its co-branches on the surface of PS. Using roughness skewness, on PS surface, the valleys were dominant at lower current density and peaks were dominant at higher current density. Using roughness kurtosis, at the lower current density (S1 & S2) PS contained the spiky surfaces; at the higher current density (S3) PS contains bumpy surfaces (Wang et al. 2006).

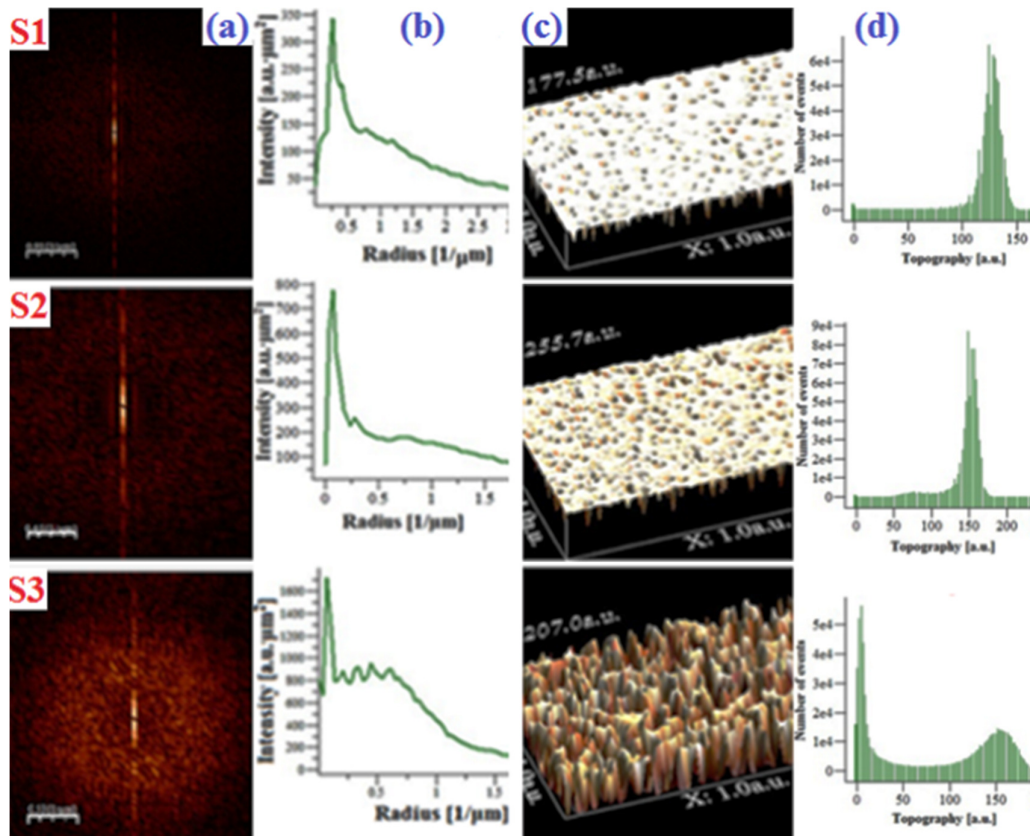


Fig. 4.5(a) FFT analysis of the PS, (b) Angular averaging of the FFT radial profiles, (c) Images obtained using WSxM software (d) Topography profiles of PS at various current densities (S1-10, S2-20 and S3-30 mA/cm²).

In Fig. 4.6 (a), FT-IR spectra reveals bonds from the various functional groups of molecules on the surface of PS. Initially, the freshly prepared PS layers possessed the silicon-hydrogen bonds, such as stretching mode of Si-H at the wave number of 2080 cm⁻¹, wagging mode of SiH₂ at ~ 670 cm⁻¹ and Si-H₂ scissor mode at ~ 900cm⁻¹, respectively. The asymmetrical stretching bonds of Si-O have been formed in the range of 1013.2 cm⁻¹ to 1090.2 cm⁻¹, when the freshly prepared PS was exposed to the open atmosphere. Peak at 1445.56 cm⁻¹ is due to CH₃ asymmetric deformation. The strong transmittance peak observed at 2915-2924 cm⁻¹ was assigned to the symmetric stretching mode of CH₂ [11].

Fig. 4.6 (b) shows the Raman peak at 520 cm^{-1} , arising from Si-Si vibrations of crystalline silicon. The size of the Si crystallites is calculated using Eq. (8). As shown in the Table 4.3, crystallite size reduced with increased the current density.

$$\text{Raman peak (cm}^{-1}\text{)} = 521.01(10X / (10X + 0.337)) \quad (49)$$

The Raman intensity increased with increased current density, because it is directly proportional to photon penetration length and Si crystalline density in the material (Guha et al. 1997). The optical properties of PS are shown in Fig. 4.6 (c-d). A red shift has been observed in peak positions of absorbance (UV-region) and photoluminescence with respect to the current density. The peak positions shifted towards the higher wavelength because, the oxidization of the PS layer enhanced with the increased of the current density, correspondingly the numbers of Si-H or Si-Si species reduced gradually. According to the electronic structure calculations, a decrease in the size of Si crystallites led to shift towards higher wavelength (Delley and Steigmeier 1995). On the other hand, an increase of the average roughness promotes an increase in the peak intensity in absorbance and photoluminescence, due to the increased concentration of granules over the surface layer of the PS.

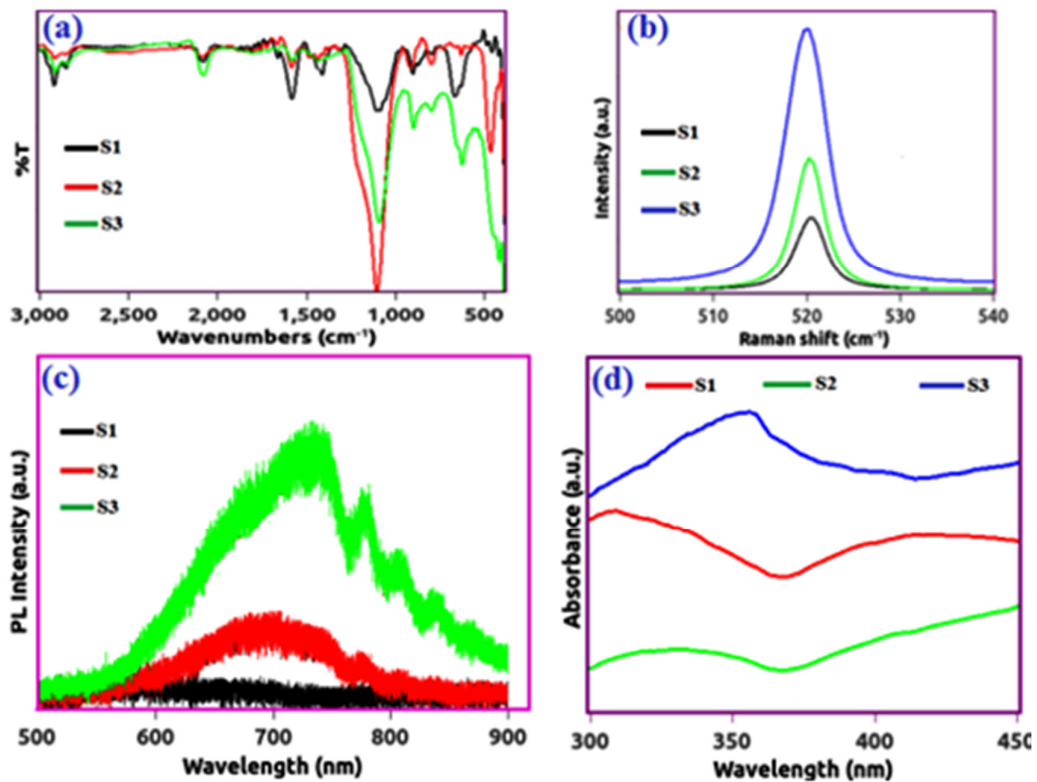


Fig. 4.6 (a) FTIR spectra of PS layers, (b) Raman spectra of PS layers for various anodization current densities (c) PL spectra of the PS (d) Absorption spectra of PS

4.3.3 Structural, optical and electrochemical properties of Si NWs

Fig. 4.7 (a) shows topographical images of Si NWs, possessing large number of NWs distributed randomly on the surface. The NWs are grown along $\langle 100 \rangle$ directions and attributed to the electrochemical dissolution. It can be also observed that the correlation of length of the NWs as a function of the current density. The length of the NWs increased with an increase in the current density due to increased the hole density. The surface elemental analysis of Si NWs also studied using EDS test as shown in Fig. 4.7(b), which was found to be identical of surface elemental analysis of PS as shown in Fig. 4.4(e).

Table 4.4 The calculated morphology parameters of Si NWs samples. (Where θ - contact angle (degree), X – crystallite size (nm), γ_s - surface free energy (mN/m), w - base width, R_q - RMS roughness (nm), λ_{max} - PL peak position (nm), R_a - average roughness (nm), R_{ku} - surface kurtosis and R_{sk} surface skewness.

Sample	γ_s	Θ	X	λ_{max}	R_q	R_{sk}	W	R_{ku}	R_a
S1	56.05	74.7	5.93	661.6	53.02	0.073	1.63	1.37	45.29
S2	41.73	120.4	4.89	659.4	60.40	0.227	1.01	1.98	52.59
S3	17.06	149.1	4.81	655.1	65.40	0.528	0.74	2.01	61.55

Fig. 4.7(c) shows the wettability graphs of Si NWs. The contact angle of Si NWs enhanced with an increase in the current density, because of reduction of the base width. The surface tension of the Si NWs is determined from the eqn. 2. The arrangement and roughness of Si NWs were analysed using FFT and WSxM software as depicted in the Fig. 4.8 (a-d). The structural parameters of Si NWs are illustrated in the Table 4.4. As shown in Fig. 4.8 (c-d), as the current density increased, the surface roughness of NWs increased, because of enhancement in the porosity on the individual NW.

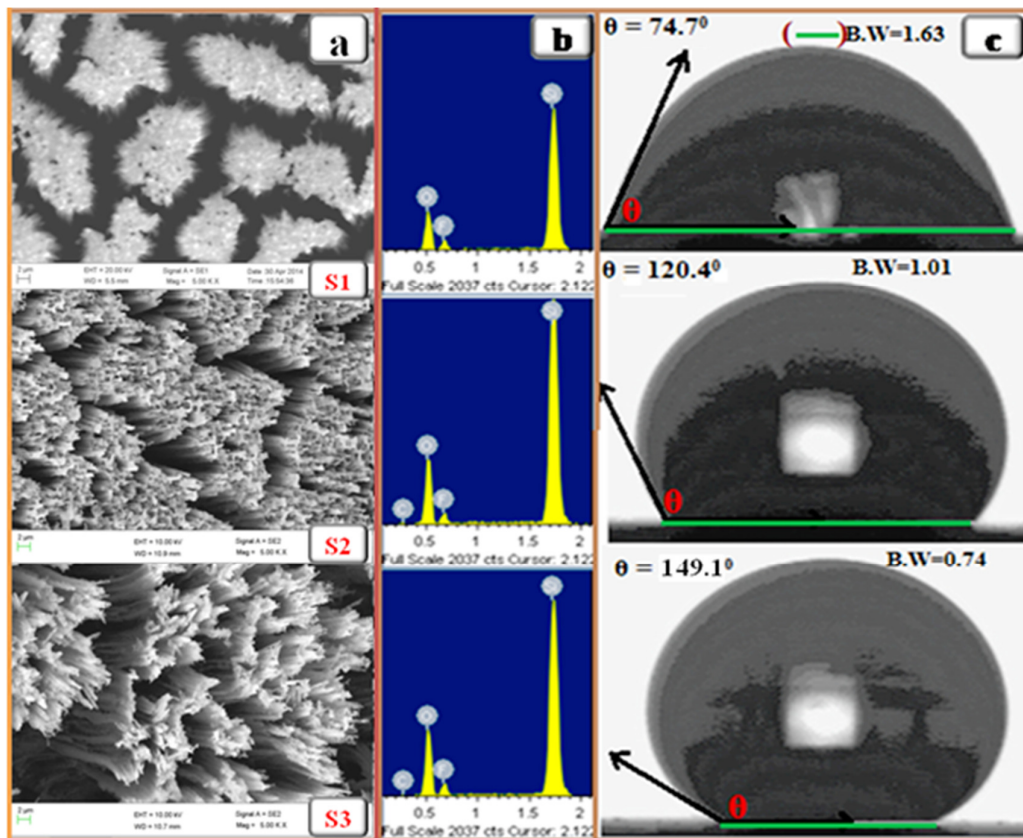


Fig. 4.7 (a) Plane view of SEM (b) EDS spectrum, and (c) contact angle images of Si NWs samples (S1,S2,S3) at different current density. The samples were labeled as S1- 40 mA/cm², S2 - 50 mA/cm² and S3 - 60 mA/cm²

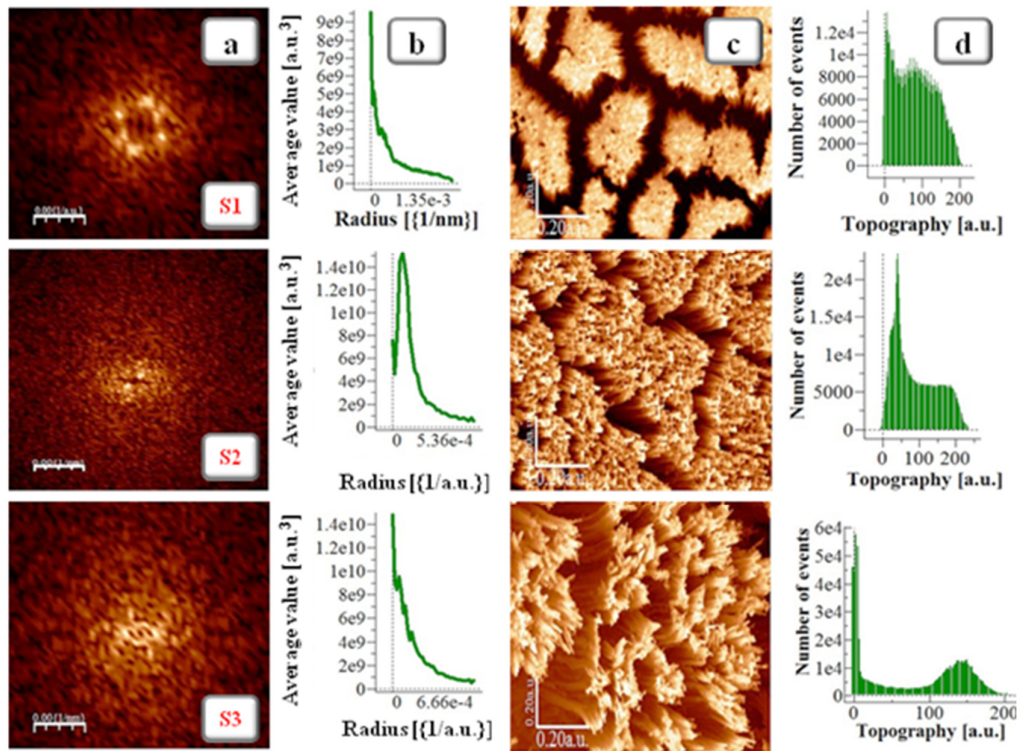


Fig. 4.8 (a) FFT analysis, (b) Angular averaging of the FFT radial profiles, (c) Images obtained using WSxM software, and (d) Topography profiles of Si NWs at various current densities (S1-40 mA/cm², S2 - 50 mA/cm² and S3 - 60 mA/cm²).

The FTIR spectrum in Fig. 4.9 (a) reveals all characteristics bonds of Si NWs. There is a significant change is seen in the spectrum of Si NWs, resulted from the various current densities. As the current density increased, the intensity of the transmittance band at 1430 and 1025 cm⁻¹ reduced, due to an increased exposure of the inner surface area to the atmosphere. A peak at 1445.56 cm⁻¹ is due to CH₃ asymmetric deformation. Fig. 4.9 (b) depicts the PL spectra of Si NWs at different current densities. The PL can be explained by the radiative recombination of excitons in small silicon nanocrystals at the NW sidewalls, in terms of a quantum confinement model. It is obvious that the intensity of PL emission reduces with increasing current density, due to decreased pristine Si and increased Si-O or Si-H species. The average grain size was determined using Eq. (9). It is clear that the PL edge slightly shifts towards lower wavelength from sample S1 to sample S3. As a result, grain size decreases.

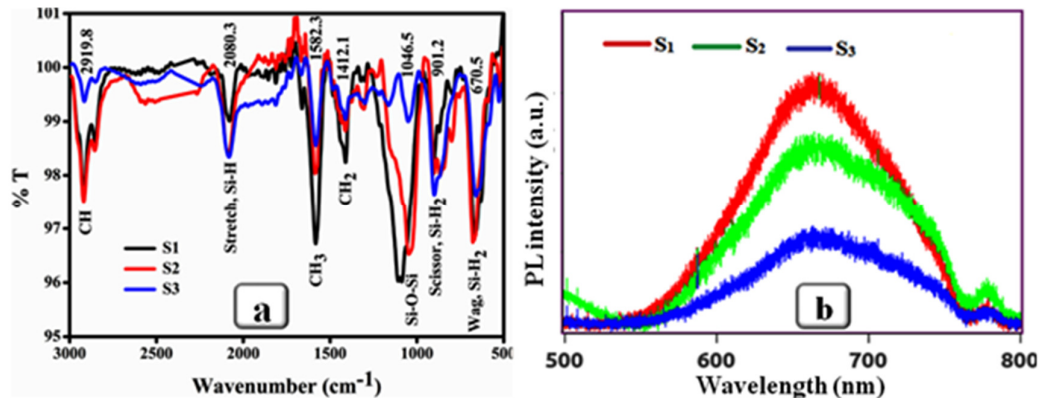


Fig. 4.9 (a) FTIR spectra and (b) PL spectra of Si NWs.

(a) Si NW anodes for Lithium ion battery applications:

To perform electrochemical operations, half-cell was assembled in argon atmosphere with moisture content <0.1 ppm, including Si NWs (sample-S2) as anode, lithium metal foil as cathode, polypropylene as separator, solution of 1M LiPF_6 in ethylene carbonate and diethyl carbonate in the volume ratio of 1:1 as electrolyte. The mass of the anode calculated using (Thakur et al. 2012); $M=d \times A_{\text{NW}} \times \rho_{\text{Si}}$, was $\sim 10^{-5}$ g. where ρ_{Si} , the density of crystalline silicon, is 2.33 gcm^{-3} , and A is the surface area and d, the average depth of Si NWs, is $70.5 \mu\text{m}$. The current is expressed according to the theoretical capacity of silicon ($1\text{C} = 3.58 \text{ A/g}$).

Fig. 4.10 (a) shows the electrochemical profiles of lithium ion cell. The cell was cycled between the voltages of 0 V to 1.5 V with current of $\pm 2 \text{ mA}$ at a different time. When the voltage rises through 0.1 V to 0.22 V, anode shows slight dilation. However, when the cell charges (lithium ion insertion) from 0.22 V to 0 V, the thickness of anode increases. Upon discharging (lithium ion extraction) the cell, anode thickness decreases from 0 V to 0.45 V, anode shows slight shrinkage in a voltage range 0.45 - 1.5. Then, resulted DC current turned on and off periodically. The area of the loop in the cell is directly proportional to the total energy that battery delivered. In Fig. 4.10 (b), the energy fade may be regarded as a good indicator for the practical performance of lithium ion cell. Notably, the discharge energy fade is significantly lower than the charge energy fade, possibly indicating an asymmetrical lithium ion transport limitation in the cell during cycling. In addition, the energy

efficiency has been calculated from the dynamic response as shown in the top portion of Fig. 4.10 (b). The energy efficiency significantly deteriorated for the first few cycles and later it stays almost stable for remaining cycles. The stable energy efficiency indicates that lithium ion cell follows medium to high power.

The cycling performance of the Si NWs is presented in Fig. 4.10 (c-d). The galvanostatic cycling tests were performed between 0 and 1.5 V (vs. Li⁺/Li) at a rate 1C. As seen in Fig. 4.10 (e), the specific capacity gradually decreases with an increase in cycle number, which is attributed mainly to the growth of solid electrolyte interface (SEI) film on the electrode. However, the attained maximum charge and discharge capacity for the first cycle is 3452.47 mAh/g and 2963.57 mAh/g, respectively, claiming that the initial coulombic efficiency, defined as the ratio of the amount of lithium ion extraction over lithium ion insertion, is 85.8 %. This is higher than reported observations (Yao et al. 2011)(Kim et al. 2013). As can be seen in the inset of Fig. 4.10 (e), the charge and discharge potential of the cell was almost stable at 5.2 mV and 1.51 V for the initial 50 cycles, eventually at 9 mV and 1.52 V for remaining cycles, respectively. The charge potentials are much lower than the previous report (Kohandehghan et al. 2014). The maximum specific capacity of Si NWs as anode in the present work is found to be more than the reported values, as shown in the Table 1A.

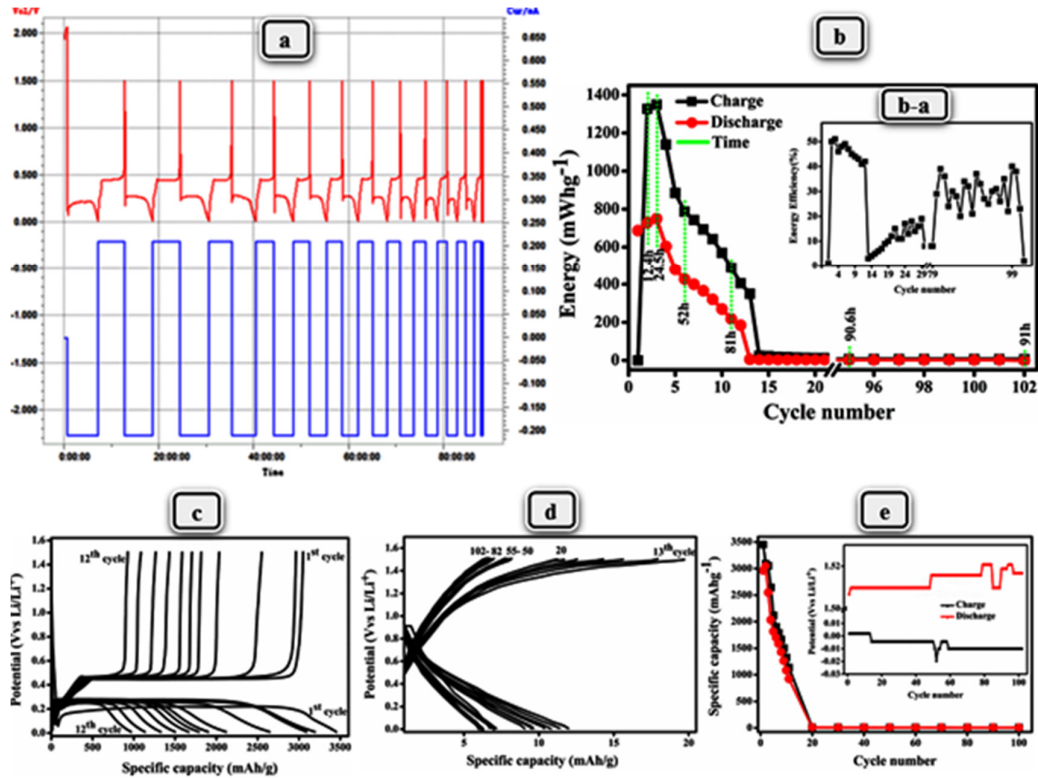


Fig. 4.10 (a) Electrochemical profiles of anode as a function of time, (b) comparing of cycle behavior with energy and energy efficiency (inset) of anode, profiles of voltage versus capacity for anode during (c) first 12 cycles and (d) cycle from 13 to 102, and (e) comparison of cycling behavior with specific capacity and potential (inset) of anode.

Table 4.5 Reported values for the electrochemical parameters of Si NWs as anode

S. No.	Charge capacity (F/g)	Discharge capacity (F/g)	Columbic efficiency (%)	Reference
1	3452.47	2963.57	85.8	present
2	1368	2440	56	(Kang et al. 2011)
3	3544	2725	77	(Yan et al 2016)
4	1987	1536	77.3	(Jung et al. 2006)
5	2014	1836	91	(Vidhya et al. 2009)
6	3000			(Barbara et al. 2015)
7	2000			(Shruti et al. 2010)
8	1970	2615	73	(Rigved et al. 2005)

Fig. 4.11 depicts the interpretation of the anode volume change on the cyclic behaviour as a function of the structural change and cell voltage. At 1st cycle, the cell was first recharged to 3 mV with a long taper time of 2 h, causing homogeneous ion diffusion in the anode. After this, the lithium-silicon alloys (Li_xSi_y) continuously experience structural change, between the simple cubic phase (C_1) and new simple cubic phase (C_2) due to lithium-ion deintercalation (intercalation) during the charge (discharge) process. This reveals that the volume change of anode at the 13th cycle becomes more than the 12th cycle, when the cell voltage increases from 3 mV to 3.5 mV, leading to inhomogeneous lithium ion diffusion in the electrode. However, the Li_xSi_y structure on the anode remains in the C_1 phase at a cell voltage of 3 mV, during the 12th cycle, due to slow lithium ion diffusion, as evidenced by the SAED. After the cell voltage increased to 5.2 mV, C_1 and C_2 phases coexists in the Li-Si structure, and the volume of the outer region in anode decreases with cycling as demonstrated in

Fig.4.11. In orderly, the outer region of nanowires is removed from the anode with a smaller taper time, the inner region of an anode holds residual silicon ions and attains the C₂ phase at the end of 20th cycle. Interestingly, few diffraction spots in the SAED pattern are better indication of the Si NWs before the 20th cycle, as well as, after 20th cycle. Consequently, the Li-Si structure reset to the C₂ phase at the end of the cycling, and the volume change of anode after 50th cycle is larger than the earlier cycles, as seen in cycles 20 and 50, at a voltage of 5.2 mV, due to much slower lithium ion diffusion. This leads to cracks and pulverization of anode instead of contributing to lithiation. After 102 cycles, continuous growth of solid state interface layer on the pulverized surface induces a significant increase in resistance, loss of cyclable Li ions and electrochemical isolation of individual Si NWs, leading to the complete deactivation of Si, and resulting in null or very low capacity of the cell.

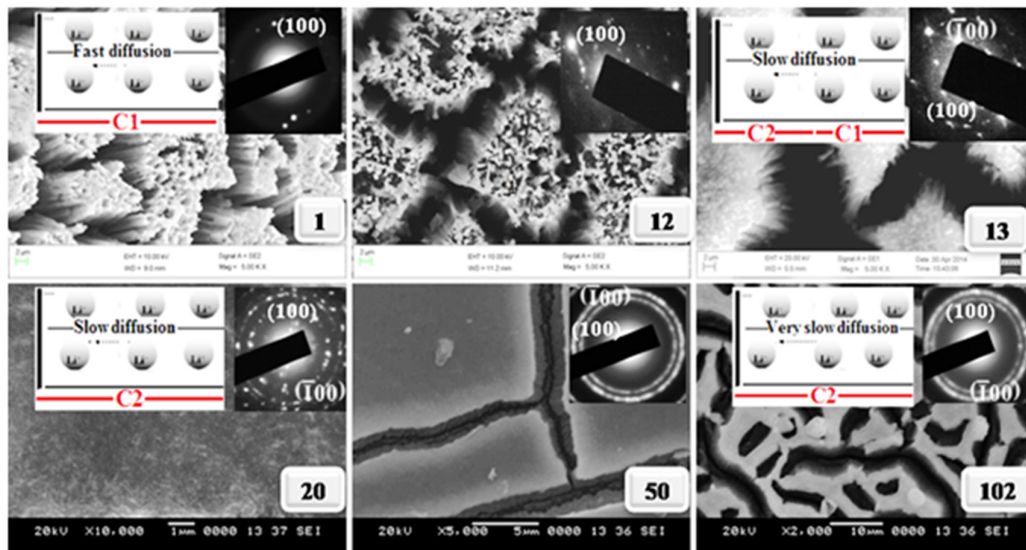


Fig. 4.11 SEM/SAED micrographs of anode at various cycle number.

As seen above, the charge transfer process in the cell could be related to the magnitude of the shrinkage/extension of an anode, as a result, the structural and optical properties may change accordingly. From Raman spectra (Fig. 4.12 (a)), the average crystallite size (D) of an anode, calculated using Eq. (5), increases upon cycling. At low cycle number, crystallites are smaller, resulting in broadening of the

Raman peak. At higher cycle number, crystallinity is more, whereas the peak width is narrow and hence larger crystallites are formed. Using the above crystallite values, the dislocation density (δ), which reveals the amount of defects in a unit volume of anode, has been estimated using Eq. (6). Dislocation density decreases with an increase of cycle number, due to decrease in the number of imperfections and grain boundaries with an increase in the crystallite size of an anode.

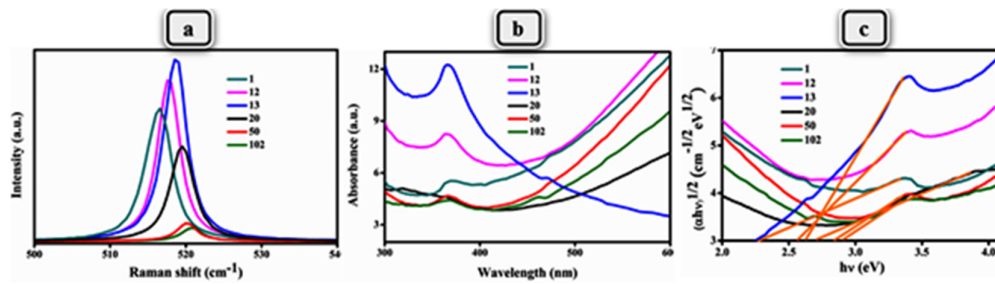


Fig.4.12 (a) Raman (b) UV-visible absorption and (c) band gap spectra of anode at various cycles.

Fig. 4.12 (b-c) shows the absorbance and band-gap energy of Si NW anode. As shown in Fig. 4.12 (b), all samples show absorption at nearly visible region of the electromagnetic spectrum, due to the d-d transitions of silicon ions in the anode. The band-gap energy E_g for the anode was estimated using Eq. (11). The optical band gap was obtained by extrapolating the linear portion of the curve to intersect the energy axis, as shown in the Fig. 4.12 (c). An increase in the band gap is attributed to decrease in the dislocation density of an anode upon cycling. The surface area of an anode estimated using image J software of SEM images, show decreasing trend with cycle number. The structural and optical parameter values are given in the Table 4.5.

Table 4.6 The physical properties of anode as a function of cycle number.

Cycle. no	Band gap (eV)	Raman position (cm ⁻¹)	Crystallite size (nm)	Dislocation density ×10 ¹⁵ (m ⁻²)	Surface area ×10 ³ (μm ²)	Specific capacity (mAhg ⁻¹)
1	2.26	516.90	4.65	46.2	1.586	3452.4
12	2.56	517.51	4.98	40.3	1.364	1134.3
13	2.62	518.53	7.04	20.1	1.121	13.5
20	2.70	519.52	11.75	7.2	0.022	9.0
50	2.83	520.11	19.47	2.6	0.019	7.1
102	2.90	520.87	125.38	0.06	0.056	0

4.4 Conclusions

Porous silicon layers were prepared via electrochemical etching method for different etching time, as well as current density. The pore diameter increases and the inter-pore distance decreases, when the etching time and current density was increased. The XRD spectra of PS layer showed a sharp peak at $2\theta=69.5^\circ$, which confirmed that the crystalline properties of PS. From FTIR in PS, on as-prepared samples, Si-H, Si-OH, Si-O-Si species and carbon related groups were measured successfully. From FFT and WSxM analysis, regularity ratio and average roughness of the Si NSs increased with increase in the current density. The Raman analysis showed that the peak intensity sharply increases with increase of etching time, because porosity increases. The average size of nanocrystals obtained by Raman line shape analysis is found to be in the range of 122.7 - 24.8nm. Investigation of the PL properties revealed that the PS shows an intense emission band at the wavelength of 650nm, because of the radiative process, associated with surface oxidation. The electrochemically etched Si NWs, as Lithium ion battery anode provides several benefits at a low cycle number. Firstly, the individual NWs provide better electrical conductivity than smooth films due to low thickness of SEI layer that enhances specific capacity. Secondly, micro-porosity helps to accommodate volume changes during cycling, without losing the structural integrity and enables easy infiltration of electrolyte and fast Li ion diffusion, resulting in high coulombic efficiency.

CHAPTER 5

SUMMARY AND FUTURE DIRECTIONS

5.1 Summary

5.1.1 Growth, characterization and catalytic activity of MnO₂ and rGO/MnO₂ NWs

MnO₂ nanowires were grown using the hydrothermal process and studied the effect of KMnO₄ concentration on it.

According to XRD pattern, α -MnO₂ nanowires are well crystallized tetragonally in the [211] lattice planes. The mean crystallite size of α -MnO₂ nanowires was obtained using Debye-Scherrer formula. It increased linearly within the range of 15-25 nm as the concentration of oxidizer was increased in the range of 0.21-0.63 mmol, at a fixed hydrothermal temperature and duration.

Nanostructured α -MnO₂ has an absorption band in the wavelength range of 210–400 nm and a broad absorption band in the region of 410–800 nm, respectively. The absorption band in UV region may be attributed to the electron transition from valence bands to conduction bands. The optical absorption of MnO₂ nanostructures in the visible light range originate mainly from d–d transitions of Mn ions. The absorption spectra of α -MnO₂ exhibit a band gap of 2.55 to 1.27 eV, which is red shifted with tuning KMnO₄ concentration.

It was found that the prepared α -MnO₂ exhibit high catalytic activity for the degradation of RB-5. The degradation result could be related to the structural and optical properties of the nanostructured catalyst. Furthermore, Fenton catalytic mechanism investigations demonstrate that OH[•] and O₂[•] play the key role in the Fenton process.

A composite of graphene oxide supported by needle-like MnO₂ (rGO-MnO₂ NWs) has been fabricated through a simplest hydrothermal route, whereas rGO nanosheets were prepared using modified hummer method and KMnO₄ and NaNO₃ as reagents.

SEM micrographs conform that MnO₂ NWs grew on the surface of rGO sheets that acted as substrates for the nucleation of MnO₂ NWs, indicating a heterogeneous nucleation. The average surface area, from BET analysis, calculated for rGO/ MnO₂ NWs is about 59.1 m²g⁻¹, whereas for pristine MnO₂ NW it is about 37.7 m²g⁻¹. The increased surface area of NWs is due to the presence of rGO nanosheets in the rGO/MnO₂.

From XRD, all the diffraction peaks in the undoped and rGO doped MnO₂ nanowires are well matched with the body-centered tetragonal phase, with lattice constants $a = b = 9.7847 \text{ \AA}$ and $c = 2.8630 \text{ \AA}$. The broad diffraction peak positioned at 23.5 corresponds to (002) plane, indicates the presence of an rGO. The interlayer spacing of rGO was 0.37 nm, slightly larger than that of graphite, which resulted from a small amount of residual oxygen-containing functional groups or other structural defects. The mean crystallite size, determined using Debye-Scherrer formula, was found to decrease within the range of 14-23 nm, for rGO-MnO₂ nanowires compared to bare MnO₂ nanowires.

Raman spectra display three core peaks at 506 cm⁻¹, 565 cm⁻¹, and 648 cm⁻¹ identified with MnO₂ NWs. The characteristics peaks of rGO centered at 1345.8 cm⁻¹ and 1596 cm⁻¹ were attributed to D-band and G-band, respectively. The I_D/I_G ratio is reduced slightly from 0.99 for rGO to 0.97 for rGO/MnO₂ NWs, which can be attributed to an increase in defects on the surface of the reduced GO, that were induced during hydrothermal reduction.

The catalytic activities of undoped and rGO doped MnO₂ nanowires were investigated through the degradation processes of the RB-5 solution under dark. The obtained results designated that the as-synthesized rGO/MnO₂ nanowires have higher photo-degradation efficiency of RB-5 (84%) as compared with MnO₂ nanowires (63%), which is due to the higher surface area, large dislocation density. Influences of

concentration of dye, H_2O_2 and rGO/MnO₂ on the degradation of RB-5 were examined.

Doping with Sn improves the specific capacitance of electrodes. According to CV study, the specific capacitance of MnO₂, rGO-MnO₂ and Sn@rGO-MnO₂ was found to be 139.05, 309.7 and 460.9 Fg^{-1} at a scanning rate of 20 mVs^{-1} , in an aqueous Na_2SO_4 solution (1 M) respectively, for super capacitor electrode applications.

5.1.2 Growth, properties and adsorption/photocatalytic activity of NiO nanoparticles

Nickel oxide (NiO) nanoparticles were successfully synthesized via thermal decomposition of the precursor nickel nitrate hexahydrate.

The X-ray diffraction pattern studies revealed the NiO has a face-centered cubic (FCC) structure and confirmed the presence of high degree of crystallinity of NiO nanoparticles. The mean crystallite size of NiO samples increases in the range of 2-5.4 nm with increase in annealing temperature in the range of 200-400 °C.

SEM images revealed that prepared NiO products have smooth and uniform particle morphology with an average diameter of several nanometers. The estimated surface area of NiO nanoparticles by image J analysis reveal that it increases with the increase in annealing temperature.

The UV-visible spectra of NiO showed a strong absorption peak at visible region. The band gap energy is found to be in the range of 4.1 to 2.3 eV, with increasing annealing temperature, which is attributed to the better quantum confinement effect.

The removal of RB-5 and photocatalytic degradation of MB in water was studied using NiO in the absence/presence of visible light irradiation. The obtained results indicate that the photocatalytic degradation yield increased from 50.8 % up to 70.2 %, whereas removal yield increased from 65 % to 87.2 % with increasing annealing temperature, when activated NiO based nanoparticles were used for an irradiation

time of 6 hours. The degradation rate of MB and removal rate of RB-5 could be well described by the first and second order kinetics, respectively.

5.1.3 Synthesis, characterization and Photo-catalytic activity of CuO nanoparticles

CuO nanoparticles were synthesized by precipitation method using the precursor of copper (II) nitrate trihydrate. This method has many advantages such as economic viability, ease to scale up and less time consuming.

It is observed from the structural analysis that the CuO nanoparticles are monoclinic in nature with lattice constants of $a = 4.6500 \text{ \AA}$, $b = 3.410 \text{ \AA}$, $c = 5.110 \text{ \AA}$ and $\alpha = \gamma = 90^\circ$, $\beta = 99^\circ$.

The SEM image displayed agglomerated Cu nano particles, spherical in shape. The UV-Visible absorption spectrum of CuO nanoparticles shows a strong absorption peak at about 437.6 nm, assigned to the electronic transition from n to π^* molecular orbitals of the ligand, which is a good evidence of CuO NPs. The band gap energy calculated from the absorption spectra, was estimated around 1.76 eV, that is lower than the reported value for the bulk CuO (1.85 eV)

As prepared CuO nanoparticles are used as acatalyst for photocatalytic degradation of RB-5, MB, and AY-23, which are organic pollutants. CuO showed excellent activity for the photo degradation of RB-5 under visible light irradiation, with efficiency estimated to be 67.8 % at 5h illumination. The catalysis isotherm equations like pseudo order types were applied and the values of their respective constants were evaluated by adopting the graphical method. The degradation rate for all the dyes followed the pseudo first order kinetics.

5.1.4 Structural, optical and electrochemical properties of Si NSs

The contact angle of PS reduced from 120.1° to 76° as the current density was reduced from 30 to 10 mA/cm². The contact angle of Si NWs reduced from 149.1° to 74.7° as we reduced the current density from 60 to 40 mA/cm².

The surface roughness of PS was reduced from 66 nm to 10 nm, as the current density was reduced from 30 to 10 mA/cm²

The surface roughness of Si NWs reduced from 61.5 nm to 45.2 nm, as the current density was reduced from 60 to 40 mA/cm².

The average size of nanocrystals in the PS is obtained from Raman spectra and is found to be in the range of 122.7 - 24.8 nm.

The average size of nanocrystals in the Si NWs from Photoluminescence found to reduce from 5.9 nm to 4.8 nm, when the current density is increased from 40 to 60 mA/cm².

The specific capacity of the anode reduced from ~ 3452.47 mAhg⁻¹ to 1134.34 mAhg⁻¹ with increased cycle number from 1st to 12th at a current rate of 1C.

5.2 Future directions

The study of structural, optical, adsorption and catalytic properties will be beneficial for the synthesis of new nanomaterials for industrial applications. Over all, the study will provide a better understanding of the effect of various physical parameters viz, concentration, temperature dopants, annealing on size, shape, surface area, bandgap and crystallite size on the performance of the nanomaterials.

To improve the quality, growth and catalytic activity of nanostructures of transition metal oxides such as nickel oxide and copper oxide etc., for the sake of water treatment, there exists a possibility to study the effect of concentration of reagents and dopant, like the reduced graphene oxide and metal nanoparticles.

The present study is concentrated on MnO₂, NiO and CuO based nanostructures for the adsorption, chemical catalysis, and photo catalysis. However, these metal oxide nanostructures can be explored for the photo electrochemical and gas sensing, solar cell applications. Addition of new impurities atoms (Al, Sn, C, Fe, etc.) into MnO₂, NiO, and CuO may be studied to achieve improved properties.

It is also worth to explore the synthesis of such transition metal oxide nanostructures using various techniques, such as spray paralysis, sol-gel, DC sputtering, RF sputtering, and microwave irradiation. Embedding these nanostructures in the matrix or template like silicon, alumina etc, to investigate their catalytic properties for the degradation of effluents in the presence of UV/visible light is also desirable.

To extend the preparation and application of porous Silicon nanoparticles and Si nanowire arrays for battery applications, the Si-Graphene nanocomposite is another system of choice, because graphene can wrap the Si nanoparticles/nanowires and increase the conductivity resulting in enhanced capacity.

Also Silicon-metal nanocomposite is of particular interest, because the metal nanoparticles (Copper/Tin/Silver) deposited on Silicon nanostructures (nanowires, nanoparticles) will act as cushion reducing the stress/strain in the Si and help reducing the cracks originating from volume change.

References

- Asbrink, S., and Norrby, L.-J. (1970). "A refinement of the crystal structure of copper (II) oxide with a discussion of some exceptional esd's." *Acta Crystallogr. B*, 26(1), 8–15.
- Abdolhosseinzadeh, S., Asgharzadeh, H., and Kim, H. S. (2015). "Fast and fully-scalable synthesis of reduced graphene oxide." *Sci. Rep.*, 5.
- Abdul Rahman, I., Ayob, M. T. M., and Radiman, S. (2014). "Enhanced photocatalytic performance of NiO-decorated ZnO nanowhiskers for methylene blue degradation." *J. Nanotechnol.*, 2014.
- Aguilar, Z. G., Brillas, E., Salazar, M., Nava, J. L., and Sirés, I. (2017). "Evidence of Fenton-like reaction with active chlorine during the electrocatalytic oxidation of Acid Yellow 36 azo dye with Ir-Sn-Sb oxide anode in the presence of iron ion." *Appl. Catal. B Environ.*, 206, 44–52.
- Akpan, U. G., and Hameed, B. H. (2009). "Parameters affecting the photocatalytic degradation of dyes using TiO₂-based photocatalysts: a review." *J. Hazard. Mater.*, 170(2), 520–529.
- Ali, A. E.-H., Raafat, A. I., Mahmoud, G. A., Badway, N. A., El-Mottaleb, M. A., and Elshahawy, M. F. (2016). "Photocatalytic decolorization of dye effluent using radiation developed polymeric nanocomposites." *J. Inorg. Organomet. Polym. Mater.*, 26(3), 606–615.
- Ali, L., Alhassani, H., Karuvantevida, N., Rauf, M. A., and Ashraf, S. S. (2014). "Efficient aerobic degradation of various Azo dyes by a *Sphingomonas* sp isolated from petroleum sludge." *J. Bioremediation Biodegradation*, 5(3), 1.
- Al-Sehemi, A. G., Al-Shihri, A. S., Kalam, A., Du, G., and Ahmad, T. (2014). "Microwave synthesis, optical properties and surface area studies of NiO nanoparticles." *J. Mol. Struct.*, 1058, 56–61.
- An, K. H., Kim, W. S., Park, Y. S., Jeong, H. J., Choi, Y. C., Moon, J.-M., Bae, D. J., Lim, S. C., and Lee, Y. H. (2001). "Supercapacitors using singlewalled carbon nanotube electrodes." *AIP Conf. Proc.*, AIP, 241–244.
- Arce, R. D., Koropecski, R. R., Olmos, G., Gennaro, A. M., and Schmidt, J. A. (2006). "Photoinduced phenomena in nanostructured porous silicon." *Thin Solid Films*, 510(1), 169–174.

- Bagal, M. V., and Gogate, P. R. (2014). "Wastewater treatment using hybrid treatment schemes based on cavitation and Fenton chemistry: a review." *Ultrason. Sonochem.*, 21(1), 1–14.
- Battaglia, V. (2015). "Capacity Fading Research on Si Anode in Lithium Ion Batteries." *228th ECS Meet. Oct. 11-15 2015*, Ecs.
- Beaudrouet, E., La Salle, A. L. G., and Guyomard, D. (2009). "Nanostructured manganese dioxides: Synthesis and properties as supercapacitor electrode materials." *Electrochimica Acta*, 54(4), 1240–1248.
- Bindu, K., Sridharan, K., Ajith, K. M., Lim, H. N., and Nagaraja, H. S. (2016). "Microwave assisted growth of stannous ferrite microcubes as electrodes for potentiometric nonenzymatic H₂O₂ sensor and supercapacitor applications." *Electrochimica Acta*, 217, 139–149.
- Bouazizi, N., Bargougui, R., Oueslati, A., and Benslama, R. (2015). "Effect of synthesis time on structural, optical and electrical properties of CuO nanoparticles synthesized by reflux condensation method." *Adv Mater Lett*, 6(2), 158–164.
- Bowley, H. J., Gerrard, D. L., Loudon, J. D., and Turrell, G. (2012). *Practical raman spectroscopy*. Springer Science & Business Media.
- Bradu, C., Frunza, L., Mihalche, N., Avramescu, S.-M., Neață, M., and Udrea, I. (2010). "Removal of Reactive Black 5 azo dye from aqueous solutions by catalytic oxidation using CuO/Al₂O₃ and NiO/Al₂O₃." *Appl. Catal. B Environ.*, 96(3), 548–556.
- Brunauer, S., Emmett, P. H., and Teller, E. (1938). "Adsorption of gases in multimolecular layers." *J. Am. Chem. Soc.*, 60(2), 309–319.
- Cavani, F., and Trifiro, F. (1999). "Selective oxidation of light alkanes: interaction between the catalyst and the gas phase on different classes of catalytic materials." *Catal. Today*, 51(3), 561–580.
- Chatterjee, S., Lim, S.-R., and Woo, S. H. (2010). "Removal of Reactive Black 5 by zero-valent iron modified with various surfactants." *Chem. Eng. J.*, 160(1), 27–32.
- Chen, J., Yao, B., Li, C., and Shi, G. (2013). "An improved Hummers method for eco-friendly synthesis of graphene oxide." *Carbon*, 64, 225–229.
- Chen, S., Zhu, J., Wu, X., Han, Q., and Wang, X. (2010). "Graphene oxide- MnO₂ nanocomposites for supercapacitors." *ACS Nano*, 4(5), 2822–2830.

- Cheng, F., Su, Y., Liang, J., Tao, Z., and Chen, J. (2009). "MnO₂-based nanostructures as catalysts for electrochemical oxygen reduction in alkaline media." *Chem. Mater.*, 22(3), 898–905.
- Cheng, G., Yu, L., Lin, T., Yang, R., Sun, M., Lan, B., Yang, L., and Deng, F. (2014). "A facile one-pot hydrothermal synthesis of β -MnO₂ nanopincers and their catalytic degradation of methylene blue." *J. Solid State Chem.*, 217, 57–63.
- Cheng, J.-S., Du, J., and Zhu, W. (2012). "Facile synthesis of three-dimensional chitosan–graphene mesostructures for reactive black 5 removal." *Carbohydr. Polym.*, 88(1), 61–67.
- Chong, M. N., Cho, Y. J., Poh, P. E., and Jin, B. (2015). "Evaluation of Titanium dioxide photocatalytic technology for the treatment of reactive Black 5 dye in synthetic and real greywater effluents." *J. Clean. Prod.*, 89, 196–202.
- Choplin, A., and Quignard, F. (1998). "From supported homogeneous catalysts to heterogeneous molecular catalysts." *Coord. Chem. Rev.*, 178, 1679–1702.
- Delley, B., and Steigmeier, E. F. (1995). "Size dependence of band gaps in silicon nanostructures." *Appl. Phys. Lett.*, 67(16), 2370–2372.
- Dresselhaus, M. S., and Araujo, P. T. (2010). *Perspectives on the 2010 Nobel Prize in physics for graphene*. ACS Publications.
- Ebraheem, S., and El-Saied, A. (2013). "Band gap determination from diffuse reflectance measurements of irradiated lead borate glass system doped with TiO₂ by using diffuse reflectance technique." *Mater. Sci. Appl.*, 4(05), 324.
- El-Kemary, M., Nagy, N., and El-Mehasseb, I. (2013). "Nickel oxide nanoparticles: Synthesis and spectral studies of interactions with glucose." *Mater. Sci. Semicond. Process.*, 16(6), 1747–1752.
- El-Safty, S. A., Kiyozumi, Y., Hanaoka, T., and Mizukami, F. (2008). "Heterogeneous catalytic activity of NiO-silica composites designated with cubic Pm3n cage nanostructures." *Appl. Catal. B Environ.*, 82(3), 169–179.
- Etacheri, V., Marom, R., Elazari, R., Salitra, G., and Aurbach, D. (2011). "Challenges in the development of advanced Li-ion batteries: a review." *Energy Environ. Sci.*, 4(9), 3243–3262.
- Fenton, J. H. (1894). "Oxidation of tartaric acid in presence of iron." *J. Chem. Soc. Trans.*, 65, 899–910.
- Fernández de Dios, M. Á., Rosales, E., Fernández-Fernández, M., Pazos, M., and Sanromán, M. Á. (2015). "Degradation of organic pollutants by heterogeneous

electro-Fenton process using Mn–alginate composite.” *J. Chem. Technol. Biotechnol.*, 90(8), 1439–1447.

Fu, C., Zhao, G., Zhang, H., and Li, S. (2013). “Evaluation and characterization of reduced graphene oxide nanosheets as anode materials for lithium-ion batteries.” *Int J Electrochem Sci*, 8, 6269–6280.

Galwey, A. K., and Brown, M. E. (1999). *Thermal decomposition of ionic solids: chemical properties and reactivities of ionic crystalline phases*. Elsevier.

Garg, A., Sangal, V. K., and Bajpai, P. K. (2016). “Decolorization and degradation of Reactive Black 5 dye by photocatalysis: modeling, optimization and kinetic study.” *Desalination Water Treat.*, 57(38), 18003–18015.

Ge, J., Yao, H.-B., Hu, W., Yu, X.-F., Yan, Y.-X., Mao, L.-B., Li, H.-H., Li, S.-S., and Yu, S.-H. (2013). “Facile dip coating processed graphene/MnO₂ nanostructured sponges as high performance supercapacitor electrodes.” *Nano Energy*, 2(4), 505–513.

George, G., and Anandhan, S. (2015). “Photocatalytic Activity of Sol-Gel Electrospun Co₃O₄ Nanofibers in Degrading Methylene Blue and Methyl Orange.” *Ann Mater. Sci Eng*, 2(2), 1025.

Goharshadi, E. K., Hadadian, M., Karimi, M., and Azizi-Toupkanloo, H. (2013). “Photocatalytic degradation of reactive black 5 azo dye by zinc sulfide quantum dots prepared by a sonochemical method.” *Mater. Sci. Semicond. Process.*, 16(4), 1109–1116.

Gonchar, K. A., Zubairova, A. A., Schleusener, A., Osminkina, L. A., and Sivakov, V. (2016). “Optical Properties of Silicon Nanowires Fabricated by Environment-Friendly Chemistry.” *Nanoscale Res. Lett.*, 11(1), 357.

Gorin, G. (1994). “Mole and chemical amount: A discussion of the fundamental measurements of chemistry.” *J Chem Educ*, 71(2), 114.

Grote, F., Kühnel, R.-S., Balducci, A., and Lei, Y. (2014). “Template assisted fabrication of free-standing MnO₂ nanotube and nanowire arrays and their application in supercapacitors.” *Appl. Phys. Lett.*, 104(5), 053904.

Guha, S., Steiner, P., Kozlowski, F., and Lang, W. (1997). “Optical characterization of free-standing porous silicon films.” *J. Porous Mater.*, 4(4), 227–237.

Haber, F., and Weiss, J. (1934). “The catalytic decomposition of hydrogen peroxide by iron salts.” *Proc. R. Soc. Lond. Math. Phys. Eng. Sci.*, The Royal Society, 332–351.

- Hao, J., Zhong, Y., Liao, Y., Shu, D., Kang, Z., Zou, X., He, C., and Guo, S. (2015). "Face-to-face self-assembly graphene/MnO₂ nanocomposites for supercapacitor applications using electrochemically exfoliated graphene." *Electrochimica Acta*, 167, 412–420.
- Henry, J., Mohanraj, K., Kannan, S., Barathan, S., and Sivakumar, G. (2013). "Effect of Butanol and Propylene Glycol in Amorphous MnO₂ Nanoparticles." *Walailak J. Sci. Technol. WJST*, 11(5), 437–443.
- Herino, R., Bomchil, G., Barla, K., Bertrand, C., and Ginoux, J. L. (1987). "Porosity and pore size distributions of porous silicon layers." *J. Electrochem. Soc.*, 134(8), 1994–2000.
- Hollister, S. J. (2005). "Porous scaffold design for tissue engineering." *Nat. Mater.*, 4(7), 518–524.
- Holzwarth, U., and Gibson, N. (2011). "The Scherrer equation versus the 'Debye-Scherrer equation'." *Nat. Nanotechnol.*, 6(9), 534–534.
- Hu, L., Chen, W., Xie, X., Liu, N., Yang, Y., Wu, H., Yao, Y., Pasta, M., Alshareef, H. N., and Cui, Y. (2011). "Symmetrical MnO₂-carbon nanotube-textile nanostructures for wearable pseudocapacitors with high mass loading." *Acs Nano*, 5(11), 8904–8913.
- Hu, L.-F., Li, R., He, J., Da, L., Lv, W., and Hu, J. (2015). "Structure and photocatalytic performance of layered HNbWO₆ nanosheet aggregation." *J. Nanophotonics*, 9(1), 093041–093041.
- Iglesias, O., De Dios, M. F., Rosales, E., Pazos, M., and Sanromán, M. A. (2013). "Optimisation of decolourisation and degradation of Reactive Black 5 dye under electro-Fenton process using Fe alginate gel beads." *Environ. Sci. Pollut. Res.*, 20(4), 2172–2183.
- Jalalah, M., Faisal, M., Bouzid, H., Park, J.-G., Al-Sayari, S. A., and Ismail, A. A. (2015). "Comparative study on photocatalytic performances of crystalline α - and β -Bi₂O₃ nanoparticles under visible light." *J. Ind. Eng. Chem.*, 30, 183–189.
- Jamal, R., Osman, Y., Rahman, A., Ali, A., Zhang, Y., and Abdiryim, T. (2014). "Solid-state synthesis and photocatalytic activity of polyterthiophene derivatives/TiO₂ nanocomposites." *Materials*, 7(5), 3786–3801.
- Jayachandran, M., Paramasivam, M., Murali, K. R., Trivedi, D. C., and Raghavan, M. (2001). "Synthesis of porous silicon nanostructures for photoluminescent devices." *Mater. Phys. Mech.*, 4, 143–147.

Jensen, J. N. (1996). "Applications of ultrasound for the destruction of hazardous waste." *Hazard. Ind. WASTES*, 28, 265–274.

Jiang, R., Huang, T., Liu, J., Zhuang, J., and Yu, A. (2009). "A novel method to prepare nanostructured manganese dioxide and its electrochemical properties as a supercapacitor electrode." *Electrochimica Acta*, 54(11), 3047–3052.

Kakaei, K., and Hasanpour, K. (2014). "Synthesis of graphene oxide nanosheets by electrochemical exfoliation of graphite in cetyltrimethylammonium bromide and its application for oxygen reduction." *J. Mater. Chem. A*, 2(37), 15428–15436.

Kanagaraj, T., and Thiripuranthagan, S. (2017). "Photocatalytic activities of novel SrTiO₃-BiOBr heterojunction catalysts towards the degradation of reactive dyes." *Appl. Catal. B Environ.*, 207, 218–232.

Karatas, M., Argun, Y. A., and Argun, M. E. (2012). "Decolorization of anthraquinonic dye, Reactive Blue 114 from synthetic wastewater by Fenton process: kinetics and thermodynamics." *J. Ind. Eng. Chem.*, 18(3), 1058–1062.

Kaur, N., Shahi, S. K., and Singh, V. (2015). "Anomalous behavior of visible light active TiO₂ for the photocatalytic degradation of different Reactive dyes." *Photochem. Photobiol. Sci.*, 14(11), 2024–2034.

Khaksar, M., Amini, M., Boghaei, D. M., Chae, K. H., and Gautam, S. (2015). "Mn-doped ZrO₂ nanoparticles as an efficient catalyst for green oxidative degradation of methylene blue." *Catal. Commun.*, 72, 1–5.

Khomenko, V., Frackowiak, E., and Beguin, F. (2005). "Determination of the specific capacitance of conducting polymer/nanotubes composite electrodes using different cell configurations." *Electrochimica Acta*, 50(12), 2499–2506.

Kim, D.-A., Shim, J.-H., and Cho, N.-H. (2004). "PL and EL features of p-type porous silicon prepared by electrochemical anodic etching." *Appl. Surf. Sci.*, 234(1), 256–261.

Kim, I.-T., Kouda, N., Yoshimoto, N., and Morita, M. (2015). "Preparation and electrochemical analysis of electrodeposited MnO₂/C composite for advanced capacitor electrode." *J. Power Sources*, 298, 123–129.

Kim, J. S., Choi, W., Cho, K. Y., Byun, D., Lim, J., and Lee, J. K. (2013). "Effect of polyimide binder on electrochemical characteristics of surface-modified silicon anode for lithium ion batteries." *J. Power Sources*, 244, 521–526.

Kodom, T., Dougna, A., Tchakala, I., Gnazou, M.-E. D., Djaneye-Boundjou, G., and Bawa, M. L. (2013). "TiO₂ PC500 coated on non woven paper with SiO₂ as a binder-

assisted photocatalytic degradation of Reactive Black 5 in aqueous solution.” *J. Water Resour. Prot.*, 5(12), 1227.

Kohandehghan, A., Cui, K., Kupsta, M., Memarzadeh, E., Kalisvaart, P., and Mitlin, D. (2014). “Nanometer-scale Sn coatings improve the performance of silicon nanowire LIB anodes.” *J. Mater. Chem. A*, 2(29), 11261–11279.

Kucza, W. (2002). “Structural stability of MnO₂ polymorphs and their reactivity vs. lithium.” *Electrochem. Commun.*, 4(9), 669–673.

Kyzas, G. Z., Deliyanni, E. A., and Matis, K. A. (2014). “Graphene oxide and its application as an adsorbent for wastewater treatment.” *J. Chem. Technol. Biotechnol.*, 89(2), 196–205.

Laohaprapanon, S., Matahum, J., Tayo, L., and You, S.-J. (2015). “Photodegradation of reactive black 5 in a ZnO/UV slurry membrane reactor.” *J. Taiwan Inst. Chem. Eng.*, 49, 136–141.

Lehmann, V., and Gösele, U. (1991). “Porous silicon formation: A quantum wire effect.” *Appl. Phys. Lett.*, 58(8), 856–858.

Li, Y., Wang, J., Zhang, Y., Banis, M. N., Liu, J., Geng, D., Li, R., and Sun, X. (2012). “Facile controlled synthesis and growth mechanisms of flower-like and tubular MnO₂ nanostructures by microwave-assisted hydrothermal method.” *J. Colloid Interface Sci.*, 369(1), 123–128.

Liu, Y., Jin, W., Zhao, Y., Zhang, G., and Zhang, W. (2017). “Enhanced catalytic degradation of methylene blue by α -Fe₂O₃/graphene oxide via heterogeneous photo-Fenton reactions.” *Appl. Catal. B Environ.*, 206, 642–652.

Lucas, M. S., and Peres, J. A. (2006). “Decolorization of the azo dye Reactive Black 5 by Fenton and photo-Fenton oxidation.” *Dyes Pigments*, 71(3), 236–244.

Ma, W., Chen, S., Yang, S., Chen, W., Cheng, Y., Guo, Y., Peng, S., Ramakrishna, S., and Zhu, M. (2016a). “Hierarchical MnO₂ nanowire/graphene hybrid fibers with excellent electrochemical performance for flexible solid-state supercapacitors.” *J. Power Sources*, 306, 481–488.

Ma, Z., Shao, G., Fan, Y., Wang, G., Song, J., and Shen, D. (2016b). “Construction of Hierarchical α -MnO₂ Nanowires@ Ultrathin δ -MnO₂ Nanosheets Core–Shell Nanostructure with Excellent Cycling Stability for High-Power Asymmetric Supercapacitor Electrodes.” *ACS Appl. Mater. Interfaces*, 8(14), 9050–9058.

Macdonald, J. R. (1987). *Impedance spectroscopy*. Wiley New York etc.

- Maddinedi, S. B., and Mandal, B. K. (2014). "Peroxidase Like Activity of Quinic Acid Stabilized Copper Oxide Nanosheets." *Austin J Anal Pharm Chem*, 1(2), 4.
- Mahmoudian, M. R., Alias, Y., Basirun, W. J., Woi, P. M., and Sookhakian, M. (2014). "Facile preparation of MnO₂ nanotubes/reduced graphene oxide nanocomposite for electrochemical sensing of hydrogen peroxide." *Sens. Actuators B Chem.*, 201, 526–534.
- Maruska, H. P., and Ghosh, A. K. (1978). "Photocatalytic decomposition of water at semiconductor electrodes." *Sol. Energy*, 20(6), 443–458.
- McKay, G. (1995). *Use of Adsorbents for the Removal of Pollutants from Wastewater*. CRC press.
- Mehta, P., Mehta, R., Surana, M., and Kabra, B. V. (2011). "Influence of operational parameters on degradation of commercial textile azo dye acid blue 113 (cyanine 5r) by advanced oxidation technology." *J Curr Chem Pharm Sci*, 1, 28–36.
- Mei, J., and Zhang, L. (2015). "Anchoring High-dispersed MnO₂ Nanowires on Nitrogen Doped Graphene as Electrode Materials for Supercapacitors." *Electrochimica Acta*, 173, 338–344.
- Meriç, S., Kaptan, D., and Ölmez, T. (2004). "Color and COD removal from wastewater containing Reactive Black 5 using Fenton's oxidation process." *Chemosphere*, 54(3), 435–441.
- Merlain, T. G., Nanganoa, L. T., Desire, B. B. P., Nsami, N. J., and Mbadcam, K. J. (2016). "Fenton-Like Oxidation of Acid Yellow 23 in the Presence of Iron Rich Soil." *Adv. Chem. Eng. Sci.*, 6(05), 553.
- Meyer, W. H. (1998). "Polymer electrolytes for lithium-ion batteries." *Adv. Mater.*, 10(6), 439–448.
- Milani, S. D., Dariani, R. S., Mortezaali, A., Daadmehr, V., and Robbie, K. (2006). "The correlation of morphology and surface resistance in porous silicon." *J. Optoelectron. Adv. Mater.*, 8(3), 1216.
- Moulijn, J. A., Leeuwen, P. W. van, and Santen, R. A. van. (1993). *Catalysis: an integrated approach to homogeneous, heterogeneous and industrial catalysis*. Elsevier.
- Mu, B., Zhang, W., Xu, W., and Wang, A. (2015). "Hollowed-out tubular carbon@MnO₂ hybrid composites with controlled morphology derived from kapok fibers for supercapacitor electrode materials." *Electrochimica Acta*, 178, 709–720.

- Mukhlis, M. B., Najnin, F., Rahman, M. M., and Uddin, M. J. (2013). "Photocatalytic degradation of different dyes using TiO₂ with high surface area: a kinetic study." *J. Sci. Res.*, 5(2), 301–314.
- Murphy, A. B. (2007). "Band-gap determination from diffuse reflectance measurements of semiconductor films, and application to photoelectrochemical water-splitting." *Sol. Energy Mater. Sol. Cells*, 91(14), 1326–1337.
- Naldoni, A., Allieta, M., Santangelo, S., Marelli, M., Fabbri, F., Cappelli, S., Bianchi, C. L., Psaro, R., and Dal Santo, V. (2012). "Effect of nature and location of defects on bandgap narrowing in black TiO₂ nanoparticles." *J. Am. Chem. Soc.*, 134(18), 7600–7603.
- Nayef, U. M. (2013). "Fabrication and Characteristics of Porous Silicon for Photoconversion." *Int. J. Basic Appl. Sci. IJBAS-IJENS*, 13(02).
- Novoselov, K. S., Geim, A. K., Morozov, Sv., Jiang, D., Katsnelson, Mi., Grigorieva, Iv., Dubonos, Sv., Firsov, and AA. (2005). "Two-dimensional gas of massless Dirac fermions in graphene." *nature*, 438(7065), 197–200.
- Okabe, H. (1978). *Photochemistry of small molecules*. Wiley New York.
- Ossadnik, C., Vepřek, S., and Gregora, I. (1999). "Applicability of Raman scattering for the characterization of nanocrystalline silicon." *Thin Solid Films*, 337(1), 148–151.
- Prakasam, M., Viraphong, O., Cambon, O., and Largeteau, A. (2015). "Hydrothermal Crystal Growth and Applications." *Adv. Solid Oxide Fuel Cells Electron. Ceram. Collect. Pap. Present. 39th Int. Conf. Adv. Ceram. Compos.*, John Wiley & Sons, Inc., 151–156.
- Puentes-Cárdenas, J., Florido-Cuellar, A., Cardona-Bedoya, J., Bohorquez-Echeverry, P., Campos-Pinilla, C., Gutiérrez-Romero, V., and Pedroza-Rodríguez, A. (2012). "Simultaneous decolorization and detoxification of black reactive 5 using TiO₂ deposited over borosilicate glass." *Univ. Sci.*, 17(1), 53–63.
- Qu, J., Shi, L., He, C., Gao, F., Li, B., Zhou, Q., Hu, H., Shao, G., Wang, X., and Qiu, J. (2014). "Highly efficient synthesis of graphene/MnO₂ hybrids and their application for ultrafast oxidative decomposition of methylene blue." *Carbon*, 66, 485–492.
- Rahmani, A. R., Zarrabi, M., Samarghandi, M. R., Afkhami, A., and Ghaffari, H. R. (2010). "Degradation of Azo Dye Reactive Black 5 and acid orange 7 by Fenton-like mechanism." *Iran. J. Chem. Eng.*, 7(1), 87–94.

- Rai, H. S., Bhattacharyya, M. S., Singh, J., Bansal, T. K., Vats, P., and Banerjee, U. C. (2005). "Removal of dyes from the effluent of textile and dyestuff manufacturing industry: a review of emerging techniques with reference to biological treatment." *Crit. Rev. Environ. Sci. Technol.*, 35(3), 219–238.
- Rajeshwar, K. (1995). "Photoelectrochemistry and the environment." *J. Appl. Electrochem.*, 25(12), 1067–1082.
- Ramesh, M., Nagaraja, H. S., Rao, M. P., Anandan, S., and Huang, N. M. (2016). "Fabrication, characterization and catalytic activity of α -MnO₂ nanowires for dye degradation of reactive black 5." *Mater. Lett.*, 172, 85–89.
- Rao, M. P., Anandan, S., Suresh, S., Asiri, A. M., and Wu, J. J. (2015). "Surfactant assisted synthesis of copper oxide nanoparticles for photocatalytic degradation of methylene blue in the presence of visible light." *Energy Environ. Focus*, 4(3), 250–255.
- Rao, M. P., Wu, J. J., Asiri, A. M., and Anandan, S. (2017). "Photocatalytic degradation of tartrazine dye using CuO straw-sheaf-like nanostructures." *Water Sci. Technol.*, 75(6), 1421–1430.
- Reynolds, L. B. (1933). "History of Chemical Precipitation." *Sew. Works J.*, 595–599.
- Sahoo, C., Gupta, A. K., and Sasidharan Pillai, I. M. (2012). "Photocatalytic degradation of methylene blue dye from aqueous solution using silver ion-doped TiO₂ and its application to the degradation of real textile wastewater." *J. Environ. Sci. Health Part A*, 47(10), 1428–1438.
- Said, Z., Saidur, R., and Rahim, N. A. (2014). "Optical properties of metal oxides based nanofluids." *Int. Commun. Heat Mass Transf.*, 59, 46–54.
- Sakai, N., Ebina, Y., Takada, K., and Sasaki, T. (2005). "Photocurrent generation from semiconducting manganese oxide nanosheets in response to visible light." *J. Phys. Chem. B*, 109(19), 9651–9655.
- Saleh, A. F. (2013). "Structural and morphological studies of NiO thin films prepared by Rapid thermal oxidation method." *Int. J. Appl. Innov. Engin-Eering Manag. IJAIEM*, 2(1), 16.
- Samejima, T., Soh, Y., and Yano, T. (1977). "Specific surface area and specific pore volume distribution of tobacco." *Agric. Biol. Chem.*, 41(6), 983–988.
- Saputra, E., Muhammad, S., Sun, H., Ang, H. M., Tadé, M. O., and Wang, S. (2013). "Different crystallographic one-dimensional MnO₂ nanomaterials and their superior

performance in catalytic phenol degradation.” *Environ. Sci. Technol.*, 47(11), 5882–5887.

Saratale, R. G., Saratale, G. D., Chang, J. S., and Govindwar, S. P. (2010). “Decolorization and biodegradation of reactive dyes and dye wastewater by a developed bacterial consortium.” *Biodegradation*, 21(6), 999–1015.

Saravanan, S., and Sivasankar, T. (2016). “Effect of ultrasound power and calcination temperature on the sonochemical synthesis of copper oxide nanoparticles for textile dyes treatment.” *Environ. Prog. Sustain. Energy*, 35(3), 669–679.

Sato, H., Minami, T., Takata, S., and Yamada, T. (1993). “Transparent conducting p-type NiO thin films prepared by magnetron sputtering.” *Thin Solid Films*, 236(1), 27–31.

Shanmugavani, A., and Selvan, R. K. (2014). “Synthesis of ZnFe₂O₄ nanoparticles and their asymmetric configuration with Ni (OH)₂ for a pseudocapacitor.” *RSC Adv.*, 4(51), 27022–27029.

Sharma, S., and Roy, S. (2015). “Biodegradation of dye Reactive Black-5 by a novel bacterial endophyte.” *Int. Res. J. Environ. Sci.*, 4(4), 44–53.

Shaul, G. M., Holdsworth, T. J., Dempsey, C. R., and Dostal, K. A. (1991). “Fate of water soluble azo dyes in the activated sludge process.” *Chemosphere*, 22(1–2), 107–119.

Sheikh, M. U. D., Naikoo, G. A., Thomas, M., Bano, M., Ahirwar, D., Pandit, U. J., and Khan, F. (2016). “Fabrication of hierarchically mesoporous CuO nanostructures and their role as heterogenous catalysts and sensors.” *RSC Adv.*, 6(49), 42807–42818.

Shuttleworth, R. (1950). “The surface tension of solids.” *Proc. Phys. Soc. Sect. A*, 63(5), 444.

Sivakov, V. A., Voigt, F., Berger, A., Bauer, G., and Christiansen, S. H. (2010). “Roughness of silicon nanowire sidewalls and room temperature photoluminescence.” *Phys. Rev. B*, 82(12), 125446.

Soltani, N., Saion, E., Hussein, M. Z., Erfani, M., Abedini, A., Bahmanrokh, G., Navasery, M., and Vaziri, P. (2012). “Visible light-induced degradation of methylene blue in the presence of photocatalytic ZnS and CdS nanoparticles.” *Int. J. Mol. Sci.*, 13(10), 12242–12258.

Song, J. Y., Wang, Y. Y., and Wan, C. C. (1999). “Review of gel-type polymer electrolytes for lithium-ion batteries.” *J. Power Sources*, 77(2), 183–197.

- Stępniewski, W. J., Nowak-Stępniewska, A., Michalska-Domańska, M., Norek, M., Czujko, T., and Bojar, Z. (2014). "Fabrication and geometric characterization of highly-ordered hexagonally arranged arrays of nanoporous anodic alumina." *Pol. J. Chem. Technol.*, 16(1), 63–69.
- Su, X., Wu, Q., Li, J., Xiao, X., Lott, A., Lu, W., Sheldon, B. W., and Wu, J. (2014a). "Silicon-based nanomaterials for lithium-ion batteries: a review." *Adv. Energy Mater.*, 4(1).
- Su, X., Wu, Q., Li, J., Xiao, X., Lott, A., Lu, W., Sheldon, B. W., and Wu, J. (2014b). "Silicon-based nanomaterials for lithium-ion batteries: a review." *Adv. Energy Mater.*, 4(1).
- Sun, J.-H., Sun, S.-P., Wang, G.-L., and Qiao, L.-P. (2007). "Degradation of azo dye Amido black 10B in aqueous solution by Fenton oxidation process." *Dyes Pigments*, 74(3), 647–652.
- Tan, W.-F., Yu, Y.-T., Wang, M.-X., Liu, F., and Koopal, L. K. (2013). "Shape evolution synthesis of monodisperse spherical, ellipsoidal, and elongated hematite (α -Fe₂O₃) nanoparticles using ascorbic acid." *Cryst. Growth Des.*, 14(1), 157–164.
- Tayeb, A. M., and Hussein, D. S. (2015). "Synthesis of TiO₂ nanoparticles and their photocatalytic activity for methylene blue." *Am. J. Nanomater.*, 3(2), 57–63.
- Thakur, M., Isaacson, M., Sinsabaugh, S. L., Wong, M. S., and Biswal, S. L. (2012). "Gold-coated porous silicon films as anodes for lithium ion batteries." *J. Power Sources*, 205, 426–432.
- Theiß, W. (1997). "Optical properties of porous silicon." *Surf. Sci. Rep.*, 29(3–4), 9195–93192.
- Tompsett, D. A., and Islam, M. S. (2013). "Electrochemistry of hollandite α -MnO₂: Li-ion and Na-ion insertion and Li₂O incorporation." *Chem. Mater.*, 25(12), 2515–2526.
- Toufiq, A. M., Wang, F., Li, Q., and Li, Y. (2014). "Hydrothermal synthesis of MnO₂ nanowires: structural characterizations, optical and magnetic properties." *Appl. Phys. A*, 116(3), 1127–1132.
- Vyas, J., Mishra, M., and Gandhi, V. (2013). "Photocatalytic Degradation of Alizarin Cyanine Green G, Reactive Red 195 and Reactive Black 5 Using UV/TiO₂ Process." *Mater. Sci. Forum*, Trans Tech Publ, 284–292.
- Wagner, R. S., and Ooherty, C. J. (1968). "Mechanism of branching and kinking during VLS crystal growth." *J. Electrochem. Soc.*, 115(1), 93–99.

- Wang, K., Gao, S., Du, Z., Yuan, A., Lu, W., and Chen, L. (2016). "MnO₂-Carbon nanotube composite for high-areal-density supercapacitors with high rate performance." *J. Power Sources*, 305, 30–36.
- Wang, W.-Z., Chen, H., Hu, Y.-Z., and Wang, H. (2006). "Effect of surface roughness parameters on mixed lubrication characteristics." *Tribol. Int.*, 39(6), 522–527.
- Wang, X., and Li, Y. (2003). "Synthesis and formation mechanism of manganese dioxide nanowires/nanorods." *Chem.-Eur. J.*, 9(1), 300–306.
- Weng, C.-H., Lin, Y.-T., and Yuan, H.-M. (2013). "Rapid decoloration of Reactive Black 5 by an advanced Fenton process in conjunction with ultrasound." *Sep. Purif. Technol.*, 117, 75–82.
- Williamson, G. K., and Smallman, R. E. (1956). "III. Dislocation densities in some annealed and cold-worked metals from measurements on the X-ray debye-scherrer spectrum." *Philos. Mag.*, 1(1), 34–46.
- Wong, C. P. P., Lai, C. W., Lee, K. M., and Hamid, S. B. A. (2015). "Advanced chemical reduction of reduced graphene oxide and its photocatalytic activity in degrading reactive black 5." *Materials*, 8(10), 7118–7128.
- Wu, Z.-S., Ren, W., Xu, L., Li, F., and Cheng, H.-M. (2011). "Doped graphene sheets as anode materials with superhigh rate and large capacity for lithium ion batteries." *ACS Nano*, 5(7), 5463–5471.
- Xia, S.-J., Liu, F.-X., Ni, Z.-M., Shi, W., Xue, J.-L., and Qian, P.-P. (2014). "Ti-based layered double hydroxides: efficient photocatalysts for azo dyes degradation under visible light." *Appl. Catal. B Environ.*, 144, 570–579.
- Yang, M., and He, J. (2011). "Fine tuning of the morphology of copper oxide nanostructures and their application in ambient degradation of methylene blue." *J. Colloid Interface Sci.*, 355(1), 15–22.
- Yao, Y., McDowell, M. T., Ryu, I., Wu, H., Liu, N., Hu, L., Nix, W. D., and Cui, Y. (2011). "Interconnected silicon hollow nanospheres for lithium-ion battery anodes with long cycle life." *Nano Lett.*, 11(7), 2949–2954.
- Yin, B., Zhang, S., Jiao, Y., Liu, Y., Qu, F., and Wu, X. (2014). "Facile synthesis of ultralong MnO₂ nanowires as high performance supercapacitor electrodes and photocatalysts with enhanced photocatalytic activities." *CrystEngComm*, 16(43), 9999–10005.

Yorikawa, H., and Muramatsu, S. (2000). "Photoluminescence and particle size distribution in porous silicon." *J. Lumin.*, 87, 423–425.

Yu, C., Li, G., Wei, L., Fan, Q., Shu, Q., and Jimmy, C. Y. (2014). "Fabrication, characterization of β -MnO₂ microrod catalysts and their performance in rapid degradation of dyes of high concentration." *Catal. Today*, 224, 154–162.

Zhang, H., Zhang, D., and Zhou, J. (2006). "Removal of COD from landfill leachate by electro-Fenton method." *J. Hazard. Mater.*, 135(1), 106–111.

Zhang, M., An, T., Hu, X., Wang, C., Sheng, G., and Fu, J. (2004). "Preparation and photocatalytic properties of a nanometer ZnO–SnO₂ coupled oxide." *Appl. Catal. Gen.*, 260(2), 215–222.

Zhang, W.-J. (2011). "A review of the electrochemical performance of alloy anodes for lithium-ion batteries." *J. Power Sources*, 196(1), 13–24.

Zhou, H., Yang, X., Lv, J., Dang, Q., Kang, L., Lei, Z., Yang, Z., Hao, Z., and Liu, Z.-H. (2015). "Graphene/MnO₂ hybrid film with high capacitive performance." *Electrochimica Acta*, 154, 300–307.

LIST OF PUBLICATIONS

1. Martha R., Rao M. P., Nagaraja H. S., et al. (2016). "Fabrication, characterization and catalytic activity of α -MnO₂ nanowires for dye degradation of reactive black 5." *Materials Letters*, 172, 85–89.
2. Martha R., Nagaraja H. S. (2017). "Effect of current density on morphological, structural and optical properties of porous silicon., *Materials Today Chemistry*, 3,1014.
3. Martha R., Nagaraja H. S. (2017). "Effect of current density and electrochemical cycling on physical properties of silicon nanowires as anode for lithium ion battery." *Materials characterization*, 129, 24-30.
4. Martha R., Rao M. P., Nagaraja H. S., et al. (2017). "rGO/MnO₂ nanowires for ultrasonic combined Fenton assisted efficient degradation of reactive black 5." *Water Sci Technol.* 76.7, 1652-1665.
5. Dhanush S., Martha R., Nagaraja H. S., et al. (2017). "Synthesized Reduced Graphene Oxide And Sn Doped Manganese Dioxide Nanocomposites For Supercapacitors And Dopamine Sensors." *Materials Today Energy*, 6, 66-74.
6. Martha R., Rao M. P., Nagaraja H. S., et al. (2017). "Photo-catalytic degradation of wastewater containing Azo dyes by synthesized CuO nanoparticles." *J Wat.sci. and Eng.* ×, *in press*.
7. Martha R., Rao M. P., Anandan S., Nagaraja H.S. (2018) "Adsorption, photocatalytic properties of NiO NPs synthesized via a thermal decomposition process." *J. Mater. Res.*, 33(5), 601-610.

Conferences

1. 2nd International Conference on Nanotechnology (ICNT)", February 19-22, 2015.Haldia, West Bengal.
2. National Conference on "Advanced Materials for Energy and Environmental applications" – (AMEEA), March 18-20th, 2015. Bharathiar University , Coimbatore.
3. International Conference on Recent Advances in Nano science and Technology (RAINSAT), July 8- 10th, 2015, SATHYABAMA UNIVERSITY, Chennai.

Conference proceedings

1. Martha R., NagarajaH.S. (2016). "Effect of etching time on structural properties of porous silicon at room temperature."*Materials Today: Proceedings*, 3, 2085–2090.